SCIENCE CHINA
Physics, Mechanics & Astronomy

• Invited Review •

? 2023 Vol. ? No. ?: 000000
https://doi.org/??

Sciences for The 2.5-meter Wide Field Survey Telescope (WFST)

Tinggui Wang[1,2*], Guilin Liu[1,4], Zhenyi Cai[1,4], Jinjun Geng[3], Min Fang[3], Haoning He[3], Ji-an Jiang[1,6], Ning Jiang[1,4], Xu Kong[1,2*], Bin Li[3], Ye Li[3], Wentao Luo[1,2], Zhizheng Pan[3], Xuefeng Wu[3], Ji Yang[3], Jiming Yu[1,4], Xianzhong Zheng[3*], Qingfeng Zhu[1,2], Yi-Fu Cai[1,4], YuanYuan Chen[3], Zhiwei Chen[3], Zigao Dai[1,2], Lulu Fan[1,2], Yizhong Fan[3], Wenjuan Fang[1,4], Zhicheng He[1,4], Lei Hu[3], Maokai Hu[3], Zhiping Jin[3], Zhibo Jiang[3], Guoliang Li[3], Fan Li[3], Xuzhi Li[1,4], Runduo Liang[1,4], Zheyu Lin[1,4], Qingzhong Liu[3], Wenhao Liu[3], Zhengyan Liu[1,4], Wei Liu[3], Yao Liu[3], Zheng Lou[3], Han Qu[3], Zhenfeng Sheng[2], Jianchun Shi[3], Yiping Shu[3], Zhenbo Su[1,4], Tianrui Sun[3], Hongchi Wang[3], Huiyuan Wang[1,4], Jian Wang[2,5], Junxian Wang[1,4], Daming Wei[3], Junjie Wei[3], Yongquan Xue[1,4], Jingzhi Yan[3], Chao Yang[3], Ye Yuan[3], Yefei Yuan[1,4], Hongxin Zhang[1,4], Miaomiao Zhang[3], Haibin Zhao[3], and Wen Zhao[1,4]

[1]*Department of Astronomy, University of Science and Technology of China, Hefei 230026, China;*
[2]*Deep Space Exploration Laboratory /Department of Astronomy , University of Science and Technology of China, Hefei 230026, People's Republic of China;*
[3]*Purple Mountain Observatory, Chinese Academy of Sciences, Nanjing 210023, China;*
[4]*CAS Key Laboratory for Research in Galaxies and Cosmology, Department of Astronomy, University of Science and Technology of China, Hefei 230026, China;*
[5]*State Key Laboratory of Particle Detection and Electronics, University of Science and Technology of China, Hefei 230026, China;*
[6]*National Astronomical Observatory of Japan, National Institutes of Natural Sciences, 2-21-1 Osawa, Mitaka, Tokyo 181-8588, Japan*
Received ?? ??, 2023; accepted ?? ??, 2023

The Wide Field Survey Telescope (WFST) is a dedicated photometric survey facility under construction jointly by the University of Science and Technology of China (USTC) and Purple Mountain observatory (PMO). It is equipped with a primary mirror of 2.5m in diameter, an active optical system, and a mosaic CCD camera with 0.73 Gigapixels on the main focus plane to achieve high-quality imaging over a field of view of 6.5 square degrees. The installation of WFST near the summit of the Saishiteng Mountain in the Lenghu area is planned to happen in the summer of 2023, and the operation is scheduled to commence three months afterward. WFST will scan the northern sky in four optical bands (u, g, r and i) at cadences from hourly/daily to semi-weekly in the deep high-cadence survey (DHS) and the wide field survey (WFS) programs, respectively. WFS reaches a depth of 22.27, 23.32, 22.84, and 22.31 in AB magnitudes in a nominal 30-second exposure in the four bands during a photometric night, respectively, enabling us to search tremendous amount of transients in the low-z universe and systematically investigate the variability of Galactic and extragalactic objects. Intranight 90s exposures as deep as 23 and 24 mag in u and g bands via DHS provide a unique opportunity to facilitate explorations of energetic transients in demand for high sensitivity, including the electromagnetic counterparts of gravitational-wave events detected by the second/third-generation GW detectors, supernovae within a few hours of their explosions, tidal disruption events and luminous fast optical transients even beyond redshift of 1. Meanwhile, the final 6-year co-added images, anticipated to reach $g \simeq 25.5$ mag in WFS or even deeper by 1.5 mags in DHS, will be of significant value to general Galactic and extragalactic sciences. The highly uniform legacy surveys of WFST will also serve as an indispensable complement to those of the Vera C. Rubin Observatory's Legacy Survey of Space and Time (LSST) that monitors the southern sky.

optical telescope, time domain astronomy, photometric survey, supenovae, multi-messenger events, tidal disruption event
PACS number(s):

Citation: WFST collaboration, et al,
, Sci. China-Phys. Mech. Astron. **?**, 000000 (2023), https://doi.org/??

Contents

1 Introduction

Since late 1950s, large surveys have been playing major roles in the development of virtually every domain of astronomy. The first large sky surveys in optical bands were conducted in 1950s through 1980s using the 1.2m Schmidt telescope of Palomar observatory in the northern hemisphere (Palomar Observatory Sky Surveys (POSS) I and II[1]) and the UK Schmidt telescope at AAO and the ESO Schmidt telescope in Chile in the southern hemisphere. The Two-Micron All Sky Survey (2MASS), completed in 2001, employed three near-infrared bands and a pair of matched 1.3m-diameter telescopes in both hemispheres (Arizona and Chile)[2]. These large sky surveys have served as pools of significant discoveries in frontiers from the solar system to galaxies and quasars for dozens of years.

The Sloan Digital Sky Survey (SDSS)[3] is among the most ambitious and influential sky surveys in the history. The dedicated 2.5m aperture telescope employed by SDSS has mapped a quarter of the entire sky and has obtained spectra for millions of galaxies, quasars and stars. In four phases of survey campaigns, SDSS has greatly advanced our understanding of the physics of galaxies, accreting supermassive black holes (quasars), the structure of the universe and our own Galaxy. In addition to their initially designed science goals, the uniform and well-calibrated photometric and spectroscopic legacy data have engaged astronomers from virtually the entire astronomical community, leading to hundreds to thousands of scientific publications each year. Following the success of SDSS, imaging surveys in the southern sky was performed by the Dark Energy Survey (DES) Camera mounted on the 4-meter BLANCO telescope in Chile[4]. Compared to SDSS, DES detects 1.5 mag deeper over a sky area of 5000 square degrees, and 2.5 mag deeper over an area of 1000 square degrees with the ESO 4m survey telescope. The Large Sky Area Multi-Object Fiber Spectroscopic Telescope (LAMOST) has carried out the largest spectroscopic survey of stars in the Milky Galaxy[5]. A high-sensitivity spectroscopic survey of the galaxies and quasars in the northern sky is now ongoing, where the dark energy spectroscopic instrument (DESI) equipped on the Mayall 4m telescope is at work[6].

Time domain surveys explore temporal changes of celestial objects, either intrinsically or extrinsically, by observing the sky repeatedly. These variations often contain crucial information for deciphering the structure and the nature of these variable sources. The blooming of time domain astronomy witnessed in the past decade has been driven the technology development of wide-field survey facilities and the novel discoveries delivered by these facilities. The Catalina Real-Time Survey (CRTS)[7] searched for rare bright transients over a sky area of 33000 square degrees using 3 wide-field telescopes. The Palomar Transient Factory (PTF/iPTF)[8] and its successor, the Zwicky Transient Facility (ZTF)[9],

have monitored 3π of the sky with a cadence of 3 days to a week, with complementary spectroscopy performed by follow-up telescopes. The Panoramic Survey Telescope and Rapid Response System (Pan-STARRS or PS)[10], the All-Sky Automated Survey for SuperNovae (ASAS-SN)[11], and the Asteroid Terrestrial-impact Last Alert System (ATLAS)[12] also conduct time-domain surveys and record transient sources. In general, time-domain surveys employ dedicated telescopes with apertures from a few tens of cm up to 1.3m and large pixel sizes, with the exception of Pan-STARRS, which used two 1.8m Telescopes and Giga-pixel cameras. Currently, Pan-STARRS is largely dedicated to the search of near-earth asteroids (NEA). The limiting magnitudes in a single exposure for these surveys are in the range of 17.0 mag in V band for ASAS-SN to 21.8 mag in r-band for Pan-STARRS.

At present, the demand for time domain surveys reaching fainter magnitude limits is growing due to the discovery of kilonovae, the electromagnetic emitter associated with the merger of neutron stars, and the increasing interest in high-redshift supernovae along with other transients with applications in cosmology and multi-messenger astronomy [13, 14]. The electromagnetic counterparts of gravitational wave sources detectable by the advanced LIGO/Virgo network in the upcoming five years will be typically 1-2 magnitudes fainter than the sensitivity limit of current major time domain surveys. These transient sources, moreover, are located in bright galaxies, and therefore easily overwhelmed by starlight in the low spatial resolution images attained in current surveys. As for the southern sky, the Vera C. Rubin Observatory (VRO) with a flagship wide-field survey telescope of 8.4 meter aperture will be commission in the upcoming year, on which a 30 second exposure is expected to reach a single-epoch magnitude limit of 24.5 mag in r band [15]. However, no time domain facilities have been planned to situate on the northern hemisphere or at a sufficiently low latitude that is anticipated to reach a similar depth.

The Wide Field Survey Telescope (WFST) is designed for scanning the dynamic 2π northern sky with four filters ($ugri$) every year and covering over 1000 deg^2 in each single night. The additional sensitive w-band allows for detecting asteroids in the solar system. It has an aperture of 2.5m in diameter, a field of view of about 3 deg in diameter, and is equipped with a mosaic of nine 9K×9K CCDs set on the primary focus. The telescope is currently being developed jointly by University of Science and Technology of China and Purple Mountain Observatory, CAS, and is expected to be installed on the mountain of Saishiteng near Lenghu in the early of 2023. The remarkable throughput of the optical system and site conditions render a depth 2 mag deeper than ZTF in a single 30s exposure, along with superior image quality. The high altitude and low water vapor result in a relatively high u-band efficiency, a standing-out advantage among time domain survey facilities aiming at the northern sky. As for site location, WFST and VRO are complementary both in longitude (158 degrees apart) and in latitude (on northern/southern hemisphere).

In this paper, we describe the expected performance of WFST and its observation strategy in Section 2. The relevant time domain sciences including supernovae, tidal disruption events (TDE), multi-messenger astrophysics and active galactic nuclei (AGN) are covered in Sections 3.1 through 3.4, while the Milky Way together with its neighbors and the solar system are discussed in Sections 4 and 5, respectively. Prospects in galaxy formation and cosmology are discussed in Section 6 and a summary of this paper is given in Section 7.

2 Expected Performance and Survey Strategy

2.1 Expected Performance of the System

The Wide Field Survey Telescope (WFST) is a 2.5m optical telescope with primary-focus optics designed for a wide 3° field of view (FoV). The optical system consists of a primary mirror, five corrector lenses, an atmospheric dispersion compensator (ADC), and the filters of six optical bands (u,g,r,i,z and w). Active optics (AO) is equipped to keep the telescope in a seeing-limited condition and to reduce primary-focus assembly (PFA) misalignment and primary mirror deformation. The scientific imaging array consisting of nine 9K×9K CCDs (E2V CCD290-99) with a pixel size of 10μm will be installed in the primary focus plane, resulting in an effective FoV of about 6 square degrees.

The telescope will be located on the top of the Saishiteng mountain near Lenghu (93°53′ E, 38°36′ N) at an altitude of 4200 m. The observing conditions of the site have been monitored for three years ever since 2018 [16], which gives a median value of seeing of 0.75 arcsec, an average night sky background brightness around 22.0 mag arcsec^{-2} at V-band when the moon is below the horizon. The nightly observable time ranges from 5 hours in June to over 11 hours in January in each year. The clear time fraction is about 70%, and the observing conditions in a significant number (337) of nights reach photometric requirements in the year 2021[1)]. Taking into account of a number of downgrading factors beyond the designed imaging performance of the optical system, doom and atmospheric seeing, we expect that the over-

1) http://lenghu.china-vo.org/sitecondition

all image quality is approximately 1″, if a median seeing of 0.75″ is assumed. The averaged throughput is estimated to be 0.39, 0.72, 0.60, 0.56 and 0.33 for *u*, *g*, *r*, *i* and *z* bands, respectively.

We estimate the limiting magnitudes of WFST based on the specification of the system design along with relevant available data. We take a value of 22.0 mag arcsec^{-2} as the V-band sky background level, and adopt a model spectrum obtained from the SkyCalc code (Version 2.0.9) developed by ESO astronomers. An airmass of 1.2 is assumed, and aperture photometry is applied to estimate the limiting magnitudes of the system for point source ($\mathrm{Mag}_{30\mathrm{s}}$) required to render a signal-to-noise ratio (SNR) of 5 for a 30 second exposure. We also compute the limiting magnitudes ($\mathrm{Mag}_{50\mathrm{m}}$) of the images stacked from one hundred 30-seconds exposures with a total integration of 50 minutes. These results are reported in Table 1 [17].

Filter	***u***	***g***	***r***	***i***	***z***	***w***
Mag$_{\mathrm{sky}}$	22.51	22.33	21.39	20.65	19.71	21.42
Mag$_{\mathrm{30s}}$	22.27	23.32	22.84	22.31	21.38	23.47
Mag$_{\mathrm{50m}}$	24.82	25.85	25.36	24.83	23.90	25.99

Table 1 Site Sky Brightness and Limiting Magnitudes for 30s exposures and stacked 50 min exposures assuming airmass=1.2.

2.2 Survey Strategy

In this subsection, we describe the two planned key programs of the WFST 6-year survey: the Wide-field Survey (WFS) program and the Deep High-cadence *u*-band Survey (DHS) program. The different designed survey modes, in terms of survey depth, area and cadence, are commensurate with the primary scientific objectives of WFST. As part of the WFST 6-year survey, each program will occupy about 45% of the total observing time. The remaining ∼ 10% of the observing time (about 1,300 hours over 6 years) will be attributed to smaller campaigns for specific purposes, such as capturing time-critical targets and intensively scanning certain sky areas of particular interests (e.g. the Galactic plane).

The WFS program will cover an area of ∼ 8,000 deg^2 in the northern sky. It will employ four broad bands (u, g, r, i) with a single exposure of 30 seconds, leading to about 90 visits per pointing in each band over 6 years, if a clear night fraction of 70% at Lenghu site is assumed [16]. As for the purpose of long-term monitoring of specific targets (e.g. active galactic nuclei and variables), single-band visits will be evenly distributed in 6 years, i.e. 60 multi-band visits (15 visits × 4 bands) per pointing per year, yielding yearly raw data of about 100 TB from the entire WFS fields. Observations for about 300 different pointings (∼2,000 deg^2) with 60 visits per pointing will be executed throughout WFS during three months, leading to about 1,200 pointings in total every year. All of *u*-band observations are scheduled in dark and grey nights, in view of the highly sky background-sensitive measurements planned in this band. To balance the survey efficiency and science goals, and to optimize the homogeneity of WFS visits, we will avoid consecutive observation in a single band, but will observe in two bands every night, with the sole exception of *u* band. This strategy will result in a reasonable cadence and time span in characterizing multi-band light curves for general purposes of time-domain research (e.g. transient classifications, variability statistics, and time-domain cosmology). Meanwhile, total integration in each band will reach ∼ 45 min over 6 years, achieving deeper detection than any of the existing single-telescope surveys with comparable survey areas on the northern hemisphere.

In addition to WFS, we plan for the Deep High-cadence *u*-band Survey (DHS) program by virtue of the superior *u*-band imaging performance of WFST in time-domain investigations. DHS will routinely monitor a sky area of 2 × ∼ 360 deg^2 surrounding the equator every year (the "Spring" and "Autumn" fields; 6 months observing per each). Considering the importance of *u*-band imaging and color information in revealing the nature of various energetic transient phenomena, for each 6-months campaign of DHS, we perform photometry in at least one more band besides *u* in hour cadence in consecutive ± 7 days during every lunar cycle (starting from the new moon). Meanwhile, a multi-band ancillary survey will keep monitoring the same region in the remaining nights of these 6 months. Such an innovative survey mode provides a unique opportunity to track transients right after their occurrences and to discover rare energetic explosive phenomena in the universe (e.g. early-phase supernovae, fast blue optical/ultraluminous transients, tidal disruption events, kilonovae, etc. Further details are deferred to §3.1–§3.3). WFST will also be combined with the next-generation Chinese space missions (e.g. the Einstein Probe (EP) [18]; the Chinese Space Station Telescope (CSST) [19]) to be launched in the upcoming years, so that unprecedented synchronization of multi-wavelength surveys between ground-based and space-borne wide-field survey facilities becomes feasible. By coordinating with EP and CSST, we will not only promptly identify optical counterparts of various high-energy astronomical events, but also attain real-time spectral energy distributions of various fast transients, by virtue of the anticipated synchronization and synergy.

Wide-field imaging is a mainstream tool employed in numerous fields of cutting-edge astronomy, whose success has been witnessed in plentiful accomplished and ongoing wide-

field survey projects. The prominent survey capability and high u-band sensitivity of WFST brings new opportunities to deep and wide exploration of the transient sky on the northern hemisphere, especially at blue optical wavelengths. The resultant large amount of multi-color light curves with cadences varying from hours to years will allow for systematic investigation of photometric behaviors of transients on different timescales from the local to distant universe. The 6-year u-band data will render final stacked u-band images reaching $\gtrsim$ 26 mag (5σ) over an area of about 1,000 deg^2 DHS fields, a depth comparable to that of the final u-band products from Vera C. Rubin/LSST to be released 10 years later. In addition to hundreds of thousands of multi-band light curves, the outcome of WFS and DHS will include weak-lensing shape catalogs with photometric redshift and shape information of over 200 million galaxies, ~ 40 thousand photometrically selected galaxy clusters, and reference catalogs listing astrometry, proper motion and other information of stars as fainter as 23 mag. WFST will contribute an invaluable legacy beneficial to the entire astronomical community in the era of 20–40m class optical and near-infrared telescopes, wide-field spectroscopic survey facilities (e.g. the Subaru Prime Focus Spectrograph, the MUltiplexed Survey Telescope), and space survey missions (e.g. CSST, Euclid, the Nancy Grace Roman Space Telescope).

3 Time-domain Science

3.1 Supernovae

3.1.1 Supernova Observations, Diversities, and Open Questions

The observation of supernovae (SNe) has a long history. The first reliably recorded SN, "SN 185", dated back to AD 185, was reported in *Book of the Later Han Dynasty* by ancient Chinese astronomers. During the centuries after that, a few SNe were discovered. The earliest systematic search for extragalactic transients was initiated in the late 1930s [20], and over 100 SNe were spotted by the Palomar Supernova Search in the following decades. Systematic SN search in the southern hemisphere started in the 1980s, and the SN detection efficiency was significantly improved in the 1990s, thanks to the advancement of charge-coupled devices (CCDs) incorporated into robotic telescopes and automatic search. More recently, the wide application of large-array CCD cameras in wide-field transient survey projects have found SNe across a wide range of redshift, and the discovery rate of SNe has been increasing exponentially over the last two decades. The wealth of SN data has remarkably deepened our understanding of stellar evolution, the SN explosion mechanism, the chemical enrichment of galaxies, and the fundamental physics of the universe. In the upcoming decade, growth spurts of transient detections in both northern and southern hemispheres are expected, resulting from wide-field surveys conducted by WFST and the Vera C. Rubin Observatory [15].

Type Ia supernovae (SNe Ia) are widely accepted as thermonuclear explosion of a carbon-oxygen white dwarf (WD) in a binary system. As significant as the success of using them as a cosmic distance indicator in the 1990s, their progenitors and the physical mechanism underlying the explosion remain under debate [21, 22]. As SNe Ia also play a key role in the chemical enrichment of galaxies and the universe, further understanding of them promise to enlighten us on the origin of major chemical species. The progenitor scenarios proposed for SNe Ia as yet can be generally categorized as single-degenerate (SD), double-degenerate (DD), and core-degenerate (CD). In the SD scenario, a carbon-oxygen white dwarf (WD) accretes materials from a non-degenerate companion star (e.g. a main-sequence or a red giant star) and its mass reaches the Chandrasekhar's limit. The DD scenario involves merger of binary WDs, while a WD and an asymptotic giant branch (AGB) star are postulated in the CD scenario.

Debates on the prevalent progenitor scenarios of SNe Ia has lasted long. Recently, a growing number of works suggest that SNe Ia are likely a mixture of the end products of different evolutionary paths. The key at present, therefore, is to clarify different progenitor paths, different SN Ia subclasses and their relationship. Typical or "normal" SNe Ia demonstrate a strong correlation between the light curve declining rate and the peak luminosity (the so-called "Phillips relation" [23]) and their peak luminosity show uniformity after correcting for this correlation. However, the tremendous amount of SNe Ia discovered in recent years reveal a considerable number of "abnormal" SNe Ia. The primary SN Ia subclasses are SN 1991T-like SNe Ia (91T-like) at the bright end and SN 1991bg-like SNe Ia (91bg-like) at the faint end. Other subclasses include the carbon-rich over-luminous SNe Ia (or "Super-Chandrasekhar" SNe Ia) that are even more luminous than 91T-like SNe Ia at the peak, leading to an estimated total mass of ^{56}Ni synthesized in these events exceeding ~1 $M_\odot$, and thus a reasonable estimate of the total mass is likely over the Chandrasekhar's limit [24-28]. Another subclass already intensively investigated in the last decade is SN 2002cx-like SNe Ia (or "SNe Iax" [29]). SNe Iax are typically faint, with absolute magnitudes spanning a wide range between ~-14 and -18 mag. A fairly rare SN Ia subclass, so-called "SNe Ia-CSM", is spectroscopically similar to Type IIn SNe (SNe IIn) that show blue continuum and strong emission lines of Balmer series, features of SN ejecta expanding into dense circumstellar materials (CSM). In contrast to SNe

IIn due to explosion of massive stars, SNe Ia-CSM are interpreted as SNe Ia explosion inside dense CSM and are likely relevant to 91T-like SNe Ia.

The core collapse of massive stars ($M > 8\ M_{\odot}$) with retained hydrogen envelopes produces the hydrogen-rich Type II SNe (SNe II), whereas if the hydrogen (sometimes even helium as well) envelopes are stripped off, we observe stripped-envelope core-collapse supernovae (SESNe). SESNe are classified into Type IIb, Ib, and Ic SNe based on the hydrogen and helium lines in the spectra [30]. It is not clear yet whether SESNe arise from single evolved massive stars or interacting binary systems or both, whether a continuum of properties between SESN subclasses exist or not, and whether different subclasses represent distinct explosion mechanisms and/or progenitor systems.

The four main subclasses of SNe II, known as SNe IIP, SNe IIL, SNe IIn and SNe IIb, have been identified. SNe IIP ("P" stands for "plateau") display constant luminosity that lasts for approximately three months, while SNe IIL ("L" stands for "linear") show a linear magnitude decline in their light curves [31]. SNe IIn are featured by their narrow (a few hundred km s^{-1}) hydrogen emission lines atop broad bases in their spectra [32]. The narrow component of these lines is attributed to the slowly moving CSM ejected by the SN progenitor before explosion. SNe IIn show diverse light curve behavior mainly due to the perplexing interactions between SN ejecta and CSM. SNe IIb display prominent broad hydrogen lines early in their evolution, while these lines gradually weaken and the spectra become helium-dominated. At later times SNe IIb appear similar to SNe Ib, suggesting that the progenitors of these "intermediate" events may have experienced a stripping level between those of SNe II and SNe Ib. The observed diversity of SNe II brings up the problems of how different these subclasses are and how to quantify them. Given that the diversity is most likely relevant to the progenitor systems of SNe II, a further question is what the different progenitor systems are that lead to these different explosions. Despite that substantial progress in our understanding of core-collapse supernovae (CCSNe) has been made during the last few decades, we still lack a complete picture of their diversity and how it is mapped to various progenitor channels. Furthermore, it remains enigmatic which CCSNe yield typical pulsars and which yield magnetars, black holes, or gamma-ray bursts.

The operation of the WFST high-cadence deep imaging survey allow us to anticipate detection of tens of thousands of SNe from the 6-year survey project. Over one hundred SNe within a few days after their explosions ("early-phase supernovae") are expected to be discovered every year (§3.1.6). The flood of well-observed SNe data collected by WFST promises to help construct a more solid connection between the evolving stars and the stars dying as SNe.

3.1.2 Early-phase Supernovae

During the past decades, dozens of early-phase SNe Ia discovered by wide-field survey projects provide clues to the progenitor systems and the explosion mechanism of SNe Ia [33-35]. Theoretically, a prominent brightening within the first few days of the SN Ia explosion is observable from particular viewing directions, a result of the interaction between the expanding ejecta and the non-degenerate companion star [36], causing a luminosity enhancement in the early time ("early-excess SNe Ia"; EExSNe Ia) as a powerful indicator for the SD progenitor system. Surveys for EExSNe Ia is now with particular popularity in time-domain astronomy, and several EExSNe Ia have been discovered since 2012.

In theory, besides the companion-ejecta interaction scenario, the interaction between confined dense CSM and the SN ejecta ("CSM-ejecta interaction" [28]) or the dynamic mixture of radioactive ^{56}Ni in the outermost region of SN ejecta ("surface-^{56}Ni-decay" [37-39]) may produce similar early light-curve excess. Moreover, radiation from short-lived radioactive elements generated by a precursory detonation in a helium shell of the primary WD ("He-shell detonation" or "He-det" [35, 40]) can cause a prominent but relatively red early excess. Previous observations are suggestive of multiple origins of EExSNe Ia and current shallow low-cadence wide-field surveys can only provide limited constraints to the origin of the early-excess feature. The deep and wide imaging of WFST will help unravel the progenitor issue of SNe Ia from a unique respect, i.e. by systematically depicting their light curves from an early time indeed (within one day after explosion). A major open question on SNe Ia is which progenitor system plays a leading role in yielding these SNe. From the early-excess perspective, none of the known EExSNe Ia is exclusively explained by the companion-ejecta interaction scenario, implying for a low possibility of dominance of the SD scenario. Given that only a modest fraction of early-phase SNe Ia manifest early-excess emissions in the companion-ejecta interaction scenario as a result of the viewing angle effect, we expect WFST to discover numerous early-phase SNe Ia to facilitate further tests and improvements of the current companion-interaction models. Furthermore, we anticipate robust evidence of the SD progenitor system by finding bona fide companion-ejecta interaction EExSNe Ia in the near future.

The rise time of SNe Ia (i.e. the time interval from its first light to the *B*-band maximum brightness) can be readily estimated for well-observed early-phase SNe Ia. Stretch-corrected mean rise time is found to be 17–18 days in a statistically significant sample of SNe Ia, in line with analyses of

individual normal SNe Ia discovered at very early time. Recently, the Zwicky Transient Factory (ZTF) constructed an even larger sample of early-phase SNe Ia, finding a a mean rise time of 18.5 days with remarkable scatter (no stretch correction applied). In contrast, EExSNe Ia commonly exhibit rise times longer than the mean values found in statistics, suggesting that a certain amount of SNe Ia experienced a long dark phase. With dozens of SNe Ia discovered by WFST within about one day after their explosions in each year, the WFST early-phase SNe Ia will place the tightest ever constraints on their rise-time, which promises to fill in the last piece of the puzzle of the earliest radiation from the SN Ia explosion.

For CCSNe, the earliest electromagnetic emission of SNe, known as the SN shock breakout (SBO), is observable only in the first minutes to hours after the emergence of the shock from the stellar surface. The strength of the CCSN SBO can be used to derive the radius of the exploding star and thus conveys important information about the structure and evolution of the progenitor. Due to the brief duration of SBO, only one event has been captured with certainty by ground-based wide-field imaging so far [41].

Recent observations of early-phase CCSNe also pose challenges to the existing theories of stellar evolution and SN explosion. A portion of early spectra of CCSNe show highly-ionized emission lines (so-called "flash" features), which have been interpreted to originate in the CSM at the very vicinity of the SN progenitor, manifesting the mass loss in the final decades. This is a novel probe to the stellar activity in the final evolutionary phase of massive stars. Indeed, such a mass-loss activity in the final stage is unprecedentedly recognized and its origin is not yet clarified, necessitating a revisit to the current stellar evolution theory. We expect early-phase CCSNe to be discovered by WFST DHS to render insights to the structure of dying massive stars and the potential relationship between the final stellar activity and the progenitor mass. In addition, the survey will allow to detect or set an upper limit of the precursors for the nearby SNe at much deeper level than current time-domain surveys, which can probe the last-minute stellar activity of massive stars.

3.1.3 Fast Transients and Their Relationship with Core-collapse Supernovae

Transients with rapid UV and optical flux variance are of particular interest to the community, as their extreme photometric behaviors not only allow for pursuing the physical properties of their progenitors, but also indicate the existence of theoretically-predicted or unknown objects in the universe. These transients mainly include (1) specific types of CCSNe (e.g. some Type Ib/IIb/Ibn supernovae; [42]) that display light-curve evolution significantly faster than the majority of SNe, (2) a newly confirmed transient type, so-called fast blue optical transients (FBOTs) or fast-evolving luminous transients (FELTs), and (3) optical counterparts of binary neutron star mergers, i.e., kilonovae (§3.3).

Recent works have confirmed the existence of at least two distinct subclasses of FBOTs: one with peak luminosities comparable to typical SNe (hereafter "normal FBOTs", the vast majority of previously found FBOTs) and the other with peak bolometric luminosities $\sim 10^{44}$ erg s^{-1} (hereafter "fast blue ultraluminous transients" or FBUTs, e.g. AT 2018cow, MUSSES2020J [43, 44]). The normal FBOTs likely originate from the CCSN SBO within dense circumstellar materials surrounding the progenitor. If so, the fast-evolving light curves of normal FBOTs imply for a dramatic mass-loss process in the few years before the core collapse of the progenitor. In the next few years, the photometric and spectral information of a considerable number of normal FBOTs discovered by WFST will shed light on the explosion mechanism of normal FBOTs and the mass-loss history of massive stars.

The origin of FBUTs is under active debate, because the extremely high luminosity and fast-evolving light curve cannot be interpreted as an extension of the SNe properties. Several alternative mechanisms have been proposed, including emission from the interaction of the SN shock wave with dense CSM, the injection of energy from spin-down of a young magnetar formed either in a CCSN or in a binary neutron star merger, accretion onto a newly formed compact object in a failed supernova, mergers of binary white dwarfs, and tidal disruption of stars by intermediate-mass or massive black holes ("IMBH TDE"; see §3.2.3 for details). Recent studies find FBUTs to be usually accompanied by prominent emission in X-ray and radio wavelengths, indicating a compact object in the center of FBUTs. In view of the very low event rate in the local universe and the high UV luminosity of FBUTs, WFST DHS is expected to be the most promising survey project to accomplish a systematic investigation of this extreme transient phenomenon in the 2020s.

3.1.4 Extreme Supernovae

The optical luminosity of superluminous supernovae (SLSNe) peak at $\lesssim$ -21 mag [45]. Most SLSNe are 10 to 100 times brighter than typical CCSNe. The low event rate of SLSNe results in their first discovery as recent as in 1999. After that, several SLSNe were occasionally found in the 2000s. In the last decade, over 100 SLSNe were observed by unbiased transient surveys equipped with large-array CCD cameras. In the observational respect, the SLSNe population can be naturally divided into hydrogen-poor (SLSNe-I) and hydrogen-rich events (SLSNe-II). The majority of SLSNe-II

emit narrow lines (SLSN-IIn), a feature similar to that of less luminous SNe IIn [46]. Therefore, they are interpreted as extreme cases of SNe IIn mainly powered by the interaction between ejecta and dense CSM. SLSNe-I are less well-understood, for which the dominate mechanism underlying their explosions is still under debate [47].

A major open question about SLSNe is the energy source that powers these extremely luminous and long-lived events. Is a central engine necessarily required? If so, what kind of engine(s) (e.g., a magnetar, an accreting black hole, or both) are at work? Tackling these questions demands for samples consistently enlarged in high-cadence deep imaging surveys and intensive follow-up observations. The 6-year WFST WFS project will regularly monitor the northern sky at a cadence of a few days, so that SLSNe at $z \lesssim 1$ will be detected with high completeness by virtue of their long-lasting and luminous light curves. SLSNe at high redshift is a potential focus of attention in the 2020s, not only of importance to the time-domain astronomy but also to tracking the star formation history in the high-z universe. Moreover, they may become useful distance estimators for cosmological measurements in the future. Taking the advantage of high UV luminosity of SLSNe and their higher event rate at higher redshift ($z \lesssim 2$), WFST that has the superior u-band sensitivity and the properly designed telescope aperture will be the most powerful telescope of searching SLSNe at $z > 0.5$ in the northern hemisphere.

An extremely luminous type of SNe in theoretical prediction, known as the pair-instability SNe (PISNe), remains elusive. PISNe are inferred to be the explosion of massive stars with zero age main sequence (ZAMS) masses of about 130–260 $M_\odot$. The high temperature in the stellar cores of these massive stars causes the copious production of electron–positron pairs that in turn result in contraction of the core, followed by explosive oxygen burning that unbinds these ultra-massive stars eventually [48]. For stars with slightly lower ZAMS masses of 90–130 $M_\odot$, the progenitor may experience multiple non-destructive pair instability episodes that expel materials prior to the final core collapse. These pulses can lead to shell collisions that power a SN-like transient. The succession of shell ejection may alternatively be followed by a PISN, of which the ejecta collides with the preceding ejected shells. This repetitive shell-collision system, with or without a final PISN, is called a pulsational pair-instability SN (PPISN [49]). PISNe and PPISNe are both extremely luminous SNe, but merely a few candidates have been reported due to the difficulty of yielding their massive progenitors in the low-z universe. Yet, the large FoV and deep imaging capability of WFST will boost the sample of PISN/PPISN candidates in the process of the planned 6-year WFST transient survey.

3.1.5 Cosmology and Gravitational Lensing

Two decades passed since its discovery, the nature of dark energy remains a mystery. The recent measurement of H_0 from the local SN Ia distance ladder, calibrated to Cepheid variables is in tension with the inference from the early universe using the cosmic microwave background (known as the "Hubble tension"). At present, three large projects designed for measuring cosmological parameters with SNe Ia are underway or planned: the Hyper Suprime-Cam Subaru Strategic Program (HSC SSP [50]), the Vera C. Rubin Observatory Legacy Survey of Space and Time (VRO/LSST [15]), and the Nancy Grace Roman Space Telescope. Nevertheless, none of these projects will construct an optimal SNe Ia sample at redshift below 0.3 for measuring cosmological parameters. Roman will find a very limited number of low-z SNe, while the nominal-cadence survey strategies of HSC SSP and VRO/LSST will leave significant multiple/single-filter gaps in their low-z SN light curves, which will downgrade the accuracy of SN Ia standardization. Hence, a large and unbiased WFST SN Ia sample to be observed with relatively high-cadence (i.e. $\lesssim$ 3 days) will further reduce the uncertainty in the measurement of dark energy density in the $0.1 < z < 0.3$ redshift bin, allowing for a precise comparison with the well-constrained measurements in the $z < 0.1$ bin. The WFST SN Ia sample also promise to refine and extend SN Ia standardization models and to improve the constraints on the relationship between SN Ia distance measurements and the properties of their host galaxies.

Among the wide range of cosmological probes in the literature, SNe II are regarded as a promising independent method for deriving accurate distances and measuring cosmological parameters. Despite that SNe II display a large range of peak luminosities, several standardization methods have been developed, such as the expanding photosphere method, the standard candle method (SCM), the photospheric magnitude method, and the photometric color method (PCM). SCM is currently the most accurate and commonly used method to derive SN II distances, allowing to construct a Hubble diagram with a ~10 percent dispersion in distance, suggesting that SNe II are potentially complementary and independent tools to constrain the nature of dark energy. Previous SN II Hubble diagrams based on SCM mainly focus on the low-z universe ($z < 0.2$), where distinguishing different cosmic expansion histories is challenging. Therefore, measurements extending further back in time using SNe II at higher redshift will be instrumental to distinguish cosmological models. Expecting thousands of WFST SNe II at $z > 0.1$ to be found in the upcoming years, we will readily perform direct comparison with SN Ia measurements at $0.1 < z < 0.3$ and reveal the relevant implications.

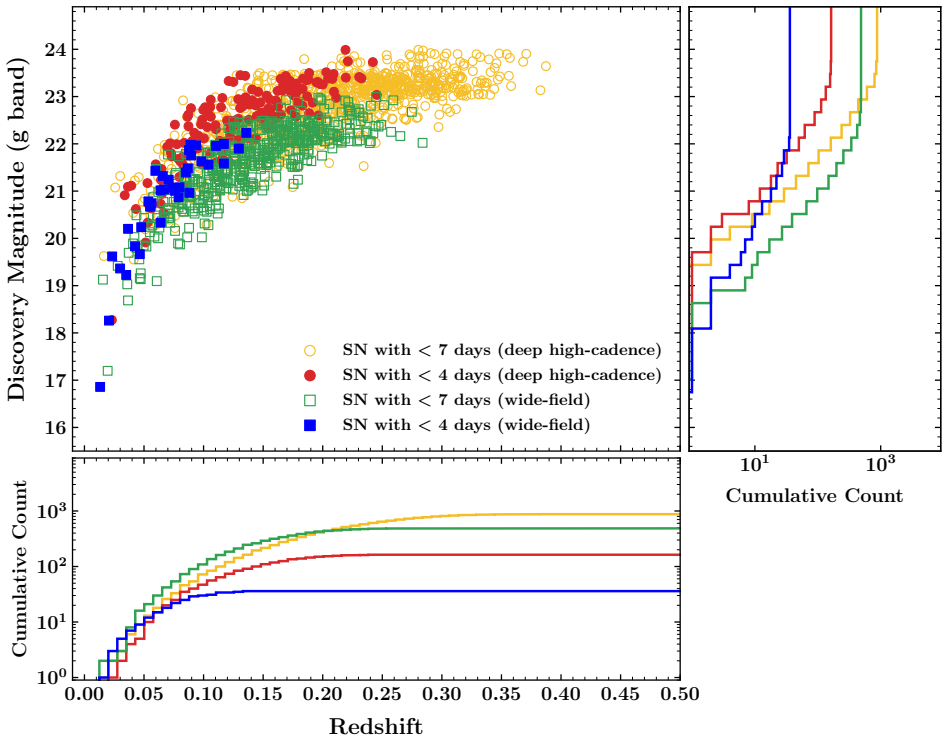

Figure 1 Expected distribution of yearly SNe Ia on the discovery magnitude vs. redshift plane in WFST deep high-cadence (circles; 360 deg^2 daily) and wide-field (squares; 2000 deg^2 in 4 days) surveys. The SNe are divided into two groups as per the time of the second detection t: open and solid symbols denote the SNe discovered with $t < 7$ days and $t < 4$ days, respectively. Right and bottom panels show cumulative counts in terms of discovery magnitude and redshift, respectively.

Recent discoveries of strongly-lensed SNe have opened up a new frontier in the domains of cosmology and early-phase SNe. Strongly-lensed SNe are events where multiple light rays from a SN converge due to the gravity of an intervening object (e.g. a galaxy or a galaxy group or cluster), which results in multiple lensed SN images. A notable feature of such a system is the relative time delays among the lensed SN images due to the difference in light paths. The validation of time delays in strongly-lensed SN systems as an independent probe for the Hubble constant H_0 has been well recognized [51]. Nevertheless, before the discovery of the first multiply-imaged SN in 2015 [52], this "time-delay cosmography" technique had only been applied on strongly-lensed quasars, for which time delays are also measurable (§3.4.5). An up-to-date work achieved a 2.4% precision measurement of H_0 from the combination of six strongly-lensed quasars [53], demonstrating the technique being a competitive and complementary approach. In comparison, time delays measurement is easier for lensed SNe, thanks to their characteristic light curves. Meanwhile, since SNe will eventually disappear, precise lens models are attainable through analyzing these systems without contamination from transients themselves. Eventually, strongly-lensed SNe are expected to provide more stringent constraints on H_0 than quasars [54]. Strong-lensing time delays also offer a unique opportunity to probe SNe shortly after their explosions, in that once a lensed SN is found, follow-up observations could be scheduled well in advance to readily track the entire process of explosion.

To date, only five strongly-lensed SNe have been discovered. A deep wide-field imaging survey with WFST will substantially increase the sample size of strongly-lensed SNe. According to Oguri et al.[55], we expect to find over 20 strongly-lensed SNe in the 6-year WFST WFS program. With dozens of WFST strongly-lensed SNe in the 2020s in hand, we expect to embrace engaging opportunities in the frontiers of cosmology and early-phase SN study.

3.1.6 Supernova Search with WFST

The three key parameters of a transient survey are its depth, area, and cadence. The time-domain-related scientific output from the WFST surveys is optimized by properly coordinating these parameters. The weakness of most previous or ongoing transient surveys lies in the limited survey depth when small-aperture (< 1.5m) telescopes are employed, or the low

survey cadence in the case of large-aperture telescopes, hindering systematic investigations of the photometric behaviors of early-phase SNe and fast transients with faint brightness and fast-evolving light curves in minutes to a few days. Thanks to the specially designed large FoV and aperture of WFST, these objects of interest are expected to be efficiently discovered via WFST high-cadence deep-imaging surveys.

Here we present one-year WFST survey simulations at 3-day and 1-day cadences, corresponding to the wide-field and deep high-cadence surveys, respectively (Figure 1). Since we plan to obtain color information in each observable night, we simply assume in our simulations that the telescope monitors the same sky area in at least two bands (e.g. u and g) every night. The clear night fraction, moon phase influence, and target visibility have all been taken into account [56]. To roughly demonstrate the SN detection efficiency of WFST, we focus on normal SNe Ia with well-established light curves and spectral templates. These SNe are stochastically generated at different redshift as per the event rate derived from local SN Ia samples. The SN Ia light curves are constructed through synthetic photometry using Hsiao's spectral template [57]. In regard to the dispersion in the intrinsic luminosity of SNe Ia, we assume a uniform distribution of absolute magnitude at maximum light spanning a range of -18.5 to -19.5 mag. Finally, random foreground extinction from the Milky Way and the host galaxy is configured for each SN.

In this simulation, a SN candidate is detected at least twice in different nights is defined as a "real" SN detection. Figure 1 shows the distribution of SNe Ia on the discovery magnitude vs. redshift plane based on two survey modes. Note that the time t in the figure is defined as that of the second detection of a SN. As our major targets, SNe with $t < 4$ days (early-phase SNe; solid symbols) will be intensively observed by other observing facilities within the following few months to depict detailed multi-band light curves and spectral evolution. The SNe Ia with $t < 7$ days (open symbols), mainly consisting of those for which a good coverage of multi-color light curves starting from ~10–14 days before the peak is expected, will facilitate statistical investigations of the light-curve behaviors of SNe and the SN cosmology over a wide range of redshift. In the simulated one-year WFST observation, we expect to discover over 1000 SNe Ia at $z \lesssim 0.25$ in $t < 7$ days, and particularly ~ 100 early-phase SNe Ia at $z \lesssim 0.15$ via WFST DHS. The number of early-phase SNe Ia is about three times larger than that discovered from WFST WFS, indicating the significance of a deep high-cadence survey for searching early-phase SNe (and other fast transients alike).

3.2 Tidal Disruption Events

3.2.1 Observational Status and Open Questions

A breakthrough in transient research during the past decade is the detection of a rapidly growing number of tidal disruption events (TDEs). A TDE occurs when a star occasionally wanders into the tidal sphere of a supermassive black hole (SMBH) residing in the center of a galaxy. The star will be tidally disrupted and partially accreted, producing a flash of electromagnetic radiation on timescales of months to years [58]. The event rate is lower than supernova by a factor of a few hundred, i.e. $10^{-4} - 10^{-5}$ gal^{-1} yr^{-1}, placing TDEs in a class of rare transients.

Already theoretically predicted in the 1970s, TDEs were not identified until late in the 1990s from the archival ROSAT data as well as a few more subsequent events identified by XMM-Newton and Chandra, guided by the anticipation of a radiation peak in soft X-ray or extreme UV bands. These TDEs, however, were all found serendipitously from archival data and synergetic information in other wavelength regimes is scarce. Thanks to a variety of wide-field optical surveys dedicated to time-domain surveys, an explosively growing number of TDEs have been found in the past decade (see recent review of [59]). In particular, the ZTF survey has boosted the discovery rate of TDEs from $\lesssim$2/yr to >10/yr, opening up a new era of sample statistics [60]. At present, optical TDEs are being discovered in real time, timely multi-wavelength follow-up observations therefore become feasible.

TDEs arouse broad interest in the community due to their distinctive scientific values. First of all, TDEs provide direct evidence for the existence of a SMBH in a quiescent galaxy beyond the current accessible regime that is based on stellar or gas dynamics, which is particularly useful in dwarf and distant galaxies. Even dormant intermediate-mass BHs (IMBHs) and SMBH binaries can be probed via TDEs. Moreover, TDEs serve as an ideal laboratory to scrutinize the accretion physics of SMBHs and tackle unsettled problems in AGNs by monitoring the entire life cycle of BH activity, or even by witnessing the formation of jets. The evolution of gas and the infrared and radio echoes of TDEs provide a novel tool to probe the sub-parsec environment of these distant quiescent SMBHs [61] inaccessible to other techniques. In the multi-messenger era, TDE is deemed an important astrophysical process as the origin of high-energy neutrinos[62] (see details in §3.3.4).

As significant as the scientific values and advancement, plenty of open questions about TDEs are yet to be answered. For instance, the TDEs found as yet exhibit an unexpected preference for post-starburst (or so-called "E+A") galaxies [63], which cannot be addressed by known selection effects. In addition, the observed total energy is one to two orders

of magnitude lower than theoretical prediction, leading to the "missing energy" puzzle. Also, the highly debatable origin of the bright optical-UV emission awaits more observational constraints. An associated issue is the connection between optically-selected and X-ray-selected TDEs, and the feasibility of constructing a simple model to unify them remains unclear. From an observational perspective, the mounting number of nuclear transients, both in normal and active galaxies, has raised a fundamental question: how to classify these transients (e.g. TDEs, turned-on AGNs, sporadic gas accretion, etc.) into different types of SMBH transient accretion events [64]? WFST, in synergy with other multi-wavelength/messenger time domain facilities in the upcoming decade, offers an unprecedented opportunity to tackle these (and many other) challenging questions.

3.2.2 Demography of Dormant SMBHs Revealed by Large TDE Samples

As a direct probe of SMBHs, TDEs shed light on the distribution of mass (and even spin) of dormant SMBHs, which constitute the majority of SMBHs in the low-redshift universe. However, the sample size of known TDEs is insufficient as yet ($\lesssim$100 up to now [59]) to achieve meaningful demography, an enlarged sample with improved completeness is indispensible.

The success of ZTF proves that high-cadence and multi-band observations during the same night provide critical color and evolution information that are remarkably beneficial to the TDE search. The observational feasibility is assured by the fact that TDEs exhibit evidently bluer and more steady color, distinguishing themselves from contaminating supernovae and usual variable AGN [60]. WFST has the potential to surpass ZTF by taking the advantage of the improved depth, the availability of u-band, the higher photometric accuracy and the high spatial resolution of imaging. In particular, as the optical band nearest to the peak wavelength of the TDE SEDs, the employed u-band distinguishes WFST from the other facilities that will dominate the discovery and characterization of TDEs on the northern hemisphere.

In order to assess the TDE discovery capability of WFST, we perform mock observations by taking site conditions, telescope parameters and survey strategy into account. We start from the billions of galaxies in the 440 deg^2 CosmoDC2 field [66], assign a TDE event rate to each galaxy as per its SMBH mass, and generate TDE light curves using the empirical model `MOSFiT`. We assume a uniform survey strategy, in which the experimental 440 deg^2 field is scanned with 30-second exposures every 10 days in u, g, r, i and z band, respectively. Also considered are the "observation windows" ($\sim$ 180 days per year) and the proportion of clear nights assumed to be 70% (a clear night is defined as more than 4 hour of contiguous fully clear time [16]). Besides a seeing distribution consistent with on-site monitoring, we adopt a sky background of 22.0 mag/arcsec^2 and readout noise of 10 e^-/pixel.

In our definition, the discovery of a TDE satisfies the following minimum requirements (an example g-band light curve is given in Figure 2): 1) the host galaxy is detectable in one band in the reference image; 2) the excess in the galactic nucleus is significant in 10 epochs and 2 bands. After performing 1000 mock observations, we find the combination of g and r bands to be the most effective. If we choose a more conservative strategy by using the combination of u, g, r and i bands so that comprehensive SED information is attainable (u band is particularly useful), then 29 $\pm$ 6 TDEs are detected in the CosmoDC2 field, equivalent to a detection rate of 532 ± 100 per year for the 8000-deg^2 wide-field survey. [67]

In addition to enlarging the sample size of TDEs, WFST will substantially extend the redshift range to $z \sim 0.8$, as suggested by our mock observations. After a planned 6-year survey, we expect to obtain a uniformly-selected sample of thousands of TDEs. Combined with the host galaxy properties learned from WFST stacked images and CSST high-resolution images, this sample will allow for probing the occupations of SMBHs among different types of galaxies and constraining their mass functions in the local universe, a vital step towards deciphering the formation and growth history of SMBHs.

3.2.3 Hunting for IMBHs through TDEs

SMBHs are believed to a result of growth from seeds that are significantly less massive. It is widely accepted that IMBHs lie in the mass range of $\sim 10^2 - 10^5\ M_\odot$, and were formed shortly after the formation of the first generation of galaxies. Investigations of IMBHs will undoubtedly advance our understanding of the BH family in the universe as a whole by bridging the gap between SMBHs in galactic nuclei and BHs of stellar masses in binaries. However, the paucity of unambiguously identified IMBHs and the poor understanding of their formation mechanism pose a major challenge [68].

Hitherto, the reported IMBH candidates have been exclusively noticed by their AGN features, yet their inactive counterparts are largely overlooked. The stellar TDEs produced by IMBHs may provide a unique opportunity for uncovering the dormant IMBHs, which are tentatively invoked to explain the X-ray outburst in an off-centered massive globular cluster or an ultra-compact galaxy resulting from a minor merger [69]. Besides normal (main-sequence) stars, white dwarfs (WDs) can be tidally disrupted by IMBHs, producing dis-

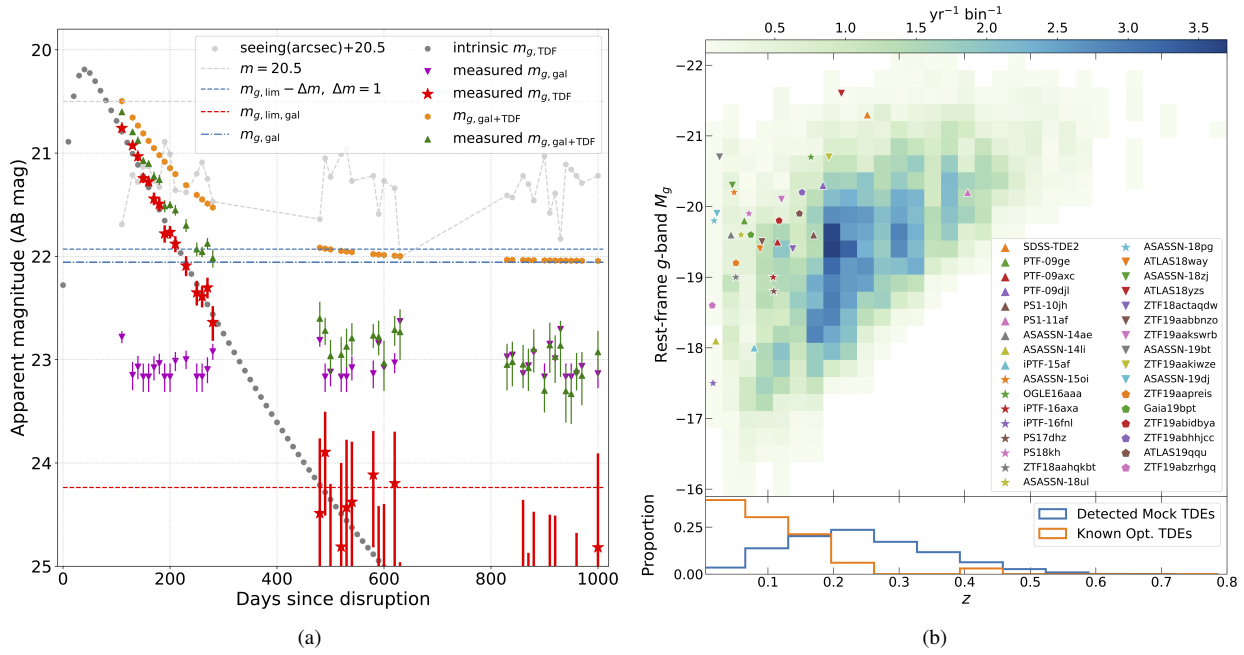

Figure 2 (a): The g-band light curves of a TDE at $z = 0.253$ as an example of our mock observations. (b) top: The peak absolute g-band magnitude (M_g) as function of redshift for TDEs detected in our mock observations. The 33 optical TDEs summarized in Table 1 of [65] have been also overplotted for comparison. (b) bottom: the histograms of TDE redshift in the mock and known sample.

tinctive features. It has been proposed that thermonuclear explosions of WDs induced by the strong tidal compression of IMBHs will manifest themselves as optical transients similar to SNe Ia [70]. Consequentially, some WD TDEs have been possibly misclassified as normal SNe Ia in the past. Distinguishing between them solely through optical emission is challenging, but they are probably featured by distinctive signatures in other bands (e.g. X-ray emission from the accretion process in the WD TDE scheme).

As introduced in §3.1.3, the understanding of the physical mechanism underlying ultra-luminous FBOTs (peak bolometric luminosity $\gtrsim 10^{44}$ erg $\rm s^{-1}$), represented by AT 2018cow, remains controversial. IMBH TDEs have been suggested as a possible scenario, though an unusually long-lasting emission of highly super-Eddington accretion is required [43]. The solution to the FBOT problem may involve a two-folded strategy: spotting them early and start prompt observations in other wavelength regimes (e.g., X-ray, radio), and performing statistical analysis based on a large sample. However, the number of AT 2018cow-like FBOTs to date remains a single digit, and enlarging the sample of FBOTs is therefore of fundamental importance. If the IMBH-TDE scenario is correct, then the ultra-luminous FBOTs are likely the most efficient and direct probe of off-centered IMBHs. The defining blue ($g - r < -0.2$ at peak) and fast-evolving characteristics of FBOTs render themselves ideal targets for DHS in u-band (see details in §2.2). In a 300-$\rm deg^2$ deep survey field, we expect tens to hundreds of FBOTs per year (aware of the large uncertainty in the event rate), making WFST one of the most competitive facilities for FBOTs-related science.

Fast TDEs with rising time ($t_{\rm rise}$) between that of FBOTs ($\sim$ 3 days) and usual TDEs ($\sim$ a month) are potentially ideal candidates of IMBHs as well, because $t_{\rm rise}$ of TDEs is correlated with BH mass in theory. The very recent discovery of a nuclear transient with a rising time of 13 days, AT 2020neh, can be plausibly explained by a main sequence star tidally disrupted by an IMBH [71] and is an exact demonstration of this strategy. The WFST deep field is capable of unveiling more fast-rising optical TDE candidates like AT 2020neh, endowing us an opportunity to explore dormant IMBHs in the centers of dwarf galaxies.

3.2.4 *Other Opportunities*

The rising phase of TDE light curves is poorly explored as yet, though it provides valuable clues to the mass of the BH and the disrupted star, and even to the BH spin. Hitherto, ASASSN-19bt, which falls luckily in the TESS field, remains the sole TDE with consecutive sampling on a daily basis allowing for depicting the light curve before its peak [72]. In the WFST and LSST era, the challenge of TDE research is distinguishing TDEs from other transients and coordinating limited follow-up observing resources for events with prominent scientific values as promptly as possible. Regular surveys at a cadence of days to weeks is not optimal for the dis-

covery of TDEs at their early rising stage, while the advantages of the planned deep high-cadence field of WFST are distinct. Our estimation shows that the emission and color of about 10 TDEs will be measurable to WFST as early as (rest-frame) 30 days before their peaks.

The overlap of WFST timeline with that of the Einstein Probe [18] is particularly engaging for TDE study, because optical and X-ray campaigns have been playing a dominant role in TDE discovery. It remains enigmatic whether TDEs bright in optical and X-ray emission belong to distinctive populations or can be described in a unified picture, where the difference is due to orientation effects, dynamic evolution or other effects. The weakness in combining the two wavelength regimes in previous TDE works is due to the shortage of dedicated time-domain surveys undertaken simultaneously in both bands. Optical TDEs unveiled in real time have been monitored in X-ray only for a short period since their discovery, yet revealed a complex relationship between X-ray and optical. The joint analysis of WFST and EP data promise to offer an unprecedented TDE sample with high-cadence light curves (or upper limits) and a solid foundation for deriving luminosity functions in the optical and X-ray bands.

Besides classical TDEs involving a star that plunges into the tidal radius, partial tidal disruption at a position barely beyond the tidal radius is also possible, in which case only the stellar envelope is stripped and ripped apart, leaving a naked compact core, which may be completely disrupted later[**?**]. The event rate of partial TDEs is naturally expected to be higher than normal ones, yet their lower luminosity pose a challenge to observations. Dozens of partial TDEs are probably detectable by the ZTF survey every year [73] but have been overlooked. The power of WFST to detect weak optical emission allow us to anticipate the discovery of a significant number of partial TDEs, but the success of this strategy likely hinges on distinguishing them from other massive nuclear transients. Partial TDE scenario is also a proposed explanation for the intriguing periodic optical flares found in galactic nuclei [74], and a potential source for low -frequency gravitational waves.

The IR echoes of TDEs have been proved effective in tracing the (sub)parsec environment of SMBHs in normal galaxies, which are otherwise extremely difficult to probe[61]. The statistics of environmental differences between quiescent and active galaxies is instrumental to revealing the triggering and fueling mechanism of AGN. However, the construction of a panorama is hindered by the strong preference of the known TDE hosts for post-starburst galaxies and thus by the absence of star-forming and passive galaxies. WFST will help construct a TDE sample with enhanced completeness by detecting a remarkable amount of optically-weak TDEs, and the analysis of dust and gas echoes based on a virtually unbiased sample will become realistic. Once completed, the upshot will be a major step towards an in-depth understanding of the pc-scale environment of SMBHs in various types of galaxies, which will ultimately facilitate the construction of a panoramic picture of the SMBH activity.

3.3 Multi-messenger Events

Stellar transients results from a variety of processes in stellar evolution, including the explosive death (e.g. SNe and Gamma Ray Bursts or GRBs), the violent behaviors of the compact remnants of the explosion (e.g. pulsars and possibly Fast Radio Bursts or FRBs), as well as processes related to the merger of binaries (e.g. Gravitational Wave Events or GWEs). Among these transients, SNe and GRBs are possibly neutrino-related events. In this section, we discuss the observation plans of stellar transients with WFST.

3.3.1 Gravitational Wave Events

The observations of GW170817 [75], GRB 170817A [76,77] and AT2017gfo [13, 14] have opened up a new era of GW multi-messenger astronomy. Electromagnetic (EM) counterparts of GWE are of fundamental importance to extreme relativistic physics and redshift measurement of standard sirens. In this subsection, we discuss the prospects of WFST in the search for optical counterparts of GWE.

Kilonovae During the coalescence of binary neutron star (BNS) and some neutron star-black hole (NSBH) binaries, neutron-rich ejecta are released through shocks at the contact interface, tidal interactions and disk outflows. The rapid neutron capture (*r*-process) nucleosynthesis renders heavy elements to form and decay in these ejecta [78], powering a rapidly evolving and roughly isotropic thermal transient "kilonova" [79].

The observations of AT2017gfo along with GW170817/GRB 170817A, have confirmed that BNS mergers produce kilonovae. Detection of kilonovae will help to locate the source, thus to measure the redshift of GW events, to explain the origin of heavy elements in universe, to probe the nature of ejecta and merger remnants, and to constrain the NS equation of state (EoS). Hereby, we simulate 10,000 BNS mergers spread over the redshift range of 0 to 0.2 to characterize the WFST detection capability of kilonova.

A binary neutron star merger, if the merger remnant is a strongly magnetized millisecond pulsar (or millisecond magnetar), is believed to result in a kilonova along with an afterglow brighter than those from the decay of radioactive heavy elements and the interaction of a relativistic jet with its ambient medium [80-82]. Observations of such transients have

posed new constraints on the EoS for dense neutron star matter, showing that the EoS therein is probably highly stiff. In parallel, the inconsistency between the Hubble constant determined from SNe Ia and that from the Cosmis Microwave Background (CMB), or the so-called "Hubble constant tension", is currently a focus of cosmological research. The electromagnetic signals together with the gravitational waves from a binary neutron star merger promises to help resolve this problem by providing an independent and unique probe of the Hubble constant [83].

During their dynamical time, BNS mergers eject neutron-rich matter through shocks at the contact interface and tidal interactions in the equatorial planes. In general, the tidal ejecta have a sufficiently low electron fraction $Y_e \lesssim 0.25$ along with production of heavy nuclei. These ejecta are lanthanide-rich, with a high opacity and known as "red" components. The polar ejecta have a larger electron fraction ($Y_e \gtrsim 0.25$) due to the effects of $e^{\pm}$ captures and neutrino irradiation. These ejecta are known as the "blue" components due to the lack of heavy nuclei synthesis and bluer colors. After the BNS merger, an accretion disk is formed around the central remnant NS or BH, while the disk loses a fraction of its mass because of the neutrino-heated winds and spiral density waves. In this case, the electron fraction and opacity of these ejecta lie between those of the "red" and "blue" components, which is therefore known as the "purple" components.

For NS (double NS or BH-NS) mergers, the binary chirp mass is among the measured parameters best determined from GW signals, while the type and mass ratio of the two companions are poorly constrained. As the ejecta properties of the kilonova are sensitive to the type of merger and the mass ratio, they are useful for diagnostics of the progenitor. The construction of more relevant samples will help us filling the gap between NSs and BHs [84]. In a double NS merger, possible remnant includes a stable NS, a supermassive NS supported by solid-body rotation, or a hypermassive NS supported by differential rotation, or a collapsing system promptly evolving into a BH, depending on the EoS and total mass of the double NS system [85].

Using the mass distribution of Galactic double NSs and EoS from GW170817/AT2017gfo constraints, we calculate the mass and velocities of the three components following [86-88]. We also derive the kilonova light curves from these samples employing the Modular Open Source Fitter for Transients (`MOSFiT`), and calculate their GW signals and the expected signal-to-noise ratio (SNR) if they are detected by the second generation (2G) GW detector network. Hereafter, we denote the network of advanced LIGO-Livingston/Handford and advanced Virgo as LHV, and the network of LHV, LIGO-India and KAGRA as LHVIK.

In Fig. 3, we show the magnitude of kilonovae at their peak luminosity and the corresponding time for BNS mergers detectable by LHV with SNR $>$ 10. The two dashed lines in each panel depict the single-visit depth of a 30s exposure for WFST and LSST. The redshift limit of LHV is $\sim$ 0.12, while WFST can observe kilonovae at a maximum redshift of $\sim$ 0.06 in r-band. As shown in the i-band panel, the time when peak luminosity is reached is concentrated around 1–3 days, a consequence of the fact that the fraction of "red"/"blue" components is strongly influenced by the mass ratio. For BNS with unequal masses, the less massive NS is tidally disrupted before contact, and the production of shocks and the "blue" components are suppressed. The "red" component has a larger opacity and it takes the photons therein more time to diffuse, so the kilonova dominated by the "red" component reaches the maximum luminosity at a later time. Hence, i-band observations allow for a deeper understanding of the color evolution of kilonova and the nature of ejecta. In Fig. 3, we further note that the u-band luminosity reaches its maximum within a few hours. Current AT2017gfo observing campaigns lack u-band imaging, and a quick WFST search in u-band facilitates investigations of the kilonova evolution within the first few hours.

Assuming a local BNS merger rate of $80 - 810$ Gpc^{-3} yr^{-1} [89], a survey area of $\sim$ 50% of the whole sky per night, and that a fraction of $\sim$ 70% are observable nights, we report the amount of BNS mergers per year with observable GW and kilonova signals in Table 2. For WFST and LHV, the rate of multi-messenger detections is $\sim 1 - 13$ per year in g- and r-bands, and is slightly lower in u and i, but z-band is likely unusable in kilonova search due to the relatively low sensitivity. We plan to focus on u- and g-bands (u in particular) campaigns in the first few hours of our kilonova search, and switch gears to r- and i-bands afterwards, especially when we optimize the search efficiency for red kilonovae [90].

Gamma-ray bursts and afterglows For high-redshift events, the expected WFST detection of EM counterparts are the short-GRBs (sGRBs) and their afterglows. However, GRB emission is beamed, i.e. the gamma-ray radiation is emitted in a narrow cone more or less perpendicular to the plane of the inspiral. Hence, only a small fraction of BNS mergers are expected to have produced observable GRBs and afterglows. In a previous work [91], we calculated the detection rate of BNS mergers observable by GW detectors, X-ray and γ-ray facilities (EP; GECAM; Swift-BAT; SVOM-ECLAIRS; Fermi-GBM), and optical telescopes (WFST, LSST) hunting for their afterglows. We simulated 10^7 BNS mergers in the redshift range of 0–0.3 and assumed a Gaussian-shaped jet profile for all of them [92], which is supported by that of GW170817/GRB 170817A.

In Table 3, we list the rate of multi-messenger detections

		u	g	r	i	z
WFST	LHV	0.6-5.8	1.1-11.6	1.3-12.9	0.8-8.5	0.2-2.4
	LHVIK	0.8-7.9	1.8-18.2	2.0-25.2	1.1-11.8	0.3-2.9
LSST	LHV	1.5-15.3	1.8-17.9	1.8-18.0	1.8-18.0	1.6-16.8
	LHVIK	2.9-29.0	3.8-37.9	3.8-39.0	3.8-39.0	3.2-32.7

Table 2 Number of BNS mergers per year with observable GW signals and kilonova.

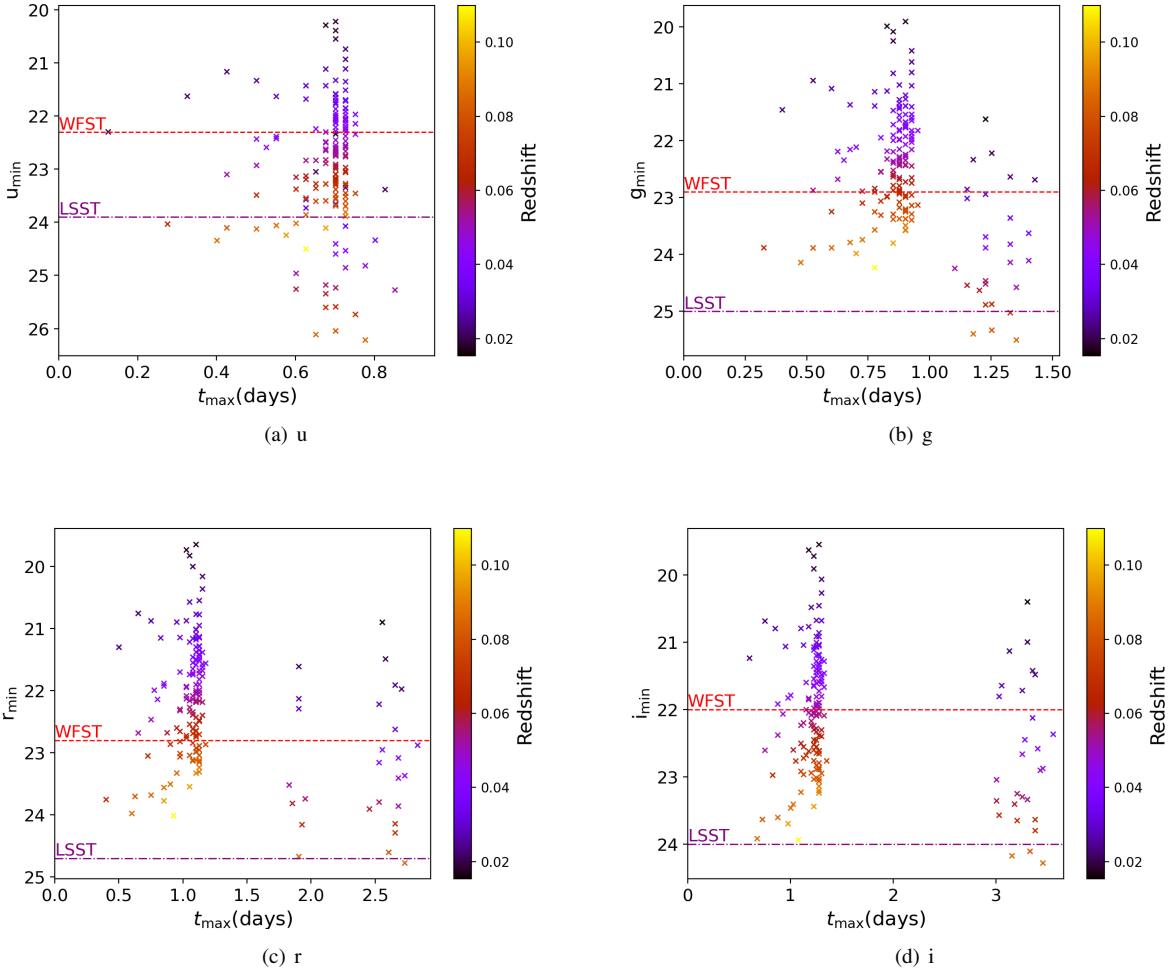

(a) u (b) g

(c) r (d) i

Figure 3 The distributions of magnitudes of kilonovae at their maximum brightness and the corresponding times for BNS mergers with GW SNR> 10. Colors depict redshifts of sources. Five panels represent the results of *u*-, *g*-, *r*-, *i*-bands, respectively.

per year. For the case of LHV, this rate is 0.042-0.425 per year when Swift-BAT is involved and is 0.072-0.731 per year if SVOM-ECLAIRS is at work. For the case of GECAM and Fermi-GBM, the rate is a few times higher due to their significantly larger survey areas. In spite of its better sensitivity, the EP result is slightly worse than Swift-BAT due to its smaller survey area. When Kagra and LIGO-India are added, LHVIK renders a rate about twice higher than LHV. We select here the BNS samples that can trigger both GW interferometers and γ-ray detectors, adopt the GECAM result as fiducial, and summarize the distribution of the BNS redshift and inclination angles (ι) in Fig. 4.

After that, we employ the standard afterglow models [93] to estimate the afterglow magnitudes at r-band. When the Lorentz factor γ drops below the half-opening angle θ_j of a jet, the jet materials begin to spread sideways, such a phenomenon is known as "jet break". For an on-axis observer, the light curve consists of two power-law segments connected at the jet-break time; as for an off-axis observer, the light curve reaches a peak after the jet break time and displays a power-law decline ever since. For off-axis GRB samples, we can calculate the peak magnitudes of afterglows in r-band; but for the on-axis case, the afterglows decay with time in the power-law manner, rendering r unattainable from their light curve. In the latter case, we adopt the r-band magnitude at the jet-break time, instead. r values are exhibited by the colorbars in Fig. 4. Our work demonstrate that the afterglows under consideration are all detectable by WFST. After accounting for the fractions of observable area and time, we find the joint observation rate of sGRBs and afterglows to be less than ~2 per year, remarkably lower than that of kilonova. Therefore, our WFST searching programs for GW EM counterparts will be focused on kilonovae.

Optical counterparts of other GW events Kilonovae and optical afterglows from BH-NS mergers are another type of multi-messenger sources that we expect to discover with WFST. The two events, GW200105 and GW200115, followed by several other candidates, GW190426, GW190917, GW191219, GW190814, GW200210, were discovered during the third observing time (O3) of the LIGO Scientific Collaboration and Virgo Collaboration (LVC). Unfortunately, no electromagnetic counterpart was identified. A number of works made efforts to explain the lack of EM identification in theory (e.g. [94]). The EoS of NSs, the spin of BH and the mass ratio of the binaries have been found to significantly influence the kilonova luminosity function and the EM detection through their parameter distributions. In the case of a primary BH with a high-spin distribution and its NS companion being less massive with a stiff EoS, the NS is expected to be disrupted by the BH in nearly every case, powering a bright kilonova and an afterglow. In an optimal estimation, WFST will detect this kind of optical counterparts at a rate of round $O(1)$ per year [94].

Binary black hole (BBH) mergers also produce EM radiation in some special cases, e.g. the BH has the electric charge or the BBH resides inside the accretion disk of a galaxy. The event GW190521 is possibly the first multi-messenger observation of a BBH event. Detection of an electromagnetic signal has been reported as ZTF19abanrhr by the Zwicky Transient Facility (ZTF) in a sky area consistent with that initially reported by the LVK in an early warning, rendering it a candidate counterpart to GW190521 [95]. A flare peaking at ~50 days after the trigger of GW caused a flux elevation of ~0.3 mag that sustained for ~50 days, assuming a typical bolometric correction factor for quasars. The EM flare is consistent with the expectations for a kicked BBH merger residing in the accretion disk of an active galactic nucleus, which potentially has paramount implications in interpreting GWs from compact mergers, forecasting future counterparts and measuring the Hubble constant. EM campaigns as follow-up observations of GW alerts are planned to monitor AGN at multiple cadences, from days to weeks, to optimize the efficiency of searching for EM counterparts in the AGN channel.

It is challenging to quantify the detection rate of optical counterparts for these GW events as a result of the perplexing parameter dependence. For WFST, the GW-triggered target-of-opportunity observations are instrumental to demystify the formation and evolution of these events.

3.3.2 Gamma-ray Bursts

Gamma-ray bursts (GRBs), the most energetic stellar explosions in the Universe, are relativistic beaming of jet emission towards the observer. The jet is launched by a compact central engine, being either a BH or a rapidly rotating and highly magnetized NS. No thorough consensus of GRB jet properties (e.g., jet composition, emission radius) exists as yet. The temporal/spectral evolution of the prompt/afterglow emission brings up the primary clues to investigating the GRB jets. A statistically significant sample of GRB prompt/afterglow light curves is fundamental to pinning down the jet properties, necessitating wide-field surveys of the optical counterparts of GRBs.

The Early Optical Afterglow Multi-wavelength observations of GRB afterglows in the past years has led to the construction of the standard external shock scenario [96, 97], in which the interaction between the blast waves and the surrounding medium heats up the ambient electrons to emit broadband afterglows in the form of synchrotron radiation. In observations, the optical afterglow typically commences

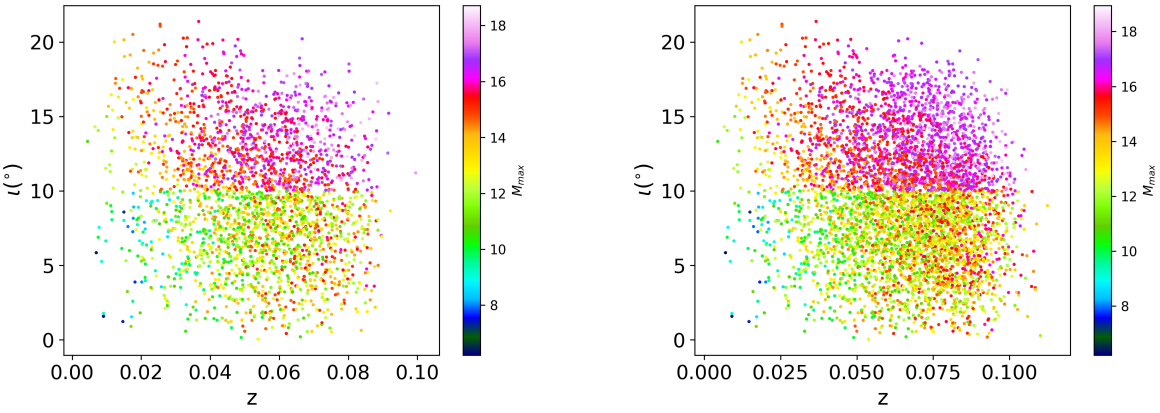

(a) LHV (b) LHVIK

Figure 4 The distributions of inclination angle, redshift of BNS samples and their afterglow fluxes, which can be triggered by GW detectors and GECAM. The colorbars show their r-band magnitude of afterglows with $\theta_j = 10°$ [91].

	Swift-BAT	SVOM-ECLAIRS	GECAM	Fermi-GBM	EP
LHV	0.042-0.425	0.072-0.731	0.278-2.820	0.198-2.001	0.029-0.297
LHVIK	0.084-0.856	0.146-1.474	0.553-5.598	0.394-3.985	0.058-0.593

Table 3 The expected detection rates (in unit of year^{-1}) of multi-messenger sources of BNS mergers via synergy of ground-based gravitational wave detectors and various γ/X-ray large field telescopes.

at a time of 10^3 s after the GRB trigger, mainly because of the difficulty of timely optical follow-ups after a GRB is detected. Hence, the early stage (within 10^3 s) of a GRB afterglow, namely the early optical afterglow, is often missed. A wide-field survey of the GRB optical afterglow promises to expand the sample of early optical afterglows and improve our understanding of GRB jets. Late-stage optical afterglows are crucial in constraining the structure of the relativistic jet launched from the central engine and the density of the ambient environment[98, 99], early optical afterglows, in parallel, are a unique probe to unravel the composition of the jets and to clarify whether baryons or magnetic fields are playing a dominant role therein [100-102].

When a jet interacts with its surrounding medium, two shocks develop simultaneously, one propagating outwards into the external medium (the "forward shock"; FS) and the other traveling backwards into the jet (the "reverse shock"; RS). Consequent bright optical flashes from the RS in the early episode are predicted on a theoretical basis [103-107], though the early optical afterglows of a few GRBs have shown evidence for an additional emission component arising from a strong RS [108, 109]. Using a series of numerical methods to solve the dynamics of an FS–RS system proposed in previous works [110-114], we relate the contribution of the RS emission in the early afterglow to the magnetization parameter of the GRB jet, i.e., $\sigma = B_0^2/(4\pi\rho_0 c^2)$, where both the magnetic field B_0 and the fluid density ρ_0 are defined in the comoving frame of the fluid. A set of numerical multi-wavelength light curves from the FS-RS system are given in Figure 5. The emerging RS emission renders early-stage light curves that deviate from those produced in the simple external shock scenario. Meanwhile, our results show that the RS emission is a significant contribution for ejecta with σ over the range of 0.1–1, and is dominated over by the FS emission otherwise. This is because at an early stage, the weak magnetic field inhibits the synchrotron radiation for $\sigma \ll 1$, whereas the strong magnetic field acts as a relaxant that weakens the RS itself for $\sigma > 1$. Therefore, observations of a substantial sample of early afterglows will constrain σ of GRB jets with statistical significance.

In our WFST surveys, the sensitivity limit lies safely below the early RS flux of a typical GRB, and the FoV can cover the uncertain region of the GRB location within several pointings, demonstrating WFST's capability to capture early afterglows. When a GRB trigger notice is reported by a space-borne wide-field gamma-ray detector (e.g. Fermi, GECAM [115] or SVOM[116]), a timely follow-up to the burst with a relatively small localization uncertainty in the gamma-ray may detect optical signals as promptly as possible. Fermi/GBM report ~300 GRBs per year on average,

among which at least 10% reside within the survey area of WFST (with site conditions and the fraction of observable nights taken into account). We plan to observe the targets with a position uncertainty of less than 10 degrees (corresponding to a fraction of $\sim$ 37%) following the first notice of Fermi. With an exposure of 30 seconds for each pointing, our simulation shows that, for these target candidates, the possibility of spotting the rising phase of the early afterglow is ~22%. As a result, we expect WFST to capture ~2–3 golden early afterglows per year. As a more optimistic consideration, the SVOM satellite to be commissioned in 2024 is expected to report $\sim$ 70 GRBs with a localization error of ~10 arc minutes, rendering a higher WFST detection rate of ~7 golden early afterglows per year.

High-redshift Gamma-Ray Bursts Thanks to the combination of their extreme brightness with the spectroscopy of the optical afterglows, GRBs are detectable up to high redshift, as already demonstrated by the cases of GRB 090423 at $z \sim 8.2$ [117, 118] and GRB 090429 at $z \sim 9.4$ [119]. As bright beacons in the deep Universe, GRBs are viewed as a complementary, and to some extent unique, probe to the early Universe. Statistical analysis of high-redshift GRBs may shed light on the cosmic expansion/dark energy, the cosmic star formation rate, Population III stars, the reionization epoch, the metal enrichment history, among other themes of fundamental importance (for a review, see [120, 121]).

During its fifteen years of operations, *Swift* only detected 9 GRBs at $z > 6$, though the redshift is spectroscopic in 5 cases, leaving the others photometric. In spite of the paucity of confirmed high-z GRBs in the *Swift* era, theoretical models predict that bursts at $z > 6$ represent more than 10% of the whole population, implying that GRBs are efficient for sampling high-z objects [122, 123]. A prerequisite of further exploiting the potential of GRBs as a cosmological probe is the construction of a larger sample of high-z GRBs. The optimal strategy for detecting the largest possible amount of high-z GRBs is to design a facility operated in soft X-ray with a high sensitivity [120, 123]. Correspondingly, the Einstein Probe (EP) to be operated in the 0.5–4 keV energy band reaching an unprecedentedly high sensitivity of 10^{-10} erg s^{-1} cm^{-2} in an exposure of 10 s is expected to detect $\sim$ 20 GRBs yr^{-1} sr^{-1} at $z \geq 6$, or $\sim$ 6 GRBs yr^{-1} sr^{-1} at $z \geq 8$ [124]. Once high-z GRBs are detected, the first and foremost issue is to measure their redshift, but the optical afterglows of GRBs fade so rapidly that a few hours later they commonly become too faint to permit accessing the redshift. Timely world-wide distribution of the EP alerts allows for coordination of follow-up optical campaigns. We expect WFST to contribute to the process of prompt identification of high-z candidates that deserve deep spectroscopy in the near IR by endowing follow-up multi-color images that facilitate photometric redshift estimates. In the EP era, the combination of the fast visible/NIR photometry using WFST and the subsequent deep spectroscopic measurements using larger ground-based telescopes will enable a highly efficient pipeline-wise identification of GRBs at $z > 6$.

3.3.3 Fast Radio Bursts

Fast Radio Bursts(FRBs) are cosmological millisecond duration radio transients[125], of which some repeat but others apparently do not[126, 127]. As of 2021, hundreds of FRBs have been reported [127], of which 18 with their host galaxies identified have been localized within arcseconds [128, 129]. The comparison between the host galaxies and sub-galactic environments has demonstrated that the surrounding environment of FRBs are similar to that of core collapse SNe (CCSNe), type Ia SNe and short-duration GRBs (SGRBs), but dissimilar to that of long-duration GRBs (LGRBs) and superluminous SN (SLSNe) [130, 131], indicative of an association of the progenitors of FRBs with those of CCSNe or SGRBs. This association is (at least partially) confirmed by the discovery of FRB 200428, an FRB from the Galactic magnetar SGR1935+2154 [132-134] in association with a supernova remnant (SNR). Hence, whether all FRBs originate from CCSNe-associated magnetars, or to be more specific, whether repeating FRBs and apparently non-repeating FRBs have the same origin, are the most appealing questions awaiting to be addressed. We anticipate that WFST surveys will help tackle these themes from the respect of their host galaxies and optical counterparts.

Host Galaxy The similarity of host galaxy and sub-galactic environments hints for an association of FRBs with other transients. As mentioned above, the number of identified FRB host galaxies as yet is 18, hosting 7 repeating FRBs and 11 apparently non-repeating FRBs. The limited sample size severely hinders in-depth investigation, rendering the proposed models on the mechanism and origin of repeating and non-repeating FRBs indiscernible. Localizing FRBs into arcsecond precision requires wide-field radio arrays as powerful as the Australian Square Kilometre Array Pathfinder (ASKAP). The Square Kilometre Array (SKA), the Five-hundred-meter Aperture Spherical radio Telescope (FAST) and the Canadian Hydrogen Intensity Mapping Experiment (CHIME) promise to deliver a detection rate ~100 yr^{-1}, if an yearly observing time comparable to that of ASKAP is assumed. The deep imaging of WFST on the northern hemisphere will set signposts for scrutinizing the FRB host galaxies. To assess the possibility to distinguish between repeating and non-repeating FRB host galaxies, we enlarge the FRB

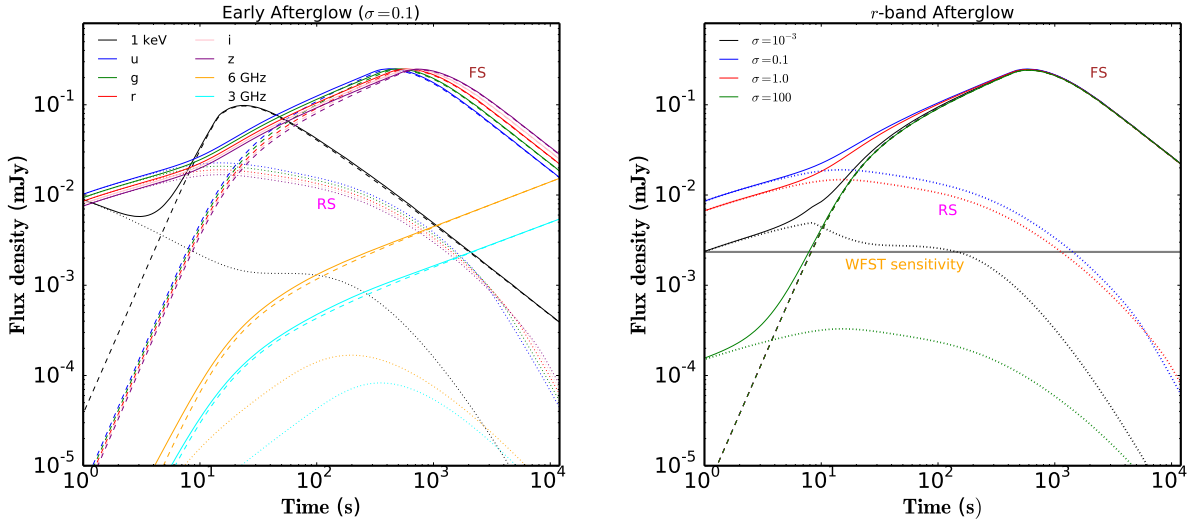

Figure 5 Left: The multiwavelength afterglows of an FS-RS system with $\sigma = 0.1$ as an example of predicted observations of a GRB jet at a redshift of $z = 1$. The initial jet parameter values are $E_{\rm K,iso} =$ erg (isotropic-equivalent kinetic energy), $n = 1$ cm^{-3} (circumburst density), $\Gamma_2 = 200$ (bulk Lorentz factor of the FS), and $\Gamma_4 = 10^4$ (bulk Lorentz factor of magnetized ejecta), the FS microphysical parameters are $\varepsilon_{\rm e} = 0.1$ and $\varepsilon_{\rm B} = 0.01$. The dashed and dotted lines present emissions from the FS and the RS, respectively. The solid lines are the total flux. Right: The r-band lightcurves of FS-RS systems with different values of σ. Other parameters used are the same as those for the left panel. The grey horizontal line exhibits the sensitivity of WFST with an exposure of 30 s.

host galaxy sample size to 72 by resampling the known FRBs [2)] and perform Kolmogorov–Smirnov tests on the host properties of repeaters vs. non-repeaters, including the stellar mass, the star formation rate (SFR), the specific star formation rate (sSFR) and the galactocentric offset of the FRBs. As a result, we find the probability of repeaters/non-repeaters drawn from the same sample to be less than 0.05. Hence, we conclude that a FRB host galaxy sample made available by the deep imaging of WFST and an enlarged FRB sample with arcsecond-localization from future radio telescope arrays will allow for distinguishing the repeating and non-repeating FRBs, if they originate differently.

Optical Counterparts As elusive as the engine and the emission mechanism of FRBs, a number of models have predicted multi-wavelength counterparts [135, 136] detectable in future WFST surveys. The mechanisms producing FRBs, the curvature radiation or maser, may also produce prompt optical radiation with a milli-second duration similar to those of FRBs. During their propagation towards the earth, the FRB photons may be inverse Compton scattered by high energy electrons into optical bands. If the electrons are from the magnetosphere of a magnetar, or if the FRB is produced by maser, then the duration of this optical signal is similar to that of FRBs; but if the FRB is surrounded by SNRs filled up with high energy electrons, the optical counterpart may last, instead, thousands of seconds [136]. Furthermore, when an outflow accompanies the FRB, a phenomenon evidenced by a pair of X-ray counterparts detected in the Galactic FRB 200428 [137], the interaction between the outflow and the interstellar medium (ISM) produces optical afterglows. Dependent on the energy of FRBs, the timescale of optical afterglows is of the order of an hour [135].

Theoretical models predict that the optical-to-radio flux ratio $\eta_\nu = f_{\rm opt}/f_{\rm radio}$ of FRBs ranges from $< 10^{-11}$ to 0.1 [136, 138, 139], and the optical radiation most detectable by WFST results from the inverse Compton scattering of FRBs inside a neutron star magnetosphere or an SNR, which typically yields $\eta_\nu = 5 \times 10^{-5}$ and 10^{-4}, respectively. Assuming an FRB to last 1 milli-second, the FRB fluence function from CHIME observations leads to the flux function $N(> f_{\rm radio}) = 818^{+229}_{-210}(\frac{f_{\rm radio}}{5\ {\rm Jy}})^{-1.4}$ sky^{-1} day^{-1}. The WFST detection rate of an FRB optical counterpart is thus estimated by $N = N_{\rm FRB}(> f_{\rm opt}/\eta_\nu) * {\rm FOV}$, where $f_{\rm opt} = t_{\rm FRB,o} f_{\rm opt,30}/t_{\rm obs}$ for a counterparts with a duration $t_{\rm FRB,o} < 30s$, $f_{\rm opt,30}$ is the 30s exposure r-band detection limit of WFST, and a 7 deg^2 FoV is applied. As a result, the event rate of the ms optical counterpart produced by magnetospheric IC is estimated to be 0.02 yr^{-1}, while the optical counterpart lasting for hours produced by FRB-SNR IC is 200 day^{-1} in an ideal case. It should be noted that $\eta_{\rm nu} = 10^{-4}$ used here is largely an upper limit with significant uncertainty, and the fraction of FRBs that are surrounded by SNRs is unknown. Moreover, an optical counterpart with a duration of an hour is often difficult to confirm, because normal surveys only record one observing point, and coordinated radio observations are required to

2) https://frbhosts.org/

complete the confirmation. The result of WFST surveys will have profound implications to FRBs, because an unambiguous detection of their optical counterparts will open up a new window for this frontier, whereas no detection also delivers constraints to the present models [139, 140].

In addition, other transients probably associated with FRBs include CCSNe (if the origin is young magnetars produced by CCSNe), gravitational wave signals and SGRBs/kilonovae (if the origin is magnetars produced by merger of compact stars). The data archive yielded by WFST surveys will be a valuable legacy for future exploration of the FRB-transient association.

3.3.4 Optical Counterparts of High-energy Neutrinos

When particles are accelerated in an astronomical object (e.g. by terminal shocks), the interaction between the accelerated cosmic rays and the surrounding matter or target photons often produces high-energy neutrinos and photons. The electromagnetic counterparts of high energy neutrinos are instrumental to the identification of candidate neutrino sources, the determination of the distance to these sources, the exploration of their properties, and our understanding of the acceleration and radiation mechanisms therein, highlighting the necessity of searching for electromagnetic counterparts or transients in coincidence with neutrinos temporally and spatially.

To date, high energy neutrinos have been detected by large neutrino telescopes settled in water (ANTARES [141], Baikal-GVD [142]) and ice (IceCube [143]), and by the Auger surface detector and ANITA at high altitude [141]. The IceCube neutrino observatory, the largest neutrino detector hitherto, detected TeV-PeV astrophysical neutrinos in 2013 [144], of which the origin remains under debate. Since 2016, the IceCube neutrino observatory has been releasing public real-time alerts on single muon neutrino-induced track events with a highly possible astrophysical origin via the Astrophysical Multi-messenger Observatory Network (AMON) and the Global Cycling Network (GCN). The IceCube neutrino alerts include "gold type" and "bronze type" notices with the chance of astrophysical origin larger than 50% and 30% and the detection rates are about 12 yr^{-1} and 16 yr^{-1}, respectively. The uncertainty in anchoring the direction of neutrinos ranges from 0.2° to 0.75°.

In their optical real-time follow-up (OFU) program, the IceCube team delivers real-time alerts to the Robotic Optical Transient Search Experiment (ROTSE) and the Palomar Transient Factory (PTF) [8, 145] to start a search for the optical counterparts, and the triggered observations are supplemented by a retrospective search in the wide field survey data of Pan-STARRS1 [10, 146]. Consequentially, electromagnetic instruments all over the world point to the direction of the neutrino events and conduct follow-up observations in energy bands and messengers ranging from radio, optical, X-ray to GeV/TeV photons and gravitational waves, whose results are then reported on the GCN. Follow-up GeV, X-ray and optical observations of alert neutrinos have revealed BL Lacs, flat spectrum radio quasars (FSRQs), TDEs, among others [62, 147, 148].

As the neutrino events detected on the southern hemisphere are highly contaminated by the muon backgrounds, the alerts released by IceCube are due to neutrinos from the northern hemisphere or the vicinity of the equator, to which IceCube has higher sensitivity. Residing on the northern hemisphere and possessing a sufficient FoV to cover the area of angular uncertainty for most neutrino events detectable by IceCube in a single exposure, WFST will serve as an ideal follow-up optical facility. Meanwhile, the optical time-domain surveys by WFST will discover more SNe, FBOTs, TDEs, GRBs and AGNs, allowing cross-identification between the detected neutrinos (real-time or archival) and WFST's legacy data. WFST surveys also promise to help identify neutrino sources and further constrain the acceleration mechanism of cosmic rays, the radiation mechanism of neutrinos, the redshift and other properties of the sources of scientific interest.

Blazars Blazars are featured by their relativistic jets driven by SMBHs with the direction aligned with the observer's line of sight. Blazars will comprise an important part of WFST targets, as will be discussed in Section 3.4. These jets may accelerate cosmic rays to high energy, and the interaction between energetic cosmic rays and target photons or matter in or near the acceleration sites may produce high-energy neutrinos and photons. Hence, blazars have been proposed to be high-energy neutrino sources [149].

On September 22, 2017, the IceCube observatory reported a track-like neutrino event (IceCube-170922A) as energetic as about 300 TeV. Follow-up observations found this event to be spatially and temporally associated with the optical-TeV active blazar TXS 0506+056 [150] with a significance of 3σ. The optical follow-up observations were performed by observatories around the world, including ASASSN, the Liverpool Telescope, the Kanata Telescope, the Kiso Schmidt Telescope, the Southern African Large Telescope (SALT), the Subaru telescope and the VLT/X-shooter. The spectra, light curve and polarization were obtained, while the redshift was constrained by optical spectroscopy from the Liverpool, Subaru and VLT telescopes before the determination made by the Gran Telescopio Canarias (GTC). It was the first time to reveal the association between neutrinos and point sources at a high significance level. The potential association between the activity of TXS 0506+056 and the neutrino event renders it a

promising candidate source of high energy neutrinos. A 3.5-σ excess of high-energy neutrino events with respect to the atmospheric background was later identified in the direction of TXS 0506+056 prior to the IceCube-170922A alert [147]. The blazar-neutrino association is supportive to the scenario that AGNs can accelerate highly energetic cosmic rays and produce neutrinos during photohadronic or hadronuclear interactions [147, 150].

In addition the follow-up of real-time neutrino triggers, in a sample of muon track neutrino events that happened between April, 2012 and May, 2017, 11 significant neutrino flares have been found to be associated with 10 AGN counterparts, including FSRQs, BL Lacs and radio galaxies [151]. Furthermore, 9 blazars are in possible association with single high-energy neutrino events, as per an analysis of both archival and alert neutrino events [148].

GRBs and SNe GRB/SN jets are believed to accelerate cosmic rays and produce high-energy neutrinos through interactions of cosmic rays with target photons or the surroundings [152]. Neutrinos may also be produced when shock-accelerated cosmic rays interact with matter and photons during the shock breakout phase of SNe. WFST's capability of detecting early phase SNe will help pin down the exploding time of SNe and probe the association between SN SBOs and neutrinos.

Alternatively, if these jets fail to break out through the stellar envelope (e.g. in red/blue supergiant stars), neutrinos and gamma-rays are produced in the interaction between accelerated protons and thermal photons in the jets choked in the thick stellar envelope or the extended material. The duration of the central engine may be longer than that of long GRBs [153, 154]. Since neutrinos and gamma-rays are produced inside the stellar envelope, the source is opaque to gamma-ray photons but transparent to neutrinos. Hence, the lack of association between the observed GRBs and IceCube neutrinos as well as the tension between the diffuse gamma-ray observations and neutrino observations can be explained. Because a Type II SN is predicted to explode a few hours after the neutrino emission, once an SN spatially associated with neutrinos is spotted, we can trace back to measure the SN explosion time using the observed SN light curve, and measure the time interval between the neutrino burst and the SN explosion.

Furthermore, as discussed in Section 3.1, some subclasses of SNe are powered by the interaction between the ejecta and the CSM or the companion (e.g. SNe Ia-CSM, SNe IIn, FBOTs and SLSNe). The terminal shocks produced by the ejecta-CSM interaction can accelerate cosmic rays to high energies. The cosmic ray-CSM interaction may result in high-energy neutrinos, rendering the above subclasses of SNe possible optical counterparts of high energy neutrinos.

A real-time program is operated by IceCube to search for muon-neutrino doublets or multiplets. To keep the atmospheric background under control, two or more muon neutrinos detected within a time interval of 100 seconds and within an angular distance of $< 3.5^\circ$ are required to trigger a doublet or multiplet alert. In March, 2012, a neutrino doublet alert was triggered: a Type IIn SN PTF12csy at a distance of about 300 Mpc was found to be 0.2° away from the neutrino alert direction (with an error radius of 0.54°), and a posteriori significance of the chance detection of the neutrino doublet and the SN was 2.2σ [155]. Nevertheless, the SN was at least 169 days old, and no long-term signal of neutrinos was found over the year, suggesting that the doublet was likely uncorrelated with the SN. On February 17, 2016, the IceCube real-time neutrino search identified a triplet with three muon neutrino candidates arriving within 100 sec between one another, with a probability of detecting at least one triplet from atmospheric background of 32%. However, no likely electromagnetic counterpart was detected[156]. The above multiplet alert was selected under the assumption that the duration of neutrino bursts from transients (e.g. GRBs or CCSNe) is shorter than 100 seconds, a typical duration of long GRBs. However, as mentioned above, in the chocked jet models or the interaction powered SNe, the duration of neutrino bursts may be longer.

The detection of early-phase SNe by WFST will help pin down the exploding time of SNe readily, allowing us to search for SNe associated with neutrinos in the WFST's archival data by assuming a certain time lag between the SNe explosion and neutrinos. Investigations of associations between GRBs/SNe and neutrinos will provide more clues on progenitor stars and the radiation mechanisms.

TDEs TDEs may generate a relativistic jet or outflow that accelerates cosmic rays to high energies. Neutrinos may be produced when cosmic rays interact with target photons or matter. In a systematic search for optical counterparts to high-energy neutrinos with ZTF [62], TDE AT2019dsg was found to be associated with a ~ 0.2 PeV neutrino IC191001A with a chance probability of about $0.2\% - 0.5\%$. AT2019dsg was discovered by ZTF six months before the detection of IC191001A, and was later classified as a TDE by ePESSTO+ based on its optical spectrum. As mentioned in Section 3.2.4, being significantly more sensitive than ZTF, WFST promises to capture faint TDEs at earlier stages to construct a TDE sample with higher completeness, and to discover more candidate associations between TDEs and neutrinos that will facilitate in-depth investigations.

3.4 Active Galactic Nuclei

Residing in the centers of active galaxies, the luminous quasars, or active galactic nuclei (AGNs) in general, are the manifestation of gas accretion onto massive black holes (BHs) and are believed to play a key role in regulating the evolution of massive galaxies. Despite that the accretion-BH scenario of the central engine of AGNs has been established since the discovery of quasars over sixty years ago, many fundamental questions remain unresolved. For instance, how do SMBHs acquire their gas? What mechanism is responsible for their variability over a wide range of wavelength? Are their activities triggered in a persistent or an episodic mode, and what are the conditions at work, in either case?

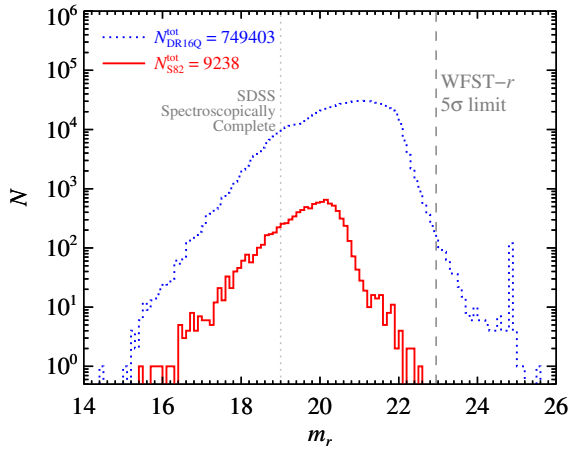

Figure 6 Distributions of the apparent r-band magnitudes for spectroscopically confirmed quasars in the Stripe 82 (S82; red solid histogram; [157]) and in the SDSS 16th data release quasar catalog (DR16Q; blue dotted histogram; [158]). Note that only quasars with physical r-band magnitudes are used here. Shown for comparison are the spectroscopically complete limit of $\sim$ 19 mag for SDSS quasars (light-gray dotted vertical line) and the WFST r-band 5σ detection limit of $\sim$ 22.9 mag in a single 30-sec exposure (gray dashed vertical line).

The ongoing and upcoming intensive time-domain surveys are instrumental to decipher the mysteries about AGNs, which are predominantly spatially unresolvable. Illustrated in Figure 6, the up-to-date SDSS survey has spectroscopically confirmed nearly $\sim$ 0.75 million AGNs over $\sim$ 10,000 deg^2 primarily in the northern sky (SDSS DR16Q; [158]), while only $\sim$ 1% of them in the well-known Stripe 82 (S82) region of $\sim$ 290 deg^2 in the southern Galactic hemisphere along the celestial equator have decade-long light curves in five bands (*u, g, r, i, z*), which are mapped 8 times on average in a 2-to-3 months duration per year between 2000 and 2008 [157]. Later on, there have been several completed or ongoing time domain surveys over the SDSS footprints, which are, however, largely with insufficient sensitivity to detect the majority of faint SDSS quasars and/or with fewer passbands than SDSS. For instance, the CRTS survey operated in 2005–2013 covered $\sim$ 26,000 deg^2 in a single broad V-band and reached typical detection limits of $\sim$ 19 – 20 mag (CRTS DR2; [7]). In 2009–2013, deeper PTF/iPTF surveys in g- and R-bands reached a depth of $R \sim$ 21.0 mag (PTF DR3; [145]). The ongoing ZTF survey has been releasing *g, r, i* images with a depth of $r \sim$ 20.5 mag since March, 2018 (ZTF DR8; [159]). The 3π Steradian Survey conducted by the Pan-STARRS1 (PS1) team between June, 2009 and March, 2014 in five passbands ($g_{\rm P1}$, $r_{\rm P1}$, $i_{\rm P1}$, $z_{\rm P1}$, $y_{\rm P1}$) reaches a 5σ depth of $r_{\rm P1} \sim$ 21.8 mag (PS1 DR2; [160]). Considering the same five passbands as SDSS and a 5σ detection limit of $r \sim$ 22.9 mag in a 30-sec single-epoch exposure (Figure 6), we expect the WFST DHS and WFS surveys provide decade-long light curves in five passbands for nearly all SDSS quasars, of which a significant amount is not observable by LSST on the southern hemisphere. Furthermore, the WFST surveys will extend the preexisting light curves to several decades for the quasars located in S82 and in the ten medium deep fields of PS1, contributing a highly valuable WFST legacy to the AGN community.

These new decades-long light curves will allow the physical origin of AGN variability to be explored both over longer timescales and towards the fainter end where BH masses lower than currently accessible are found. The increase of time baseline will lead to an increasing possibility of identification of new types of rare AGN associated events. Thanks to the upcoming deep and high-resolution WFST images, constructing a sample of considerably close AGN pairs is foreseeable by virtue of the unique AGN colors, such that inspection of the triggering mechanism of AGN activity is made possible. In addition, the long-term variability as well as the deep WFST stacked images (to a depth of $r \sim$ 25 mag) will be of service to identify and characterize quasar candidates fainter than the the completeness limit of SDSS spectroscopy. These quasar candidates will then be readily observable targets for subsequent major spectroscopic programs (e.g. LAMOST-II and MUST) that explore even fainter AGNs at high redshift with lower BH masses with an ultimate goal of attaining a panoramic view of the BH growth and its co-evolution with galaxy and tracking down the cosmological evolution of the intergalactic medium and the large-scale structure of the universe. Several relevant science cases are elaborated as follows.

3.4.1 Physical Origin of AGN Optical Variability

The AGN variability in optical is suspected to be driven by X-ray reprocessing [161], accretion disk turbulence [162], or corona heating [163], but the physical origin remains largely unclear. Hitherto, no self-consistent physical model has been validated by all relevant observations, because of the perplex-

ing accretion physics involved and the large observational uncertainties. The decades-long light curves from the WFST legacy survey will help improve the observational precision by conducting single-band and inter-band measurements of the variation.

Correlations In general, AGN variability appears aperiodic or even stochastic in single-band observations [164], though it can be described by a characteristic timescale and a long-term variation amplitude on a statistical basis [165]. Hence, scrutinization of the correlations between these two and other observational or physical parameters of AGNs (e.g., wavelength, redshift, BH mass, bolometric luminosity, Eddington ratio, metallicity, X-ray loudness, radio loudness, and the strength of emission lines) promises to shed light on the mysteries about AGN structure and accretion physics. In particular, the correlation between the BH mass and the slope of variation amplitude to wavelength is a promising alternative method for BH mass estimation (M. Y. Sun et al. in preparation). A recently proposed approach to measure the density of gaseous outflow based on variability of broad absorption lines also hinge on accurate measurement of AGN light curves [166]. Accurate measurement of the timescale and the variation amplitude is therefore a primary goal of AGN science in the time-domain era. The WFST legacy survey extending the preexisting quasar light curves to several decades will help pin down accurately the variation timescale up to a number of years.

Coordination and timelags Despite that single-band quasar light curves appears stochastic, inter-band variations sometimes demonstrate well-established coordination, where brightening or dimming in phase across optical to UV wavelengths (and even X-ray bands) is seen. In addition, variations at longer wavelengths lags behind those at shorter wavelengths, a phenomenon termed as the inter-band timelag. Uncorrelated variations [168] and the failure of recovering lags for the vast majority of AGNs seen in the Dark Energy Survey fields are also reported [169]. Regardless of the complication, the inter-band timelags derived from optical continuum variations of AGNs are used to estimate the size of accretion disks [170], under the assumption that the inter-band timelags are closely related to the difference of light travel time among different disk regions irradiated by the central X-ray corona. However, this assumption is under debate as the role of X-ray reprocessing is challenged by multiple observations [171]. A new mechanism for the inter-band timelag has been proposed as per the thermal disk turbulence scenario [162]. As seen in the left panel of Figure 7, for AGNs akin to NGC 5548 observed in the five WFST passbands, the disk turbulence model predicts an intrinsic dispersion of the inter-band timelag as a function of wavelength in seeming consistency with current preliminary observations. Employing a tentative survey strategy described in §2.2, $\lesssim$ 10% - 30% accuracy of the measured timelag is readily achievable through averaging hundreds of AGNs with comparable BH mass and luminosity, even if the first year data are solely used (Figure 7, right panel). A significant accuracy of the timelag measurement is expected as a result of 6-year data accumulation.

The $\sim$ 700 square degree deep drilling fields frequently monitored by WFST are significantly larger than those in the PS1 Medium Deep Survey and those planned for LSST, and appealing progress in AGN research is expected to be made by WFST. In addition to assessing the time lags between different wavelengths, these deep drilling fields will offer a unique opportunity to investigate the true variable SEDs as well as the timescale-dependent color variation of AGNs, of which the latter is deemed as a new path to probe and test the accretion disk physics in the era of time-domain astronomy [172], demonstrating the potential of the WFST legacy survey to improve our understanding of AGN variability physics.

3.4.2 Particular AGN Variability

While the majority of AGNs display stochastic variations, the persistent monitoring of AGNs in the current time-domain era has led to the emergence of previously known types of AGN variability with enigmatic physical origins.

Extremely variable (EV) AGNs are those vary by $>$ 1 mag on a timescale of decades [173], in contrast to normal AGNs with a typical variation of $\sim$ 0.2 mag on a similar timescale. The physical origin of EV AGNs is under debate, but a universal mechanism underlying both extreme and normal variations has been suggested [174]. Intriguingly, $>$ 20% of EV AGNs are spectroscopically confirmed as rare changing-look (CL) AGNs [175]. CL AGNs are featured by dramatic emergence or disappearance of broad emission lines on timescale of decades, which pose challenges to the standard thin disk theory. Despite that most CL AGNs are intrinsically related to changes in the accretion rate [176], the cause of such a change is unknown as yet. Furthermore, the timescale and frequency of CL AGNs may place constraints on the episodic and net lifetimes of AGNs, and are instrumental to probing the AGN triggering mechanism and the accretion process. Complemented by archival data, the WFST surveys will facilitate the construction of decades-long light curves and the characterization of EV and CL AGNs.

From nearly a million quasars from the CRTS survey, Graham et al. [177] identified 51 events showing strange major flares atop of the normal stochastic quasar light curves. Their physical origin remains unclear, though micro-lensing by stars in the foreground galaxies is a possibility [178], and

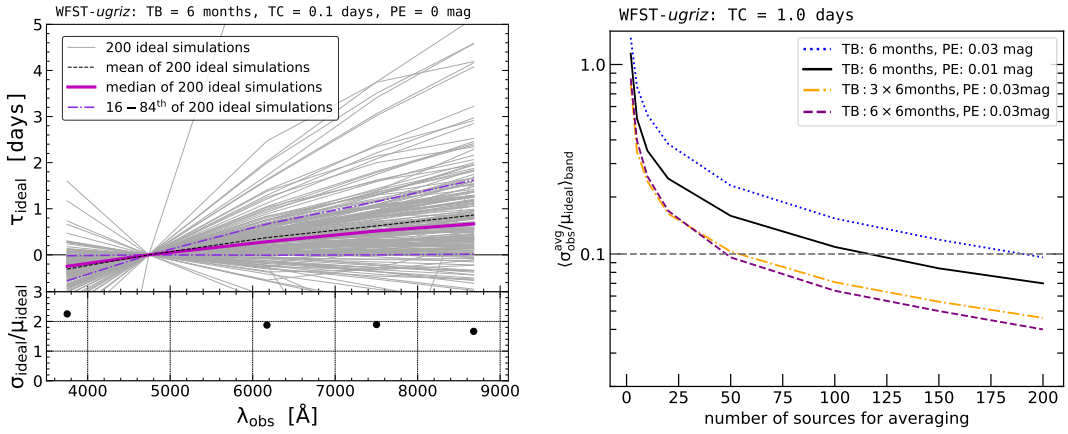

Figure 7 Left panel: relative to WFST-*g* band, the intrinsic inter-band timelag as a function of wavelength implied by the disk turbulence model [167] for AGNs akin to NGC 5548 observed yearly in WFST-*ugriz* passbands, assuming a temporal baseline of 6 months per year, a temporal cadence of 0.1 day, and without photometric error (Z. B. Su et al. 2023, in preparation). In the top subpanel, gray thin solid lines show results of individual simulations, while the median/mean and 16%-84% percentile ranges are shown accordingly. In the bottom subpanel, the intrinsic uncertainty of individual timelag in each band is quantified as the ratio of the corresponding dispersion $\sigma_{\rm ideal}$ to the mean timelag $\mu_{\rm ideal}$. Right panel: considering a real temporal cadence of 1 day in the WFST DHS and photometric errors of 0.01-0.03 mag, the observed uncertainties of the mean timelag decreases significantly with increasing the number of sources used in averaging and especially with increasing the cumulative observations from one year to three and six years.

a more appealing proposed mechanism is associated with explosive stellar-related activity in the accretion disk, such as SNe, TDEs, or mergers of stellar-mass BHs [177]. Remarkably, the ZTF survey has potentially spotted an event of binary BH merger in the accretion disk of an AGN in accordance with a reported gravitational-wave event [95]. Nearly two magnitudes deeper than ZTF campaigns, the WFST survey promises to significantly increase the number of detected extraordinary events as a basis for in-depth investigation of their nature.

Periodically varying quasars are considered to be supermassive BH binary (SMBHB) candidates, of which several have been reported [179]. Recently, from a sample of $\sim$ 9000 color-selected quasars in an $\sim$ 50 deg^2 sky area of the PS1 Medium Deep Survey, Liu et al. [180] identified 26 SMBHB candidates with more than 1.5 cycles of variation. The WFST surveys will help verify these SMBHB candidates and identify new candidates, if deep fields larger than those of PS1 are monitored.

Notably, the decades-long light curves delivered by the WFST survey will benefit the search for peculiar AGNs with monotonically increasing/decreasing variations, minimal variations over a long timescale and true turn-on/turn-off AGNs, potentially a crucial step towards revealing the triggering mechanism of AGNs.

3.4.3 Low-luminosity AGNs and IMBHs

Low-luminosity AGNs in dwarf galaxies is of particular interest, because they practically offer the opportunity to identify candidates of intermediate-mass black holes (IMBHs) that bridge the mass gap between SMBHs and stellar-mass BHs. IMBHs in the local universe, as relics/analogs of SMBH seeds in the early universe, are essential for investigating the seed formation mechanisms and the co-evolution of BHs and galaxies. However, IMBHs with supportive observational evidence remain scarce to date, rending the increase of the sample size a pressing demand (see [68] for a review).

A challenge in finding low-luminosity AGNs hosted by dwarf galaxies is posed by the weak AGN signal that is easily overwhelmed by the star-forming activity when conventional methods (e.g. optical spectroscopy, X-ray or radio mapping) are employed. Variability proves to be an effective tool for distinguishing real AGNs from star-forming galaxies and has resulted in the discovery of a considerable number of IMBH candidates in dwarf galaxies, including star-forming ones largely overlooked previously. Recently, the characteristic timescale of optical variability is found to correlate with the BH mass [181], paving a way to identify IMBH candidates through mass estimation purely based on photometric variability. The high-resolution images to be obtained by WFST will significantly alleviate the dilution of the stellar light from host galaxies, in contrast to current time-domain optical surveys. Reliable photometry of these weak AGNs will thus become accessible, allowing for detection of active IMBH candidates not only in isolated dwarf galaxies, but also in close dwarf companions of large galaxies, or even in the stripped cores of dwarf galaxies inside a massive galaxy. In combination with a daily-based cadence in high cadence fields, these photometric measurements promise to help construct an appreciable sample of IMBHs with BH mass estimates.

3.4.4 Off-nucleus AGNs

Observationally, off-nucleus AGNs are featured by the spatial offset and are physically connected to nearby companion galaxies. According to the standard framework of hierarchical structure formation, a galaxy merger as well as the subsequent coalescence of SMBH binaries in a gas-rich environment is naturally expected [182]. The coalescence may result in a recoiling SMBH, as predicted by multiple numerical general-relativity (GR) simulations [183]. Hence, off-nucleus AGNs are probably hosted by galaxies in an early phase of galaxy merger, or are ejected AGNs in case the recoiling SMBH is still active after merger. A systematic search for off-nucleus AGNs in galaxy mergers at different offsets and redshifts will help constrain the role of galaxy merger and the associated AGN fueling and feedback, while a search for recoiling SMBHs will provide insight into the distribution of mass ratios and spins in SMBH binaries prior to merger so that the GR numerical simulations are tested.

To date, the application of multiple approaches has only resulted in several hundred offset AGN candidates [184] and a few recoiling SMBH candidates [185]. Recently, adopting a novel variability-based search strategy, Ward et al. [185] identified 52 AGNs in merging galaxies and 9 recoiling SMBH candidates based on a parent sample of 5493 optically EV AGNs with flux variations over 2.5 mag in both ZTF $g-$ and $r-$bands over a 2.5-year period. Among their offset AGNs, those with available redshifts display linear separations typically larger than 2 kpc as a result of the low resolution of ZTF images. In comparison, the high-resolution multi-band imaging of WFST will enable us to construct a sample of targets with smaller offsets that helps reveal the crucial phase closer to the merger event, and a more statistically complete sample allowing to test relevant physics before and after mergers is also accessible. A new method to search for off-nucleus AGNs or close AGN pairs based on their color variation properties (e.g. the bluer-when-brighter trend) is under development. The nature of off-nucleus AGNs found by WFST will be further explored when the extremely high-resolution images from CSST become available.

3.4.5 Strongly-lensed AGNs

When AGNs are lensed by intervening objects (galaxies in particular), multiple images may be observed. Such strongly-lensed AGN systems are of fundamental importance to a number of astrophysical frontiers. They facilitate the measurement of the total-mass profile and dark-matter substructures in the lens galaxies, and are used to probe the co-evolution of black holes and their hosts at cosmological distances. When the light curves of lensed AGNs are obtained, these systems can be further used to constrain the stellar initial mass function in the lens galaxies and to measure the size and temperature profile of the accretion disks surrounding BHs in the background AGNs. In addition, strongly-lensed AGNs with time delay measurements may deliver independent and precise measurements of the Hubble constant, a probe of particular importance to deepen the understanding of the growing tension between the H_0 values given by distance ladders and cosmic microwave background observations.

The discovery of strongly-lensed AGN systems traditionally relies on imaging- and spectroscopy-based methods, though several variability-based methods have been developed recently [186, 187], which may render ongoing and upcoming time-domain surveys (e.g. ZTF, WFST, and LSST) fully exploited. To date, $\approx$ 200 strongly-lensed AGN systems have been found, of which light-curve measurements for individual lensed images are avaible to only $\approx$ 30 [3)]. A simulation conducted by Oguri et al. [55] suggests that, on average, there exist $\simeq$ 0.06 galaxy-scale strongly-lensed AGN systems per deg^2 possessing two (for two-image systems) or three (for four-image systems) lensed images brighter than i = 22 mag. Therefore, we expect WFST to detect $\approx$ 500 strongly-lensed AGN systems, and notably, to further deliver multi-band high-cadence light curves of these systems. The resultant extensive legacy dataset will potentially be a significant step forward in multiple relevant frontiers.

4 Asteroids and the Solar System

4.1 Overview of NEO Science

By definition, a near-Earth Object (NEO) is any object with its perihelion q≤1.3 AU and its aphelion Q≥0.983 AU. Possibilities include an asteroid or a comet. NEOs may deliver information about the primordial materials of the Solar System, though a more realistic reason to construct a catalog of them as complete as possible is their potentially damaging impacts onto the Earth. Ever since the early stage of its formation, Planet Earth has been subject to NEO impacts. An exhaustive geologic consensus has revealed that the Cretaceous-Tertiary extinction was caused by the impact of a large asteroid or comet 65 million years ago [188]. In July, 1994, the widely observed impacts into Jupiter of the fragments of Comet Shoemaker-Levy 9 released energy equivalent to millions of megatons of TNT and generated fireballs and dark clouds on Jupiter as large as the Earth. In view of the realistic threat of impacts, NEO surveys were commissioned in the late 1990s (e.g. LINEAR, NEAT, Spacewartch, CSS,

3) https://obswww.unige.ch/~millon/d3cs/COSMOGRAIL_public/code.php

Pan-STARRs [189, 190], ATLAS, CNEOST). Knowledge on the NEO population has been accumulating for three decades, and more than 95% of kilometer-class NEOs have been cataloged hitherto. The goal of the Large Synoptic Survey Telescope, NEOCam and other next-generation sky surveys is to catalog NEOs of relatively small sizes.

Sky surveys using ground-based optical telescopes are the most efficient and systematic approach to capture NEOs. In the next decade, LSST is poised to monitor NEOs on the southern hemisphere, while WFST on the northern hemisphere will contribute a comprehensive catalog of NEOs at an advantage of its wide FoV. WFST will manifest itself by its capability of detecting small and faint (r=22.5 mag with 30-second exposure time) objects, and its 6.5 deg^2 FoV that will enable frequently repeated mapping of a significant fraction of the sky to search for NEOs, and its high resolution (0.33″/pix) to optimize the orbital accuracy of faint NEOs. Granvik's model [191] predicts that thousands of near-Earth asteroids are readily observable by WFST every night (see: Figure 8).

Detection of NEOs on or within the Earth's orbit can be challenging for ground-based observers due to their proximity to the Sun, rendering these NEOs poorly characterized and cataloged as yet. The majority of the objects that fall into this class are known as Atiras or interior-Earth objects. In general, Atiras are only observable in the brief windows during evening and morning twilight. Multiple programs have surveyed Atiras, but only 28 are known to us as yet, of which many were discovered by ZTF [9, 192]. Monitoring the Atiras region may bring up additional benefits, because twilight observations at the near-Sun region (see: Figure 9) will significantly increase the solar phase angle coverage of NEOs and MBAs, so that photometric models and actual detection are both improved, facilitating the discovery of Earth Trojan asteroids [193] supposed to librate at the Earth-Sun L4 and L5 Lagrange points. Dynamical simulations predict that these objects can survive over a timescale comparable to the age of the solar system, implying that an ancient population of small asteroids may exist in these regions.

The combination of the 2-meter aperture of WFST and the excellent night sky conditions of Lenghu is advantageous to twilight observations (starting at a sun altitude of −12 degrees and ending at −18 degrees). A twilight survey is a strategy to realize the science goals described above without interfering the operation of WFST surveys. However, we must be aware that sky background brightness at twilight (According to [194], the average of lightening or darkening is 0.23 ± 0.02 mag/arcsec^2/min at twilight) will worsen the detection limit, only a few relatively large near-Earth asteroids may be seen. Another concern during the twilight NEA survey is due to the low-orbit satellite constellation like Starlink. [195] estimate that once the size of the Starlink constellation reaches 10,000, virtually all ZTF images taken during twilight will be of lower quality, WFST twilight NEA survey likewise.

4.2 Cometary Activity

Comets are considered to be the least modified solar system objects or "fossils" date back to the era of planet formation, and are therefore an essential probe to the origin and evolution of the solar system. They can be classified into short-period (with orbital periods shorter than 200 years) and long-period (orbital periods over 200 years) comets. Before 2006, comets were believe to originate from two locations: most short-period comets born in the Kuiper Belt or the scattered disc, while long-period ones in the Oort Cloud. The main asteroid belt was identified as the third origin of comets in 2006 [196]. Main-belt comets are found in the main asteroid belt with orbital characteristics are similar main-belt asteroids, though tails or comas exist. Main-belt comet has arisen broad interest ever since their discovery, because the existence of comets in the asteroid belt implies that water ice exists therein, a intriguing clue to tackling the origin of water on the earth [197] and to the solar system's thermal history. To date, only 9 main-belt comets have been discovered [198, 199], thus an in-depth understanding of these objects awaits systemic searches and accumulation of further investigations.

Within 3 AU, cometary activity is consistent with the standard model, in which water ice volatilization acts as the main drive [200]; while beyond 5 AU, the volatilization of volatile gases is the main cause [201]. Different modes are at work, in which dust is released from the surface of the comet nucleus as a result of the sublimation of gas ice and water ice, distant comets therefore promise to help unveil the mechanisms underlying cometary activity. WFST is expected to make contributions to the examination of the activity of main-belt and distant comets.

4.3 Trans-Neptunian Objects and Planet Nine

Trans-Neptunian Objects (TNOs), also known as Kuiper Belt Objects (KBOs), are asteroids or dwarf planets beyond the orbit of Neptune, of which the distribution extends from about 30 AU from the Sun to nearly 1,000 AU or even further. Over 2,000 of these objects have been cataloged so far, likely representing only a tiny fraction of the actual populations in this region. The Kuiper Belt is believe to be populated with millions of objects, of which hundreds of thousands are larger than 100 kilometers [202, 203].

The diverse structures and characteristics of TNOs provide clues to the formation and evolution history of our So-

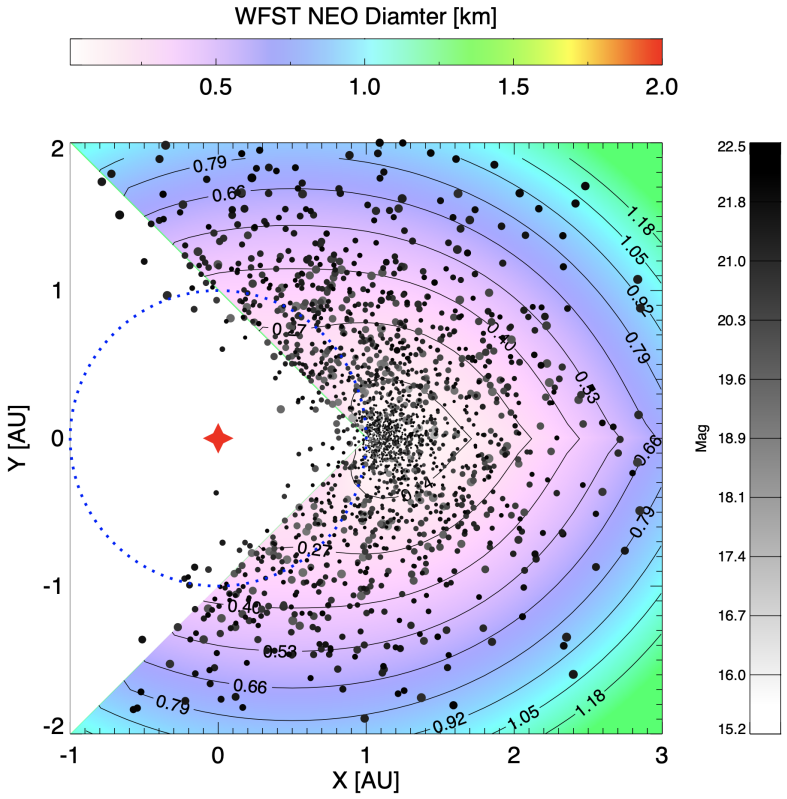

Figure 8 The size and position of near-Earth asteroids visible to WFST, the color indicates the diameter of NEA,each dot represents a NEA(form Granvik's model[191]),the dot's gray scale represents magnitude,the size of the dot indicates the diameter of NEAs. The dotted blue line shows the orbit of the Earth,the red asterisk at the origin represents the Sun.

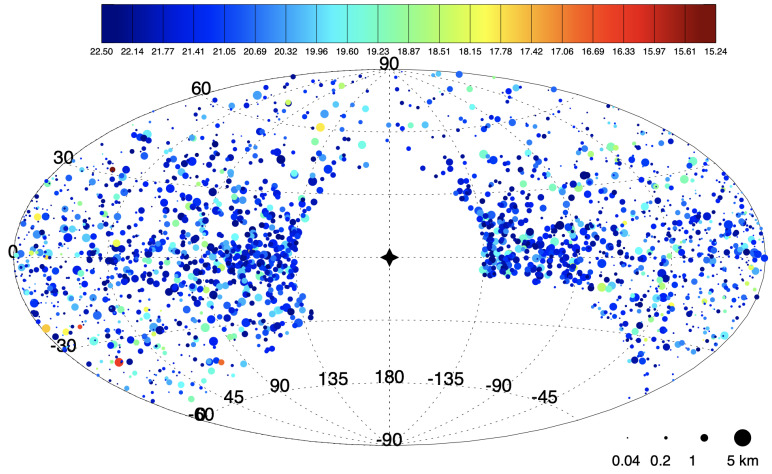

Figure 9 Ecliptic coordinate system centered on the sun, the dot's color represents magnitude,the size of the dot indicates the diameter of NEAs (form Granvik's model[191]), the star in the center represents the Sun. The 45° region around the Sun is considered unobservable.

lar System, and offer unique information to place constraint on unknown parameters involved in planetary formation and migration simulations. TNOs are classified into several dynamical populations: resonant populations, classical belts, scattering disks, and detached objects. Comparison between different populations may shed light on their respective evolution history. The cold classical subclass, dynamically defined as TNOs with non-resonant orbits, no close encounters with Neptune, and with orbital inclinations less than 5°, is a special population with multiple unusual physical properties (e.g. a distinctly red color, a large fraction of wide binaries, generally higher albedos, a steep slope of size distribution at large sizes) [204]. These unusual properties imply that this subclass may have formed or dynamically evolved in processes different from other TNOs. Furthermore, a variety of potential correlations among orbital and physical characteristics (e.g. inclination and color) awaits observational tests using a larger sample [205]. Notably, even the discovery of a single binary asteroid system or several high-inclination objects may impose strong constraints on planet formation and evolution theories [206].

The Planet 9 hypothesis derives from several dynamical anomalies of known distant TNOs [207]. Distant TNOs, also known as detached objects, are far beyond the eight-planet dynamical region, and may act as an indirect probe of the far reaches of the solar system. Hitherto, only 14 detached objects have been detected, of which five chaotic objects may fail to represent the dynamical statistics because of their instability [208], necessitating a sample with higher statistical significance to help clarify the (non)existence of Planet 9.

5 The Milky Way and Its Satellite Dwarf Galaxies

5.1 Star Formation

5.1.1 Young Stars

Mass accretion rate ($\dot{M}_{\rm acc}$) is a crucial parameter in modeling the evolution and dissipation of circumstellar disks and planet formation as well. Young stars commonly display accretion variability at various timescales due to different physical mechanisms, including non-steady accretion on timescales of hours, global instabilities of the magnetospheric structure on timescales of months [209, 210]. In addition, the interaction between circumstellar disks and the young massive planets may induce pulsed accretion [211]. Pulsed accretion onto young stars also serves as a novel tool to identify young massive planets. Measurement of accretion rates of young stellar systems helps unravel the evolution of circumstellar disks in low-metallicity environments.

Magnetic pressure may expel gas from the midplane of the disk, which is funneled onto the star along the magnetic field lines. The gas flow falls onto the stellar surface at approximately a free-fall velocity, causing a strong "accretion shock" on the stellar surface [212]. Ultraviolet/optical excess emission arises when the gravitational energy of the infalling material involved in the accretion process is radiated away along with the accretion shock, manifesting itself as a direct measure of the accretion rate [213]. The WFST survey will adopt an optimized methodology by employing *u*-band, in which the Balmer excess emission falls, and conduct $\dot{M}_{\rm acc}$ measurements. Figure 10 (left) depicts the relation between the WFST *u*-band brightness and the accretion luminosity for a sample of young stars in the literature, where the WFST synthetic observation is performed on their VLT/X-shooter spectra and the accretion luminosity are taken from [214]. The tightness of the correlation promises that WFST *u*-band photometry will yield accurate measurement of accretion rates onto young stars. Using the data from the Gaia EDR3 and ALLWISE, we construct a sample of over $\sim 1.8\times10^4$ young stars surrounded by circumstellar disks observable by WFST (Figure 10; right). Hence, for the first time, WFST will accomplish a systemic measurement of accretion rates and variability based on a large sample of young stars.

5.1.2 Accretion Burst Events

To date, it remains an open question that how young stars gain their mass from the surrounding environment through disk accretion. Relevant models conventionally assume a steady accretion onto the central young star with a constant accretion rate [215], though these models predict a significantly higher luminosity than what is observed [216]. To tackle this "luminosity problem", Kenyon & Hartmann [217] proposed an episodic accretion scenario, under the assumption that a large fraction of disk accretion occurs during a number of short-lived bursts. Accretion bursts were first observed around low-mass young stars [218], and seen around high-mass young stars later [219], but it remains unclear how frequently young stars are in the state of accretion outbursts, and what mechanisms drive these outbursts.

EXors and FUors are the two types of young stars where accretion outbursts is likely ongoing. The Fuors phenomenon is the most prominent during star formation that displays an increase of brightness by 5 magnitudes or more within a year and remains bright afterwards for decades [218], while EXor outbursts occur on shorter timescales (~ years) and show lower amplitudes [220]. It remains enigmatic whether any physical distinction exists between these two types because of the paucity of known FUors and of observations before their

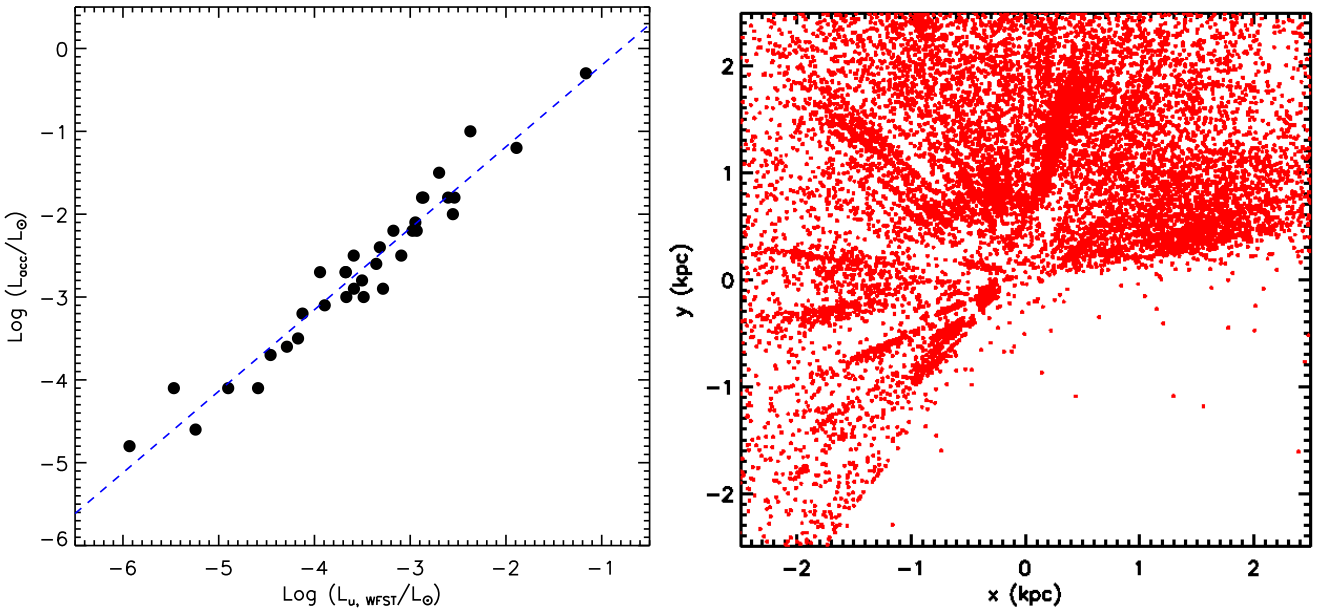

Figure 10 Left: Relation between the WFST u-band brightness and the accretion luminosity. Right: A bird's-eye view of the distribution of young stars with circumstellar disks which can be observed with WFST, looking down on the Galactic disk with the sun at the center.

outbursts. Among the ~1.8×10^4 young stars with circumstellar disks to be monitored by WFST, we expect to detect 0.5–7 FUor outburst events each year, an estimate based on the PTF survey [221]. Despite that all-sky infrared surveys are awaited to fully characterize the evolutionary stages of these young stars, the WFST time-domain survey will significantly contribute in exploring the accretion history of young stars that are captured at different evolutionary stages.

5.2 Mapping the Milky way

5.2.1 3D Dust Distribution

Dust distribution is an indispensable piece of information of Galactic science, while dust extinction is routinely invoked in astrophysical studies. A thorough dust distribution map is recovered by measuring the reddening and extinction towards a large number of stellar objects. Based on modern wide-field optical photometric and spectroscopic surveys (e.g. SDSS, Pan-STARRS1 and Gaia), the three-dimensional (3D) Galactic dust distribution has been mapped at an arcmin-scale spatial resolution, from which the structures of dust Galactic disk such as warp and spiral arms have been revealed [222, 223]. The WFST survey is at least 2–3 magnitudes deeper than Pan-STARRS1 in *r* band, promising to produce 3D dust maps with improved resolution and dynamical range than previous maps, so that Galactic high-density regions associated with star formation can be traced and Galactic models be better constrained. In particular, the high sensitivity and photometric accuracy of the WFST survey will allow for investigating the diffuse interstellar medium at high Galactic latitude. For instance, WFST will benefit the study of intermediate-velocity clouds (IVCs) that are considered as an inflow of gas consisting of recycled disk material and thus believed to be connected to a Galactic fountain process [224].

5.2.2 Stellar Clusters

Stellar clusters in the Milky Way serve as ideal test beds for stellar evolution from pre-main sequence to post-main sequence stages, given their ranges of age spreading over several magnitudes from a few to tens of Myr (open clusters) to a few to tens of Gyr (globular clusters) [225, 226]. The co-eval, co-spatial, and iso-metallic stellar members provide abundant clues to stellar astrophysics. As important as they are, the majority of star clusters have been relatively poorly studied due to their large distances or large angular sizes.

The detection limit of the final stacked images from the WFST survey programs in the *r* band will reach 25 mag, 2–3 magnitude deeper than the Pan-STARRS1 survey. For open clusters confined in the galactic plane, we estimate the minimum stellar mass detectable by WFST as a function of distance (Figure 12). For the clusters within a 5 kpc distance from the sun, WFST can resolve them down to a stellar mass of $\lesssim 1\,M_\odot$ with an appreciable completeness of mass estimate for these open clusters. The young open clusters and the even younger embedded clusters (to be better studied in IR) represent the current star formation rate of the Milky Way [227]. Thus, the 3D distribution of these two types of young

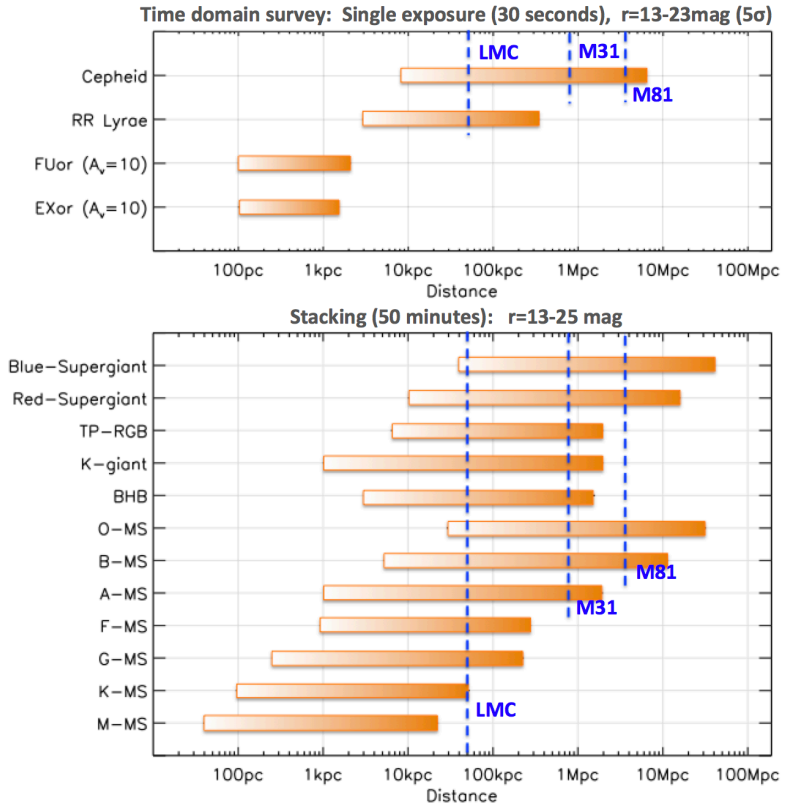

Figure 11 Detectability of different types of stars vs. the distances in the WFST images with single exposure (top) and stacked images (bottom)

clusters depicts the 3D star formation rate distribution of the Milky Way, which, along with the 3D molecular gas map [228], provides a view of baryon cycle of the Milky Way. For nearby ($\lesssim$1 kpc) young clusters, WFST's accuracy, sensitivity, and multi-epoch mapping will enable the detection of cluster members down to the mass level of brown dwarfs, rendering a significantly improved characterization of low-mass star formation in stellar clusters, which is of fundamental importance to deriving initial mass functions.

The Gaia mission has released a catalog of reliable members for over 200 known clusters within 2 kpc from the Sun [229]. These clusters range from 10 Myr to several Gyr in age [230] and are therefore ideal calibrators for the mass–dependent relationship between stellar rotation and age. The ages of these clusters are derivable from color-magnitude fitting using the Gaia data [230], while the rotation periods of the individual members in a cluster are achievable from the WFST time domain surveys. A well-calibrated mass–dependent relationship between stellar rotation and age is a crucial step towards understanding the star formation history of the milky way.

5.2.3 *Structure of the Milky Way*

The stellar structure of the Milky Way (MW) consists of four components: a bulge, a thin disk, a thick disk, and a diffuse stellar halo. The knowledge of the structure of the Milky Way has been rapidly increasing due to a variety of sky surveys (e.g. SDSS, Pan-STARRS, LAMOST, and Gaia) and the development of technology supporting these surveys. However, plentiful issues about the detailed structures of the MW and their formation mechanism remain unresolved.

As a space-borne facility, the Gaia satellite is capable of mapping the entire sky, though its detection limit of $\sim$ 20 mag is insufficient for scrutinizing dense stellar fields. An investigation of the detailed MW structures and their formation mechanism necessitates a deep survey that covers a large FoV and detects a larger number of low-mass stars to large distances (c.f. Figure 11; bottom). An accurately determined 3D distribution of MW stars and a decomposition of the MW into a number of components are crucial steps towards constraining the formation mechanism of the different MW components. The decomposition hinges on measurement of the metallicity of individual stars, which requires high-sensitivity and high-precision photometry in *u, g, r bands* [231]. Previous and current surveys with sufficient FoVs either lack a *u*-band filter (e.g. Pan-STARRS) or lack sensitivity in *u*-band

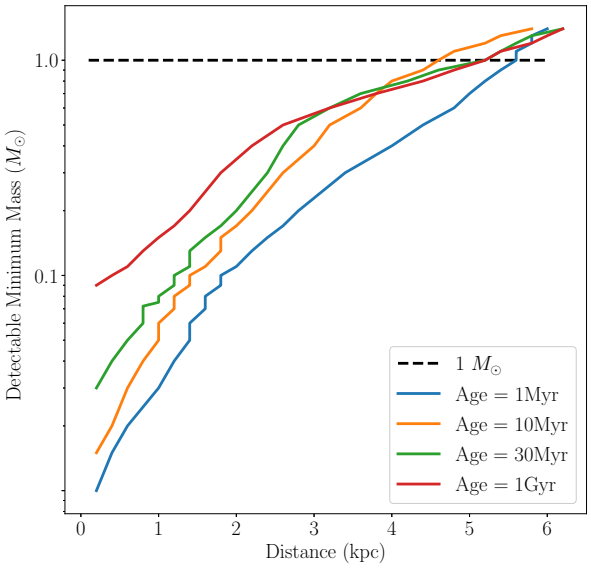

Figure 12 The minimum stellar mass of the open cluster member varies with distance from near to far. The isochrones of low-mass stars at 4 ages are shown in different colors [232]. For open clusters, an empirical relation $A_V = 1.5\,\mathrm{mag\,kpc^{-1}}$ is used in the distance module.

(e.g. SDSS or SkyMapper). The upcoming LSST will reach a depth of $r = 27$ mag when the images are co-added, though the observations will be limited to be within the southern sky.

The six-year WFST co-added images will reach limiting magnitudes of $u = 24.6$, $g = 25.2$, and $r = 25.1$, which is ~ 2 magnitude deeper than the existing SDSS data. WFST is expected to obtain high-precision multi-color measurement of nearly 5 billion MW stars and detect main sequence stars at large distances (Figure 11). The multi-band photometry (including u band) of the WFST sky survey will enable measurement of the photometric metalicities of stars, a critical tool to distinguish halo stars from disk stars, and to accurately determine photometric distances of stars. Large metal-poor star samples will yield a metallicity distribution function (MDF) of the Galactic halo and thus constrain the chemical evolution models of the MW. With the metalicities and distances of stars in hand, we will probe the MW structure with better precision and over a broader range of distance. In particular, WFST is expected to detect several tens more debris streams at large distances ($R > 50$ kpc) in either dwarf galaxies or globular clusters.

5.2.4 Astrometry and Variable Stars

WFST can survey over 6000 square degrees per night and map the entire northern sky in each band every three nights. The six-year survey will accumulate high-quality imaging data of the northern sky in *u, g, r, i, z* bands at over one hundred epochs. These multi-epoch data will facilitate measurement of the proper motions (σseveral mas yr^{-1}) of one billion stars in the northern sky and delivery of the multi-dimensional information (e.g. proper motion, parallax, position and metalicity) of ~100,000 nearby stars, so that the local gravitational potential field are constructed and the mass distribution and structure model of MW are constrained. WFST's sensitivity and accuracy is sufficient for detecting hypervelocity stars in the galactic halo at distances up to more than 10 kpc. The multi-band photometry will help determine the metalicities of these hypervelocity stars, a fundamental parameter to discriminate their origination [233].

The WFST time-domain survey will catalog millions of variables. Among them, RR Lyrae Stars and Classical Cepheids are two of the most important types that serve as standard candles to measure distances; eclipsing binary stars (EBs) are of significance to stellar physics; and X-ray binary systems, including high and low mass binaries, are ideal astrophysical laboratories to examine the formation and evolution of stars, compact objects, and mass transfer processes in a binary system [234]

RR Lyrae Stars are old (>10 Gyr), low-metallicity, horizontal-branch pulsating stars varying periodically, and have been used as standard candles. Currently, the completeness of RR Lyrae Star detection in existing surveys like Gaia and PanSTARRS drop to $\lesssim$50% at a distance $\gtrsim$ 80 kpc [235]. The WFST survey 1–2 magnitude deeper than Pan-

STARRS1 will significantly increase the sample size of RR Lyrae Stars at large distance in MW and in nearby dwarf spheroidal galaxies (Figure 11; top). RR Lyrae Stars at large distances are of exceeding importance to probing the Galactic halo and the MW structure near the viral radius of the MW's dark matter halo (∼200–300 kpc [236]). As for the Galactic thick disk, ambiguity remains whether it is a distinct component, whether it is flared or warped, and how it is related to other Galactic components (thin disk, halo, and bulge) in spatial extent, chemistry and kinematics [237]. The deep WFST time-domain survey to search for RR Lyrae at low Galactic latitudes, where extinction is higher than in the halo, will shed light on these puzzles.

Classical Cepheids are among the pivotal standard candles to determine accurate distances within the local group. In contrast to RR Lyrae Stars, Classical Cepheids are young stars (≲400 Myr). They are involved in the examination of the thin disk structure of the MW and deemed to trace the detailed morphology of the thin disk out to a Galactocentric distance of ∼15 kpc [238]. The WFST survey promises to detect Classical Cepheids at distances over 5 Mpc (Figure 11; top). Construction of a WFST sample of MW Classical Cepheids will allow for depicting the Galactic structure in more detail, while the sample of Classical Cepheids in other galaxies will help tackle the intrinsic variance of Cepheid properties.

Eclipsing binary stars (EBs) are indispensable for stellar physics. The accurate parameter (e.g. mass, radius, temperature, luminosity) of the two component stars are achievable through the analysis of EBs. These parameters will impose strict constraints on stellar evolution models, especially at the low mass end where the model is significantly uncertain. There remain many open issues in eclipsing contact binaries (ECBs), such as the merging of binary stars, the evolution of their common envelope, and the short-period limit [239]. The detection limit of the WFST survey in the *r*-band down to ≈23 mag in a 30-second exposure implies the discovery of faint EBs by WFST. According to the well-established period-color relationship of ECBs [240, 241], those ECBs with the shortest period possess the lowest temperature. Finding faint main sequence ECBs will help unveil the origin of the cut-off in the period of ECBs. In particular, an ECB system with M2V+M2V components is observable within a distance of 4 kpc with a brightness of r≈22 mag.

X-ray Binaries consist of a normal star and a compact object, being either a NS or a BH [242]. As per the mass of the optical companion, they are conventionally classified into high-mass (usually $\geq 10\ M_{\odot}$, [243]) and low-mass X-ray binaries (usually $\leq 1\ M_{\odot}$, [244]). The two main subclasses of high-mass X-ray binaries are the supergiant X-ray binaries and the Be/X-ray binaries. To date, only 114 high-mass X-ray binaries in the MW have been catalogued, of which about 60% are Be/X-ray binaries [243]. In a Be/X-ray binary, the compact companion is usually an NS [245], though Be-BH binary systems also exist [246]. Most Be/X-ray binaries are hard X-ray transients usually showing two types of X-ray outbursts: Type I X-ray outbursts, of which the X-ray luminosity $L_X \sim 10^{36-37}$ erg s^{-1} and the duration is the orbital period, and Type II X-ray outbursts, which are significantly brighter ($L_X > 10^{37} ergs^{-1}$) and display no evident connection with the orbital period [247]. Long-term optical observations indicate that significant optical variations precede the X-ray outbursts [248], necessitating the monitoring of a sample of Be/X-ray binaries to delineate the relationship between the optical variability and the X-ray outbursts. Low-mass X-ray binaries are systems where an NS or BH is accreting materials from its low-mass companion donor star via a Roche lobe overflow. About 200 low-mass X-ray binaries have been catalogued in our Galaxy [244], of which most are X-ray transients with observed outbursts. Population synthesis indicates that about 2.1×10^3 low-mass X-ray binaries with NS accretors exist in the MW [249], though the majority of them remain unexplored. The time-domain survey of WFST is expected to capture the periodic variability of the light curves and discover an remarkable amount of new candidates of low-mass X-ray binaries.

5.3 Satellite Dwarf Galaxies in the Local Group

The dwarf galaxies surrounding the MW and M31 are the galaxies of the lowest mass observable in the Universe. These objects are of broad interest due to their astrophysical uniqueness. Bright stars in these systems can be resolved even by ground-based telescopes, rendering them ideal targets to probe the star formation history, the chemical enrichment as well as the initial mass function in low-mass halos [250,251]. In addition, their abundance and spatial distribution place stringent constraints on structure formation theories on spatial scales smaller than ∼ 1 Mpc [252]. Like their massive peers, dwarf galaxies are dominated by dark matter, which is possibly detectable through the products of its decay. In view of their physical scales and distances, dwarf galaxies in the Local Volume are ideal laboratories for detection of dark matter decay signals [253].

The search for faint dwarf galaxies in the Local Volume has been continued ever since the serendipitous discovery of the first such system in 1930s. Only 11 MW satellite galaxies were known prior to SDSS. During the past two decades, more than 50 new MW satellites were discovered, thanks to the advent of large imaging surveys (e.g. SDSS). The majority of the known MW satellites have luminosities comparable to those of globular clusters, though their surface brightness is remarkably lower, posing a challenge to direct identifica-

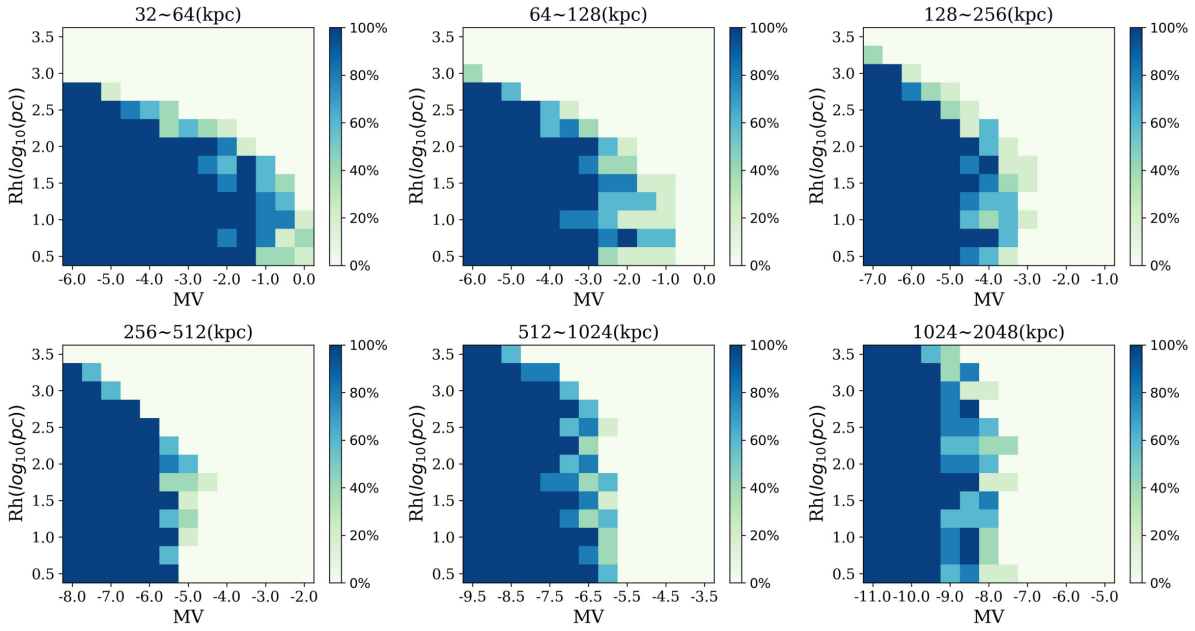

Figure 13 Detection efficiency of searches for dwarf galaxies. Detection efficiency is shown as a function of azimuthally averaged physical half-light radius and absolute V-band magnitude in different bins of heliocentric distance. The detection efficiency ranges from 0% to 100%, as shown in the color bar.

tion in imaging. In practice, these galaxies are immersed in statistical fluctuation of number density as significant as that of cataloged stellar objects.

The 6-year WFST co-added images will reach a depth of $r = 25.1$ and cover ~ 10000 deg^2 of the northern sky, well suited for the search of faint dwarf galaxies in the Local Volume. This depth is ~ 2 magnitude deeper than SDSS and comparable to that of the Dark Energy Survey (DES) [4]. DES covers ~ 5000 deg^2 of the southern sky, and ~ 20 Milky Way satellites are found in the DES footprints. Under the simple assumption that the distribution of MW satellites is isotropic, detection of ~160 MW satellites in the full sky down to $r \sim 25$ is expected. As for the SDSS footprints in the northern sky, ~ 40 satellites are expected down to the same magnitude limit. Taking into account the classical and newly found satellite galaxies in the SDSS footprints, we expect ~ 20 new MW satellites to be discovered in the era of WFST. However, this number is to be treated as an upper limit, because MW satellite galaxies are not observed to distribute randomly, but a trend to cluster near the Large Magellanic Cloud exists.

We conduct a simulation to analyze the capability of WFST in detecting dwarf galaxies. The detection efficiency is quantified by simulating model dwarf galaxies immersed in typical star fields as imaged by WFST. Background MW star fields are constructed with the code *Galaxia* [254]. A Kroupa initial mass function [255] is adopted for the simulated galaxies. In accordance to observations, we assume an old, metal-poor dominant stellar population that spans a stellar age range of 7–12 Gyr and a metallicity range of [Fe/H] = [−2.2, −1.5]. We then search dwarf galaxies using an algorithm in the literature [256]. We demonstrate the detection efficiency as a function of distance and $V-$band absolute magnitude of the galaxies in Figure 13. Within the viral radius of the MW ($\sim$ 300 kpc), we conclude that galaxies with $M_V < -4$ are readily detectable in the stacked images of WFST. Alternatively, the detection limit within 1 Mpc is found to be $M_V < -6$.

6 Galaxy Formation and Cosmology

Modern optical imaging surveys have significantly deepened our understanding of the universe. Especially in recent years, with the help of high quality imaging of SDSS, CFHTLenS, Dark Energy Survey (DES), HSC-SSP and KiDS, we are in a position to explore the universe with unprecedented accuracy, an era known as that of precision cosmology. Nonetheless, tension emerges between CMB observations and optical survey measurements, including the σ_8 tension between weak lensing and CMB as well as the H_0 tension between CMB constraints and time-delay/SNe Ia. It has been under suspicion whether this is due to certain hidden systematic effects or new physics beyond our knowledge. The debate arises even among research groups pursuing the same subjects but using data sets from different facilities. Meanwhile, extensive efforts have been made to improve the data processing pipelines to understand potential systematic effects. For instance, a recent shape catalog from HSC-SSP [257] is aided by detailed

simulations and systematic tests to ensure that systematic effects are under control.

Apparently, the entire collection of data sets obtained so far remains insufficient for an ultimate understanding of either new physics or systematic effects. In the near future, further progress will be made by space-based e.g. CSST, Roman Telescope and ground-based e.g. Vera Robin Telescope facilities which are expected to scan half of the entire sky and accomplish deep imaging down to 28 mag in *r*-band. Once completed, the WFST multi-band imaging survey will be the largest survey on the northern hemisphere overlapping with multiple spectroscopic surveys (e.g. PFS, DESI, LAMOST2 and MUST). The combination of WFST and LSST (on the southern hemisphere) will yield all-sky data, and the integration of multi-band imaging and spectroscopy promises to boost the advancement of precision cosmology.

6.1 Galaxy Formation

The WFST shear catalog will be a key product for galaxy formation studies delivering information about the position, shape, photometric redshift of galaxies as well as calibrated biases as a function of resolution and signal-to-noise ratio. Combined with preexisting and upcoming spectroscopic data available for the northern sky (e.g. SDSS, MUST and LAMOST2), it will significantly improve the accuracy of weak gravitational lensing measurements, placing more stringent constraints on theories of galaxy formation and cosmology. We elaborate science related to weak lensing analysis in three aspects, i.e. galaxy-halo connection, halo assembly effects and cluster detection. Two more important topics will also benefit from the WFST imaging surveys: the deep *u*-band imaging will potentially facilitate the construction of large samples of *u*-band drop-out galaxies and low surface brightness galaxies.

6.1.1 Galaxy-halo Connection

Galaxies form and evolve inside dark matter halos and are affected by the large-scale environment. Exploring the connection of galaxies with their host dark matter halos and with their large-scale environment is therefore a crucial step towards the accomplishment of the blueprint of galaxy formation. Numerous works exist in the literature on the galaxy-halo connection based on a variety of observational measurements such as galaxy clustering and galaxy-galaxy lensing [258, 259] or the combination of the two [260].

Nevertheless, plentiful questions remain unresolved. For instance, does the host halo mass depend on the galaxy properties? If this is the case, which galaxy properties are dominant? How are these relationships built? How do different environmental processes, an interplay of various environmental factors, affect the galaxy properties? A recent work [261] used a massive star-forming galaxy sample to find that about 67% of gas has been converted to stars, which is abnormally high compared the typical conversion fraction of 20-30%. It remains unclear what mechanism causes this specific mass bin that bears such a high gas consumption rate.

The host halos of AGNs featured by their strong central SMBH activity is another topic of interest. AGNs are different from other galaxies in the spectral energy distribution (SED) and spectral line features. Whether different types of AGNs reside in different large-scale environments remains an open question. Zhang et al. [260] conclude that the halo masses of AGNs are similar to those of star-forming galaxies, but are lower than the quenched control sample. However, AGNs appear to be surrounded by a larger number of satellites than star-forming galaxies, indicating an association of the AGN trigger mechanism with satellite galaxies.

The WFST shape catalog will manifest itself by the 7 (WFS) or 20 (DHS) times deeper imaging and multi-band photometry than SDSS, and the signal-to-noise ratio of Weak lensing analysis around galaxies will increase by a factor of 3, leading to an accuracy in halo mass estimation enhanced by a factor of ~ 2. Fig. 14 depicts the improved uncertainty in WFST measurement (red dots) compared to SDSS galaxy-galaxy lensing measurement (green dots). Within the halo virial radius, the WFST shape catalog alone is predicted to shrink the errorbar by a factor of 2.5.

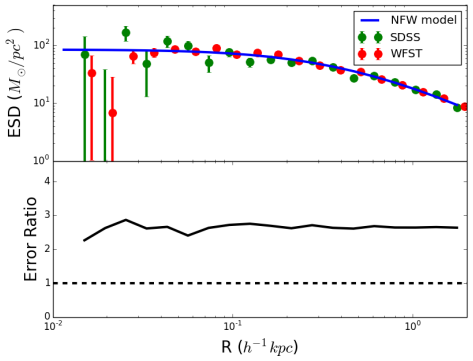

Figure 14 The comparison of the galaxy-galaxy lensing signals between SDSS shape catalog and WFST shape catalog. The lower panel is the ration between the two errors. The error shrinks by a factor of 2.5 given the same lens sample but different catalog.

6.1.2 Halo assembly effects

The clustering of dark matter halos strongly depends on the halo mass, though numerical simulations have revealed de-

pendence on other halo properties, including the formation history, the internal substructure and the spin of a halo, a higher-order effect referred to as the halo assembly bias.

Many observational efforts have been made to detect the assembly bias. For instance, Miyatake et al. [262] claimed the detection of assembly bias based on RedMaPPer clusters by performing weak gravitational lensing and projected clustering analysis. However, this result is recognized by Zu et al [263] as an artifact due to projection effects of the RedMaPPer cluster members, and therefore the secondary bias is even higher than the Lambda cold dark matter (LCDM) prediction. They further predict that a 10-fold larger number of clusters with deep imaging will concretely improve the detection. WFST will increase this number up to about 40,200, or 4.6 times larger than the sample size of Miyatake et al. (2016), spanning the same richness range but a broader redshift range ($0.1 < z < 0.8$). Combining WFST cluster sample with that of LSST is expected to suppress the uncertainty to less than 10%, at a level comparable to the predicted LCDM assembly bias. A recent work divided 630 massive clusters into early- and late-formed clusters using the ELUCID simulation [264], and concluded that a 4-σ difference in clustering is detected, suggestive of an real detection of assembly bias.

Clusters are not the only probe to the assembly bias. Lin et al. [265] constructed low-mass samples divided into early- and late-formed galaxies to pursue this effect, who attributed null detection to their noisy measurements. McCarhty et al. [266] extended the previous work by analyzing a larger number of galaxies and changing the clustering estimator to the redshift space distortion (RSD), which is essentially the Legendre expansion of clustering, but velocity information is taken into account. A large amplitude of velocity bias for early-forming central galaxies is found in this work, which may originate from assembly bias, though the measurement is again overly noisy to validate their statement. A significant detection awaits accumulation of more lens samples and deeper imaging data sets.

In addition, the accurate determination of halo boundaries is an important issue in galaxy formation, which are commonly defined as the radius that encloses a certain value of density contrast Δ compared to the mean/critical density of the universe. On a more physical basis, More et al. [267] introduced the concept of *splashback* radius, where the accreted matter reaches its first orbital apocenter. They claim that such a radius depends on the accretion rate of the halo, whose typical value ranges from 0.8 to 1.5 virial radii. A recent work [268] showed that the *splashback* radius also depends on the major/minor axis of the local tidal tensor. We expect that the first attempt to observationally determine the *splashback* radius will hinge on measurement of the surface number density of galaxies to be followed by detecting galaxy over density around SZ clusters as well as weak gravitational lensing.

WFST data from the WFS and DHS fields will yield high quality imaging and photometry to help address all the above research topics. In particular, the shape catalog will allow us to measure the halo mass of spectroscopically selected galaxy groups, to compare the result with that of other halo mass estimation methods, and to remarkably improve the measurement of *splashback* radius as well as the assembly bias.

6.1.3 *U-band Drop-out Galaxies at $z \sim 2$–3*

Lyman Break Galaxies (LBGs) are star-burst galaxies at high redshift (for a review, see [269]) that can be identified using the technique of combining u, g and r bands, as demonstrated in a recent work of joint analysis based on the CLAUDS and HSC-SSP deep imaging [270, 271]. Plentiful works exist in the literature address the UV luminosity function (UV-LF) of LBGs that can be used to estimate the energy budget at high redshift. Since the pioneering work of Steidel et al. [272], continuous efforts have been made to analyze the UV-LF of LBGs (e.g. [273], [274]).

The selection criteria are $u - g > 0.88$, $g - r < 1.2$ and $u - g > 1.88(g - r) + 0.68$ (Equation 4 in [270]). WFST will provide all the involved broad-band imaging with deep and wide survey regions, as mentioned in Sec. 2. We estimate the number of LBGs from both the DHS fields (~1000 square degrees, down to 26.4 mag or an absolute mag of −20.6 at $z = 3$ in g, and 25.9 mag in r) and WFS fields (6800 square degrees, down to 25.1 mag or an absolute mag of −21.9 at $z = 3$ in g, and 24.7 mag in r).

We adopt the luminosity function at $z = 3$ in [274], for which M_{1350} monochromatic flux is used as an indicator. In the DHS region only, we expect to detect 10^7 galaxies (with g-band absolute magnitude down to -20.6, considering the %90 completeness for $r < 25.5$). Though in an amount two orders of magnitude lower than that of the LSST survey, this catalog of galaxies will serve as a guidance for future follow-up spectroscopic surveys. LBGs at higher redshift ($z > 4$) can also be selected as per *g, r, i* color criteria as already done in [275], yielding another valuable legacy catalog.

6.1.4 *Low Surface Brightness Science*

The low surface brightness (LSB) regime holds the promise to revolutionize our understanding of galaxy formation and evolution in the upcoming decade. In particular, demographics of satellites around galaxies of different morphological types and masses in the local universe will offer crucial tests of the LCDM paradigm on small scales; systematic characterization of stellar halos and tidal features in the outskirts of

galaxies can provide important clues to the hierarchical assembly histories of galaxies.

The prime focus architecture of WFST minimizes the contamination from scattered light, which is particularly desirable for LSB science. The WFST six-year co-added imaging data (~ 50 min) will reach a r-band 3–σ surface brightness limit of ~ 28.7 mag arcsec^{-2} by averaging a 10×10 arcsec^2 area, slightly deeper than the 275 deg^2 Stripe 82 field of SDSS. By scaling the results from extensive completeness simulations, we expect to achieve a detection of ordinary satellite dwarf galaxies down to an average surface brightness of ~ 25.7 mag arcsec^{-2} within the effective radius at a 50% completeness limit. This corresponds to a stellar mass limit of ~ $10^{6.1\pm0.5}$ $M_\odot$ out to ~ 60 Mpc [276]. In addition, a surface brightness limit of 28.7 mag arcsec^{-2} allows for detection of tidal features from galaxy merger events that happened at least ~ 3-4 Gyr ago. Finally, the wide-field and homogeneous data sets from WFST will enable a robust stacking analysis of surface brightness profiles well beyond 30 mag arcsec^{-2} for galaxies of different morphological types, masses and environments, providing stringent constraints on the build-up of galaxy stellar halos in general.

Besides the combination of its sky area coverage and survey depth, an important advantage of WFST over existing optical imaging surveys, such as DES and HSC-SSP (Hyper Suprime-Cam Subaru Strategic Program), lies in its inclusion of deep u-band data that are indispensable in probing stellar population properties of galaxies with broad-band photometry.

6.2 Cosmology

As tensions in cosmological parameter measurements recently emerge (e.g. H_0 and $S_8 = \sigma_8(\Omega_m/0.3)^{0.5}$) between the CMB probe and SNe Ia, time-delay, weak lensing analysis, debates arise on whether certain hidden systematic effects are at work or new physics is in anticipation.

In the northern sky, WFST is expected to make valuable contributions to cosmological research by detecting a large amount of SNe Ia (cf. Sec. 3.1.5) and strong lensing AGN/SNe Ia (cf. Sec. 3.1.5 and 3.4) systems, and yielding a cluster catalog and a shape catalog. In this section, we focus on the standard cosmology constraints and cosmologies that deviates from LCDM.

Within the framework of the standard cosmology, we proceed with the analysis of cluster mass function, cosmic shear and their combination with other measurements (e.g. clustering, cluster mass functions, time-delay, etc.). For non-standard cosmology, we focus on the constraints on modified gravity models, dark matter particle models, among other topics.

6.2.1 *Cluster detection and cosmology*

Clusters of galaxies act as a probe to cosmology and galaxy formation. The well-known Bullet cluster alone is a smoking-gun evidence of dark matter, where the spatial distribution of X-ray-emitting hot gas significantly deviates from that of dark matter inferred from weak lensing.

Furthermore, the shock feature seen in the X-ray poses a challenge to the standard cosmology in the sense that the exceedingly high collision speed of the two merging giants is difficult to realize in numerical simulations. Abell 520, another cluster intensively studied using weak-lensing techniques, poses another challenge to the classic galaxy formation paradigm in the sense that significantly fewer galaxies than theoretical prediction are found in the "dark core" of the cluster. Another puzzle results from the recent finding of a massive rotating cluster (the Coma cluster) rotating at a velocity of 197 km s^{-1}. In brief, an appreciable number of mysteries about clusters await exploration in the future WFST survey region.

Construction of reliable cluster catalogs is a nontrivial commission, especially when spectroscopic information of galaxies is absent. However, endeavors to catalog clusters using photometric information has been made (e.g. RedMaPPer and CAMIRA involving red ridge galaxies). Yang et al. [277] present a novel halo-based cluster selection method (a modified approach based on [278]), where adjustment of applied on the pipeline that delivers photometric data. Nevertheless, these methods suffer from the projection effect because of the accuracy of photometric redshift and therefore the membership estimation is biased, as described in [263] and [279]. Along with extended X-ray sources, the Sunyaev-Zel'dovich (SZ) effect is another tool of cluster studies. More recently, shear maps of galaxies are used to catalog the HSC-SSP shear map clusters.

The combination of cluster catalogs with a variety of selection methods and galaxy-galaxy lensing can yield tight constraints on observable halo mass scaling relations. Fig. 15 shows the κ (colored map) and shear map (white ticks) of a cluster selected from the ILLUSTRIS TNG simulation.

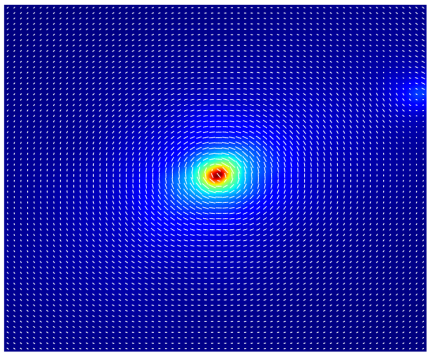

Figure 15 The shear map and kappa map of a cluster-sized dark matter halo chosen from ILLUSTRIS simulation with halo mass of $10^{14}\mathrm{h}^{-1}M_{\odot}$.

As mentioned in the previous section on assembly bias detection, WFST will generate a photometrically selected cluster sample based on the RedMaPPer algorithm. The sample will contain over 40,000 clusters with richness higher than 20 between $0.1 < z < 0.8$. The scientific goals include performing cluster mass estimation to constrain cosmology and cross-matching clusters with other observations (e.g. SZ clusters, X-ray clusters and weak lensing mass maps). The cluster catalog together with the weak lensing shape catalog will be of appreciable value for cosmological explorations and serve as reference data for next-generation surveys.

Once cluster catalogs from various observations are obtained, the cluster abundance and its evolution will readily constrain the fluctuation amplitude σ_8 and the Ω_m parameter. The baryon fraction of clusters can be used to estimate the ratio of cosmic baryonic fraction $\frac{\Omega_b}{\Omega_m}$, while the core structure of clusters is a test bed of the nature of dark matter.

In spite of the virtues of these cluster statistics, each of them has certain limitations. For instance, the systematics in converting cluster observables (X-ray luminosity, S-Z Compton parameter, richness and weak lensing) to mass may bias the scaling relation used for mass estimation. Construction of a reliable cluster catalog is the first step in the expedition of cluster cosmology.

6.2.2 3 × 2-point correlation functions

The digit 3 in the title of this section denotes three types of 2-point correlations employed in the statistical analysis, i.e. galaxy clustering, cosmic shear and galaxy-galaxy lensing measurements. Cosmic shear alone is sensitive to the dark matter density perturbation σ_8 and the fraction of dark matter Ω_m. However, intrinsic alignments potentially bias the results. The alignment of galaxies itself is a topic of interest that addresses the misalignment between galaxies and their dark matter halos, assuming a triaxial halo shape.

Recent weak lensing surveys (e.g. KiDS, HSC-SSP, DESc) and joint analyses combining all three surveys display a tension of 2σ or so with CMB experiments. The WFST surveys will suppress the error by a factor of 1.3, assuming a depth similar to that of DES and an effective weak lensing area of the WFS in the northern sky.

Apart from halo masses of galaxies, cosmological constraints can also be obtained by combining clustering analysis. Leauthaud et al. [280] found that σ_8 predicted by weak lensing is lower than the value that fits galaxy correlation well, a discrepancy known as the "lensing is low" problem. After that, the combination of galaxy-galaxy lensing and clustering analysis becomes a standard routine to maximize the utility of different estimators, e.g. an up-to-date work using HSC-SSP data that combines galaxy-galaxy lensing and clustering. Also notably, Shi et al. [281] combine the redshift space distortion (RSD) from the SDSS DR7 spectroscopy data and galaxy-galaxy lensing and provide a tight constraint on the growth factor at $z = 0.1$.

WFST WFS and DHS fields overlap with BOSS/HSC-SSP that contains spectroscopic sample with public availability, facilitating the clustering and galaxy-galaxy lensing joint analysis with LowZ and 2MASS samples. This combination will lead to an enhancement of sigal-to-noise ratio by a factor of 3.3 (WFS)/3.0 (DHS), compared to the CFHTLenS analysis and the HSC S16A shape catalog.

6.2.3 Joint Analysis with Other Observations

Besides weak gravitational lensing, multiple cosmological probes have been employed, such as the CMB radiation, baryon acoustic oscillations (BAO), and SNe Ia. The joint analysis and comparison between different probes are powerful tools. In particular, comparing the probes bearing different degeneracy direction for the same set of parameters may render the joint likelihood analysis to break the degeneracy between the parameters. For instance, Di Valentino et al. [282] combined BAO, CMB, Weak Lensing and SNe Ia analysis and extend the constraint of 6 LCDM parameters to 12 parameters by taking into account the sum of neutrino mass, the sum of neutrino species effective number, the dark energy equation of state, etc.

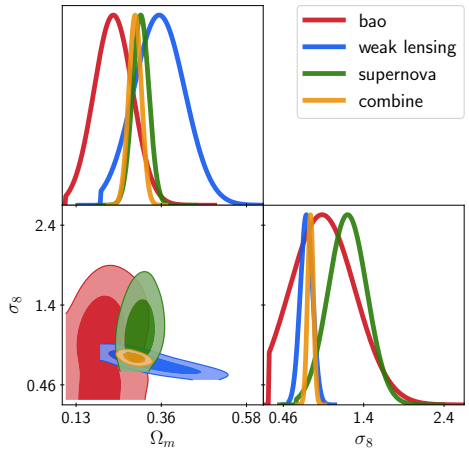

Figure 16 The joint analysis of cosmological constraints.

The commission of WFST will improve the joint analysis of SNe Ia, weak Lensing, clusters, time-dely and CMB in the northern sky, whereas the spectroscopic catalog from eBOSS and DESI survey will serve as a natural ally of WFST imaging data in relevant cosmological investigations.

6.2.4 Non-standard Cosmology

The tensions between the early and late probes lead to the possibility of new physics, like the "two dark clouds" in the early 20th century. Maybe certain interactions between dark matter and dark energy is the cause of the low σ_8 value from the weak lensing constraint, or can we find an substitute for dark matter or dark energy? What is dark matter exactly, and can it be tested by cosmological probes like cosmic shears? Does the theory of general relativity still hold at galactic scales?

Weak gravitational lensing can provide strong constraints on the dark side of our universe and therefore on non-standard cosmology. For instance, a recent work by Luo et al.[283] found that the Emergent Gravity can hardly explain the difference weak lensing signals between the blue/red galaxy sample with similar stellar mass. Zhang et al. [284] ruled out one of the interacting dark matter/energy models using weak gravitational lensing analysis based on the SDSS DR7 shear catalog.

WFST WFS and DHS fields are estimated to contain 7 and 22 times larger amount of source galaxies per arcminute square in survey area similar to SDSS, resulting in a wide and deep shape catalog to improve the current constraint by a factor 2.12 and 1.88, respectively.

7 Summary

WFST located near the summit of Mountain Saishiteng is a dedicated imaging facility under construction. The wide field survey (WFS) and the deep high-cadence survey (DHS) programs have been scheduled, covering a sky area of 8000 and 1000 square degrees, respectively. The unique design of WFST survey strategy will render a u-band imaging depth of 26.0 mag in the deep survey, comparable to the 10-year u-band depth of LSST. The high cadence enables the search for multiple time domain sources such as SNe, TDEs, optical counterparts of gravitational-wave events, AGN variability and the near-earth terrestrial objects. Stacked WFS and DHS data also facilitate cosmological investigations, such as weak/strong gravitational lensing, galaxy formation and constraints on cosmology.

The DHS mode of WFST will produce a catalog of tens of thousands of supernovae, of which a few hundreds are expected to have early-phase observations that promise to deliver information about the progenitor systems. The high-cadence u-band data will boost the detection of UV-luminous objects, a.k.a. FBOTs/FBUTs, as well as extreme SNe 100 times more luminous than SNe Ia and CCSNe. As low as the event rate of superluminous SNe, we anticipate that WFST will detect a sample of them at $z \leq 1.0$ with appreciable completeness. Furthermore, strongly-lensed supernovae at high redshift can be used to constrain Hubble parameter by measuring time delays in multiple-image systems. Aware of the 4 preexisting ones, we estimate that about 20 such systems will be discovered in the process of the 6-year WFST survey. The combination of the preexisting and newly found strongly-lensed AGNs from WFST legacy is expected to suppress the uncertainty of H_0 to $< 1.0\%$.

Kilonova, a transient phenomenon triggered by the merging process of a NS-NS or BH-NS binary is known as the electromagnetic counterpart of gravitational waves. This intriguing event was first confirmed by follow-up observations of GW170817/GRB170817A in 2017. Kilonovae can been used to explain the production of heavy elements through r-process and to constrain H_0 with electromagnetic observations rendering redshift information. Kilonova is also predicted to be coupled with short GRB, in spite of no agreement regarding the formation of the beamed gamma ray jets hitherto. The early optical afterglow of GRBs will remarkably help tackle the triggering mechanism of GRBs. Meanwhile, FRB has become a focus of time-domain astronomy since CHIME and other experiments discovered hundreds of repeating and non-repeating FRBs. WFST will provide optical information for these mysterious transients and deepen the understanding of the physics behind them. In addition, large number of high energy transients discovered by WFST

will be a crucial resource for searching for the electromagnetic counterparts of high energy neutrino events; together with the the careful designed follow-up program we may unravel the origin of these mysterious particles.

On galactic scales, another fruitful field in time domain astronomy is attributed to TDEs, deemed as a direct probe of the association of the central SMBH with AGN activity, though their rarity poses a challenge. The WFST surveys, by virtue of the large FoV and high cadence, promise to detect TDEs at a rate of hundreds per year with the redshift range to be extended to about 1.0. TDEs involving IMBHs is one of the numerous models to explain FBUTs that provide a promising way to fill or understand the gap between stellar BHs and SMBHs and to constrain the theory of seed black holes or the baby SMBHs. A grown-up SMBH residing in the galaxy center actively accretes surrounding materials to power the central engine of an AGN, another field of astrophysical importance, of which the diversity and variability have arisen broad interest. In particular, a subclass of AGNs displaying extreme variability, of which more than 20% have been confirmed as CL AGNs, remain of an enigmatic physical origin. Like strongly-lensed SNe, strongly-lensed AGNs are of fundamental use to cosmological tests. WFST will discover a significant amount of the above-mentioned objects that will help exploit extremely variable AGNs as well as cosmology.

We also assess the capability of WFST of detecting small objects in the solar system, concluding that WFST will improve both the positioning and the characterization of faint NEOs, cometary activity and TNOs (KBOs). The dynamical anomalies of the distant TNOs hint for the existence of Planet 9. The number of known TNOs as yet is only 14, including 5 chaotic ones, necessitating a sample with higher statistical significance to facilitate a further test of the Planet 9 hypothesis.

The stacked imaging data of WFST are a valuable legacy to exploit the Milky Way, galaxy formation and cosmology, of which the feasibility has been demonstrated by previous surveys. The WFST u-band covers the Balmer emission that serves as an indicator of the mass accretion rate, and other broad bands are requisite to measure the extinction. The 2-3 magnitude deeper photometry (in r band) of WFST than Pan-STARRS1 will improve the 3D dust mapping of the Galaxy and help pin down the number of dwarf galaxies in the vicinity of the Milky Way, rendering a direct test of the long-standing "missing satellite" problem.

Progress in the exploration of galaxy formation and cosmology relies not only on data quality, but also the amount of data. WFST will yield about 3PB imaging data in total six years, as a result of scanning 8000 square degrees in the WFS at a depth similar to that of DES, and 1000 square degree in the DHS at a depth similar to HSC SSP. As mentioned in Sec. 6, the release of the final 6-year WFST survey data promise to place remarkably improved constraints on galaxy-halo connection, cluster characterization and cosmology. The legacy shape catalog to be combined with other survey data (e.g., KiDS, DES, HSC SSP and upcoming survey projects) or even further with BAO, SNe Ia, time-delay and CMB measurements will facilitate a joint analysis anticipated to tighten a variety of cosmological constraints.

In conclusion, WFST is constructed at a site with premier observing conditions on the northern hemisphere. Once commissioned, this dedicated survey facility will yield massive data products that, in combination with future spectroscopic surveys of the northern sky (e.g. LAMOST II and MUST), promise to make a major step forward in time domain astronomy that will further benefit the entire astronomical community.

This work was supported by Cyrus Chun Ying Tang Foundations, the Major Science and Technology Project of Qinghai Province (2019-ZJ-A10), the 111 Project for "Observational and Theoretical Research on Dark Matter and Dark Energy" (B23042), the National Natural Science Foundation of China (Grant Nos. 11833007, 12192221, 12192224, 12273113, 12233008, 12273036), and the Frontier Scientific Research Program of Deep Space Exploration Laboratory (2022-QYKYJH-HXYF-012). ZYC and HNH acknowledge the supports from the USTC Research Funds of the Double First-Class Initiative with No. YD2030002009 and Project for Young Scientists in Basic Research of Chinese Academy of Sciences (No. YSBR-061), respectively.

Conflict of interest The authors declare that they have no conflict of interest.

1 I. N. Reid, C. Brewer, R. J. Brucato, W. R. McKinley, A. Maury, D. Mendenhall, J. R. Mould, J. Mueller, G. Neugebauer, J. Phinney, et al., Publ. Astron. Soc. Pac. **103**, 661 (1991).
2 M. F. Skrutskie, R. M. Cutri, R. Stiening, M. D. Weinberg, S. Schneider, J. M. Carpenter, C. Beichman, R. Capps, T. Chester, J. Elias, et al., Astron. J. **131**, 1163 (2006).
3 J. E. Gunn, W. A. Siegmund, E. J. Mannery, R. E. Owen, C. L. Hull, R. F. Leger, L. N. Carey, G. R. Knapp, D. G. York, W. N. Boroski, et al., Astron. J. **131**, 2332 (2006), arXiv: astro-ph/0602326.
4 The Dark Energy Survey Collaboration, arXiv e-prints astro-ph/0510346 (2005), arXiv: astro-ph/0510346.
5 G. Zhao, Y.-H. Zhao, Y.-Q. Chu, Y.-P. Jing, and L.-C. Deng, Research in Astronomy and Astrophysics **12**, 723 (2012).
6 DESI Collaboration, A. Aghamousa, J. Aguilar, S. Ahlen, S. Alam, L. E. Allen, C. Allende Prieto, J. Annis, S. Bailey, C. Balland, et al., arXiv e-prints arXiv:1611.00036 (2016), arXiv: 1611.00036.
7 A. J. Drake, S. G. Djorgovski, A. Mahabal, E. Beshore, S. Larson, M. J. Graham, R. Williams, E. Christensen, M. Catelan, A. Boattini, et al., Astrophys. J. **696**, 870 (2009), arXiv: 0809.1394.
8 N. M. Law, S. R. Kulkarni, R. G. Dekany, E. O. Ofek, R. M. Quimby, P. E. Nugent, J. Surace, C. C. Grillmair, J. S. Bloom, M. M. Kasliwal, et al., Publ. Astron. Soc. Pac. **121**, 1395 (2009), arXiv: 0906.5350.
9 E. C. Bellm, S. R. Kulkarni, T. Barlow, U. Feindt, M. J. Graham, A. Goobar, T. Kupfer, C.-C. Ngeow, P. Nugent, E. Ofek, et al., Publ. Astron. Soc. Pac. **131**, 068003 (2019), arXiv: 1905.02209.
10 N. Kaiser, in *Ground-based Telescopes*, (edited by J. Oschmann, Jacobus M.), volume 5489 of *Society of Photo-Optical Instrumentation*

Engineers (SPIE) Conference Series, 11–22 (2004).
11 B. J. Shappee, J. L. Prieto, D. Grupe, C. S. Kochanek, K. Z. Stanek, G. De Rosa, S. Mathur, Y. Zu, B. M. Peterson, R. W. Pogge, et al., Astrophys. J. **788**, 48 (2014), arXiv: 1310.2241.
12 J. L. Tonry, L. Denneau, A. N. Heinze, B. Stalder, K. W. Smith, S. J. Smartt, C. W. Stubbs, H. J. Weiland, and A. Rest, Publ. Astron. Soc. Pac. **130**, 064505 (2018), arXiv: 1802.00879.
13 I. Arcavi, C. McCully, G. Hosseinzadeh, D. A. Howell, S. Vasylyev, D. Poznanski, M. Zaltzman, D. Maoz, L. Singer, S. Valenti, et al., Astrophys. J. Lett. **848**, L33 (2017), arXiv: 1710.05842.
14 P. S. Cowperthwaite, E. Berger, V. A. Villar, B. D. Metzger, M. Nicholl, R. Chornock, P. K. Blanchard, W. Fong, R. Margutti, M. Soares-Santos, et al., Astrophys. J. Lett. **848**, L17 (2017), arXiv: 1710.05840.
15 Ž. Ivezić, S. M. Kahn, J. A. Tyson, B. Abel, E. Acosta, R. Allsman, D. Alonso, Y. AlSayyad, S. F. Anderson, J. Andrew, et al., Astrophys. J. **873**, 111 (2019), arXiv: 0805.2366.
16 L. Deng, F. Yang, X. Chen, F. He, Q. Liu, B. Zhang, C. Zhang, K. Wang, N. Liu, A. Ren, et al., Nature **596**, 353 (2021).
17 L. Lei, Q.-F. Zhu, X. Kong, T.-G. Wang, X.-Z. Zheng, D.-D. Shi, L.-L. Fan, and W. Liu, arXiv e-prints arXiv:2301.03068 (2023), arXiv: 2301.03068.
18 W. Yuan, C. Zhang, Z. Ling, D. Zhao, W. Wang, Y. Chen, F. Lu, S.-N. Zhang, and W. Cui, in *Space Telescopes and Instrumentation 2018: Ultraviolet to Gamma Ray*, (edited by J.-W. A. den Herder, S. Nikzad, and K. Nakazawa), volume 10699 of *Society of Photo-Optical Instrumentation Engineers (SPIE) Conference Series*, 1069925 (2018).
19 H. Zhan, Chin. Sci. Bull **66**, 1290 (2021).
20 F. Zwicky, Publ. Astron. Soc. Pac. **50**, 215 (1938).
21 W. Hillebrandt, M. Kromer, F. Röpke, and A. Ruiter, Frontiers of Physics **8**, 116 (2013).
22 D. Maoz, F. Mannucci, and G. Nelemans, Annu. Rev. Astron. Astrophys. **52**, 107 (2014).
23 M. M. Phillips, P. Lira, N. B. Suntzeff, R. A. Schommer, M. Hamuy, and J. Maza, Astron. J. **118**, 1766 (1999), arXiv: astro-ph/9907052.
24 K. Maeda, K. Kawabata, W. Li, M. Tanaka, P. A. Mazzali, T. Hattori, K. Nomoto, and A. V. Filippenko, Astrophys. J. **690**, 1745 (2009), arXiv: 0808.0138.
25 R. A. Scalzo, G. Aldering, P. Antilogus, C. Aragon, S. Bailey, C. Baltay, S. Bongard, C. Buton, M. Childress, N. Chotard, et al., Astrophys. J. **713**, 1073 (2010), arXiv: 1003.2217.
26 J. M. Silverman, M. Ganeshalingam, W. Li, A. V. Filippenko, A. A. Miller, and D. Poznanski, Mon. Not. R. Astron. Soc. **410**, 585 (2011), arXiv: 1003.2417.
27 S. Taubenberger, S. Benetti, M. Childress, R. Pakmor, S. Hachinger, P. A. Mazzali, V. Stanishev, N. Elias-Rosa, I. Agnoletto, F. Bufano, et al., Mon. Not. R. Astron. Soc. **412**, 2735 (2011), arXiv: 1011.5665.
28 J.-a. Jiang, K. Maeda, M. Kawabata, M. Doi, T. Shigeyama, M. Tanaka, N. Tominaga, K. Nomoto, Y. Niino, S. Sako, et al., Astrophys. J. Lett. **923**, L8 (2021), arXiv: 2111.09470.
29 R. J. Foley, P. J. Challis, R. Chornock, M. Ganeshalingam, W. Li, G. H. Marion, N. I. Morrell, G. Pignata, M. D. Stritzinger, J. M. Silverman, et al., Astrophys. J. **767**, 57 (2013), arXiv: 1212.2209.
30 A. V. Filippenko, A. J. Barth, T. Matheson, L. Armus, M. Brown, B. R. Espey, X.-M. Fan, R. W. Goodrich, L. C. Ho, V. T. Junkkarinen, et al., Astrophys. J. Lett. **450**, L11 (1995).
31 R. Barbon, F. Ciatti, and L. Rosino, Astron. Astrophys. **72**, 287 (1979).
32 E. M. Schlegel, Mon. Not. R. Astron. Soc. **244**, 269 (1990).
33 P. E. Nugent, M. Sullivan, S. B. Cenko, R. C. Thomas, D. Kasen, D. A. Howell, D. Bersier, J. S. Bloom, S. Kulkarni, M. T. Kandrashoff, et al., Nature **480**, 344 (2011).
34 Y. Cao, S. Kulkarni, D. A. Howell, A. Gal-Yam, M. M. Kasliwal, S. Valenti, J. Johansson, R. Amanullah, A. Goobar, J. Sollerman, et al., Nature **521**, 328 (2015).
35 J.-a. Jiang, M. Doi, K. Maeda, T. Shigeyama, K. Nomoto, N. Yasuda, S. W. Jha, M. Tanaka, T. Morokuma, N. Tominaga, et al., Nature **550**, 80 (2017).
36 D. Kasen, Astrophys. J. **708**, 1025 (2010).
37 A. L. Piro and V. S. Morozova, Astrophys. J. **826**, 96 (2016).
38 J.-a. Jiang, M. Doi, K. Maeda, and T. Shigeyama, Astrophys. J. **865**, 149 (2018).
39 J.-a. Jiang, N. Yasuda, K. Maeda, M. Doi, T. Shigeyama, N. Tominaga, M. Tanaka, T. J. Moriya, I. Takahashi, N. Suzuki, et al., Astrophys. J. **892**, 25 (2020), arXiv: 2002.10737.
40 K. Maeda, J.-a. Jiang, T. Shigeyama, and M. Doi, Astrophys. J. **861**, 78 (2018), arXiv: 1805.12325.
41 M. C. Bersten, G. Folatelli, F. García, S. D. van Dyk, O. G. Benvenuto, M. Orellana, V. Buso, J. L. Sánchez, M. Tanaka, K. Maeda, et al., Nature **554**, 497 (2018), arXiv: 1802.09360.
42 A. Y. Q. Ho, D. A. Perley, A. Gal-Yam, R. Lunnan, J. Sollerman, S. Schulze, K. K. Das, D. Dobie, Y. Yao, C. Fremling, et al., arXiv e-prints arXiv:2105.08811 (2021), arXiv: 2105.08811.
43 D. A. Perley, P. A. Mazzali, L. Yan, S. B. Cenko, S. Gezari, K. Taggart, N. Blagorodnova, C. Fremling, B. Mockler, A. Singh, et al., Mon. Not. R. Astron. Soc. **484**, 1031 (2019), arXiv: 1808.00969.
44 J.-a. Jiang, N. Yasuda, K. Maeda, N. Tominaga, M. Doi, Ž. Ivezić, P. Yoachim, K. Uno, T. J. Moriya, B. Kumar, et al., Astrophys. J. Lett. **933**, L36 (2022), arXiv: 2205.14889.
45 A. Gal-Yam, Science **337**, 927 (2012), arXiv: 1208.3217.
46 R. M. Quimby, G. Aldering, J. C. Wheeler, P. Höflich, C. W. Akerlof, and E. S. Rykoff, Astrophys. J. Lett. **668**, L99 (2007), arXiv: 0709.0302.
47 A. Gal-Yam, Annu. Rev. Astron. Astrophys. **57**, 305 (2019), arXiv: 1812.01428.
48 Z. Barkat, G. Rakavy, and N. Sack, Phys. Rev. Lett. **18**, 379 (1967).
49 S. E. Woosley, S. Blinnikov, and A. Heger, Nature **450**, 390 (2007), arXiv: 0710.3314.
50 S. Miyazaki, Y. Komiyama, S. Kawanomoto, Y. Doi, H. Furusawa, T. Hamana, Y. Hayashi, H. Ikeda, Y. Kamata, H. Karoji, et al., Publ. Astron. Soc. Jpn. **70**, S1 (2018).
51 S. Refsdal, Mon. Not. R. Astron. Soc. **128**, 307 (1964).
52 P. L. Kelly, S. A. Rodney, T. Treu, R. J. Foley, G. Brammer, K. B. Schmidt, A. Zitrin, A. Sonnenfeld, L.-G. Strolger, O. Graur, et al., Science **347**, 1123 (2015), arXiv: 1411.6009.
53 K. C. Wong, S. H. Suyu, G. C. F. Chen, C. E. Rusu, M. Millon, D. Sluse, V. Bonvin, C. D. Fassnacht, S. Taubenberger, M. W. Auger, et al., Mon. Not. R. Astron. Soc. **498**, 1420 (2020), arXiv: 1907.04869.
54 X. Ding, T. Treu, S. Birrer, A. Agnello, D. Sluse, C. Fassnacht, M. W. Auger, K. C. Wong, S. H. Suyu, T. Morishita, et al., Mon. Not. R. Astron. Soc. **501**, 269 (2021), arXiv: 2005.13550.
55 M. Oguri and P. J. Marshall, Mon. Not. R. Astron. Soc. **405**, 2579 (2010), arXiv: 1001.2037.
56 M. Hu, L. Hu, J.-a. Jiang, L. Xiao, L. Fan, J. Wei, and X. Wu, Universe **9**, 7 (2022), arXiv: 2212.11535.
57 E. Y. Hsiao, A. Conley, D. A. Howell, M. Sullivan, C. J. Pritchet, R. G. Carlberg, P. E. Nugent, and M. M. Phillips, ApJ **663**, 1187 (2007), arXiv: astro-ph/0703529.
58 M. J. Rees, Nature **333**, 523 (1988).
59 S. Gezari, Annu. Rev. Astron. Astrophys. **59** (2021), arXiv: 2104.14580.
60 S. van Velzen, S. Gezari, E. Hammerstein, N. Roth, S. Frederick, C. Ward, T. Hung, S. B. Cenko, R. Stein, D. A. Perley, et al., Astrophys. J. **908**, 4 (2021), arXiv: 2001.01409.
61 N. Jiang, T. Wang, X. Hu, L. Sun, L. Dou, and L. Xiao, Astrophys. J. **911**, 31 (2021), arXiv: 2102.08044.
62 R. Stein, S. v. Velzen, M. Kowalski, A. Franckowiak, S. Gezari, J. C. A. Miller-Jones, S. Frederick, I. Sfaradi, M. F. Bietenholz,

A. Horesh, et al., Nature Astronomy **5**, 510 (2021), arXiv: 2005.05340.
63 K. D. French, I. Arcavi, and A. Zabludoff, Astrophys. J. Lett. **818**, L21 (2016), arXiv: 1601.04705.
64 A. Zabludoff, I. Arcavi, S. La Massa, H. B. Perets, B. Trakhtenbrot, B. A. Zauderer, K. Auchettl, J. L. Dai, K. D. French, T. Hung, et al., Space Sci. Rev. **217**, 54 (2021), arXiv: 2103.12150.
65 S. van Velzen, T. W. S. Holoien, F. Onori, T. Hung, and I. Arcavi, Space Sci. Rev. **216**, 124 (2020), arXiv: 2008.05461.
66 D. Korytov, A. Hearin, E. Kovacs, P. Larsen, E. Rangel, J. Hollowed, A. J. Benson, K. Heitmann, Y.-Y. Mao, A. Bahmanyar, et al., Astrophys. J. Suppl. Ser. **245**, 26 (2019), arXiv: 1907.06530.
67 Z. Lin, N. Jiang, and X. Kong, Mon. Not. R. Astron. Soc. (2022), arXiv: 2204.01615.
68 J. E. Greene, J. Strader, and L. C. Ho, Annu. Rev. Astron. Astrophys. **58**, 257 (2020), arXiv: 1911.09678.
69 D. Lin, J. Strader, E. R. Carrasco, D. Page, A. J. Romanowsky, J. Homan, J. A. Irwin, R. A. Remillard, O. Godet, N. A. Webb, et al., Nature Astronomy **2**, 656 (2018), arXiv: 1806.05692.
70 M. MacLeod, J. Guillochon, E. Ramirez-Ruiz, D. Kasen, and S. Rosswog, Astrophys. J. **819**, 3 (2016), arXiv: 1508.02399.
71 C. R. Angus, V. F. Baldassare, B. Mockler, R. J. Foley, E. Ramirez-Ruiz, S. I. Raimundo, K. D. French, K. Auchettl, H. Pfister, C. Gall, et al., arXiv e-prints arXiv:2209.00018 (2022), arXiv: 2209.00018.
72 T. W. S. Holoien, P. J. Vallely, K. Auchettl, K. Z. Stanek, C. S. Kochanek, K. D. French, J. L. Prieto, B. J. Shappee, J. S. Brown, M. M. Fausnaugh, et al., Astrophys. J. **883**, 111 (2019), arXiv: 1904.09293.
73 J.-H. Chen and R.-F. Shen, Astrophys. J. **914**, 69 (2021), arXiv: 2104.08827.
74 A. V. Payne, B. J. Shappee, J. T. Hinkle, P. J. Vallely, C. S. Kochanek, T. W. S. Holoien, K. Auchettl, K. Z. Stanek, T. A. Thompson, J. M. M. Neustadt, et al., Astrophys. J. **910**, 125 (2021), arXiv: 2009.03321.
75 LIGO Scientific Collaboration and Virgo Collaboration, Phys. Rev. Lett. **119**, 161101 (2017), arXiv: 1710.05832.
76 A. Goldstein, P. Veres, E. Burns, M. S. Briggs, R. Hamburg, D. Kocevski, C. A. Wilson-Hodge, R. D. Preece, S. Poolakkil, O. J. Roberts, et al., Astrophys. J. Lett. **848**, L14 (2017), arXiv: 1710.05446.
77 V. Savchenko, C. Ferrigno, E. Kuulkers, A. Bazzano, E. Bozzo, S. Brandt, J. Chenevez, T. J. L. Courvoisier, R. Diehl, A. Domingo, et al., Astrophys. J. Lett. **848**, L15 (2017), arXiv: 1710.05449.
78 E. Symbalisty and D. N. Schramm, Astrophys. Lett. **22**, 143 (1982).
79 B. D. Metzger, G. Martínez-Pinedo, S. Darbha, E. Quataert, A. Arcones, D. Kasen, R. Thomas, P. Nugent, I. V. Panov, and N. T. Zinner, Mon. Not. R. Astron. Soc. **406**, 2650 (2010), arXiv: 1001.5029.
80 Y.-W. Yu, L.-D. Liu, and Z.-G. Dai, Astrophys. J. **861**, 114 (2018), arXiv: 1711.01898.
81 J.-J. Geng, Z.-G. Dai, Y.-F. Huang, X.-F. Wu, L.-B. Li, B. Li, and Y.-Z. Meng, Astrophys. J. Lett. **856**, L33 (2018), arXiv: 1803.07219.
82 L. Li and Z.-G. Dai, Astrophys. J. **918**, 52 (2021), arXiv: 2106.04788.
83 T. Dietrich, M. W. Coughlin, P. T. H. Pang, M. Bulla, J. Heinzel, L. Issa, I. Tews, and S. Antier, Science **370**, 1450 (2020), arXiv: 2002.11355.
84 C. Barbieri, O. S. Salafia, M. Colpi, G. Ghirlanda, A. Perego, and A. Colombo, Astrophys. J. Lett. **887**, L35 (2019), arXiv: 1912.03894.
85 B. Margalit and B. D. Metzger, Astrophys. J. Lett. **850**, L19 (2017), arXiv: 1710.05938.
86 T. Dietrich and M. Ujevic, Classical and Quantum Gravity **34**, 105014 (2017), arXiv: 1612.03665.
87 D. Radice, A. Perego, K. Hotokezaka, S. A. Fromm, S. Bernuzzi, and L. F. Roberts, Astrophys. J. **869**, 130 (2018), arXiv: 1809.11161.
88 B. D. Metzger and R. Fernández, Mon. Not. R. Astron. Soc. **441**, 3444 (2014), arXiv: 1402.4803.
89 LIGO Scientific Collaboration and Virgo Collaboration, Astrophys. J. Lett. **913**, L7 (2021), arXiv: 2010.14533.
90 Z.-Y. Liu, Z.-Y. Lin, J.-M. Yu, H.-Y. Wang, G.-M. Mourani, W. Zhao, and Z.-G. Dai, arXiv e-prints arXiv:2302.00246 (2023), arXiv: 2302.00246.
91 J. Yu, H. Song, S. Ai, H. Gao, F. Wang, Y. Wang, Y. Lu, W. Fang, and W. Zhao, Astrophys. J. **916**, 54 (2021), arXiv: 2104.12374.
92 B. Zhang and P. Mészáros, Astrophys. J. **571**, 876 (2002), arXiv: astro-ph/0112118.
93 R. Sari, T. Piran, and R. Narayan, Astrophys. J. Lett. **497**, L17 (1998), arXiv: astro-ph/9712005.
94 J.-P. Zhu, S. Wu, Y.-P. Yang, B. Zhang, H. Gao, Y.-W. Yu, Z. Li, Z. Cao, L.-D. Liu, Y. Huang, et al., Astrophys. J. **917**, 24 (2021), arXiv: 2011.02717.
95 M. J. Graham, K. E. S. Ford, B. McKernan, N. P. Ross, D. Stern, K. Burdge, M. Coughlin, S. G. Djorgovski, A. J. Drake, D. Duev, et al., Phys. Rev. Lett. **124**, 251102 (2020), arXiv: 2006.14122.
96 T. Piran, A. Shemi, and R. Narayan, Mon. Not. R. Astron. Soc. **263**, 861 (1993), arXiv: astro-ph/9301004.
97 P. Meszaros and M. J. Rees, Astrophys. J. **405**, 278 (1993).
98 K. D. Alexander, E. Berger, W. Fong, P. K. G. Williams, C. Guidorzi, R. Margutti, B. D. Metzger, J. Annis, P. K. Blanchard, D. Brout, et al., Astrophys. J. Lett. **848**, L21 (2017), arXiv: 1710.05457.
99 D. Lazzati, R. Perna, B. J. Morsony, D. Lopez-Camara, M. Cantiello, R. Ciolfi, B. Giacomazzo, and J. C. Workman, Phys. Rev. Lett. **120**, 241103 (2018), arXiv: 1712.03237.
100 T. Piran, Phys. Rep. **314**, 575 (1999), arXiv: astro-ph/9810256.
101 Z. G. Dai and T. Lu, Astron. Astrophys. **333**, L87 (1998), arXiv: astro-ph/9810402.
102 B. Zhang and H. Yan, Astrophys. J. **726**, 90 (2011), arXiv: 1011.1197.
103 P. Mészáros and M. J. Rees, Astrophys. J. **476**, 232 (1997), arXiv: astro-ph/9606043.
104 P. Mészáros and M. J. Rees, Mon. Not. R. Astron. Soc. **306**, L39 (1999), arXiv: astro-ph/9902367.
105 R. Sari and T. Piran, Astrophys. J. **520**, 641 (1999), arXiv: astro-ph/9901338.
106 B. Zhang, S. Kobayashi, and P. Mészáros, Astrophys. J. **595**, 950 (2003), arXiv: astro-ph/0302525.
107 Y. Z. Fan, D. M. Wei, and C. F. Wang, Astron. Astrophys. **424**, 477 (2004), arXiv: astro-ph/0405392.
108 W. T. Vestrand, J. A. Wren, A. Panaitescu, P. R. Wozniak, H. Davis, D. M. Palmer, G. Vianello, N. Omodei, S. Xiong, M. S. Briggs, et al., Science **343**, 38 (2014), arXiv: 1311.5489.
109 E. Troja, V. M. Lipunov, C. G. Mundell, N. R. Butler, A. M. Watson, S. Kobayashi, S. B. Cenko, F. E. Marshall, R. Ricci, A. Fruchter, et al., Nature **547**, 425 (2017).
110 A. M. Beloborodov and Z. L. Uhm, Astrophys. J. Lett. **651**, L1 (2006), arXiv: astro-ph/0607641.
111 Z. L. Uhm, Astrophys. J. **733**, 86 (2011), arXiv: 1003.1115.
112 J. J. Geng, X. F. Wu, L. Li, Y. F. Huang, and Z. G. Dai, Astrophys. J. **792**, 31 (2014), arXiv: 1407.0588.
113 J. J. Geng, X. F. Wu, Y. F. Huang, L. Li, and Z. G. Dai, Astrophys. J. **825**, 107 (2016), arXiv: 1605.01334.
114 S. Ai and B. Zhang, Mon. Not. R. Astron. Soc. **507**, 1788 (2021), arXiv: 2104.06450.
115 Y. Li, X. Wen, X. Sun, X. Liu, X. Liang, D. Guo, W. Peng, K. Gong, G. Li, H. Wang, et al., Scientia Sinica Physica, Mechanica & Astronomica **50**, 129508 (2020).
116 J. Wei, B. Cordier, S. Antier, P. Antilogus, J. L. Atteia, A. Bajat, S. Basa, V. Beckmann, M. G. Bernardini, S. Boissier, et al., arXiv e-prints arXiv:1610.06892 (2016), arXiv: 1610.06892.
117 R. Salvaterra, M. Della Valle, S. Campana, G. Chincarini, S. Covino, P. D'Avanzo, A. Fernández-Soto, C. Guidorzi, F. Mannucci, R. Margutti, et al., Nature **461**, 1258 (2009), arXiv: 0906.1578.

118 N. R. Tanvir, D. B. Fox, A. J. Levan, E. Berger, K. Wiersema, J. P. U. Fynbo, A. Cucchiara, T. Krühler, N. Gehrels, J. S. Bloom, et al., Nature **461**, 1254 (2009), arXiv: 0906.1577.

119 A. Cucchiara, A. J. Levan, D. B. Fox, N. R. Tanvir, T. N. Ukwatta, E. Berger, T. Krühler, A. Küpcü Yoldaş, X. F. Wu, K. Toma, et al., Astrophys. J. **736**, 7 (2011), arXiv: 1105.4915.

120 R. Salvaterra, Journal of High Energy Astrophysics **7**, 35 (2015), arXiv: 1503.03072.

121 F. Y. Wang, Z. G. Dai, and E. W. Liang, NewAR **67**, 1 (2015), arXiv: 1504.00735.

122 R. Salvaterra, S. Campana, G. Chincarini, S. Covino, and G. Tagliaferri, MNRAS **385**, 189 (2008), arXiv: 0710.4280.

123 G. Ghirlanda, R. Salvaterra, G. Ghisellini, S. Mereghetti, G. Tagliaferri, S. Campana, J. P. Osborne, P. O'Brien, N. Tanvir, D. Willingale, et al., MNRAS **448**, 2514 (2015), arXiv: 1502.02676.

124 J. Wei, X. Wu, F. Wang, Z. Liu, Z.-G. Dai, and B. Zhang, Scientia Sinica Physica, Mechanica & Astronomica **48**, 039505 (2018).

125 D. R. Lorimer, M. Bailes, M. A. McLaughlin, D. J. Narkevic, and F. Crawford, Science **318**, 777 (2007), arXiv: 0709.4301.

126 L. G. Spitler, P. Scholz, J. W. T. Hessels, S. Bogdanov, A. Brazier, F. Camilo, S. Chatterjee, J. M. Cordes, F. Crawford, J. Deneva, et al., Nature **531**, 202 (2016), arXiv: 1603.00581.

127 The CHIME/FRB Collaboration, :, M. Amiri, B. C. Andersen, K. Bandura, S. Berger, M. Bhardwaj, M. M. Boyce, P. J. Boyle, C. Brar, et al., arXiv e-prints arXiv:2106.04352 (2021), arXiv: 2106.04352.

128 J. P. Macquart, J. X. Prochaska, M. McQuinn, K. W. Bannister, S. Bhandari, C. K. Day, A. T. Deller, R. D. Ekers, C. W. James, L. Marnoch, et al., Nature **581**, 391 (2020), arXiv: 2005.13161.

129 S. Bhandari, K. E. Heintz, K. Aggarwal, L. Marnoch, C. K. Day, J. Sydnor, S. Burke-Spolaor, C. J. Law, J. X. Prochaska, N. Tejos, et al., arXiv e-prints arXiv:2108.01282 (2021), arXiv: 2108.01282.

130 S. Bhandari, E. M. Sadler, J. X. Prochaska, S. Simha, S. D. Ryder, L. Marnoch, K. W. Bannister, J.-P. Macquart, C. Flynn, R. M. Shannon, et al., Astrophys. J. Lett. **895**, L37 (2020), arXiv: 2005.13160.

131 Y. Li and B. Zhang, Astrophys. J. Lett. **899**, L6 (2020), arXiv: 2005.02371.

132 C. D. Bochenek, V. Ravi, K. V. Belov, G. Hallinan, J. Kocz, S. R. Kulkarni, and D. L. McKenna, Nature **587**, 59 (2020), arXiv: 2005.10828.

133 CHIME/FRB Collaboration, B. C. Andersen, K. M. Bandura, M. Bhardwaj, A. Bij, M. M. Boyce, P. J. Boyle, C. Brar, T. Cassanelli, P. Chawla, et al., Nature **587**, 54 (2020), arXiv: 2005.10324.

134 L. Lin, C. F. Zhang, P. Wang, H. Gao, X. Guan, J. L. Han, J. C. Jiang, P. Jiang, K. J. Lee, D. Li, et al., Nature **587**, 63 (2020), arXiv: 2005.11479.

135 S.-X. Yi, H. Gao, and B. Zhang, Astrophys. J. Lett. **792**, L21 (2014), arXiv: 1407.0348.

136 Y.-P. Yang, B. Zhang, and J.-Y. Wei, Astrophys. J. **878**, 89 (2019), arXiv: 1905.02429.

137 C. K. Li, L. Lin, S. L. Xiong, M. Y. Ge, X. B. Li, T. P. Li, F. J. Lu, S. N. Zhang, Y. L. Tuo, Y. Nang, et al., Nature Astronomy **5**, 378 (2021), arXiv: 2005.11071.

138 A. M. Beloborodov, Astrophys. J. **896**, 142 (2020), arXiv: 1908.07743.

139 G. Chen, V. Ravi, and W. Lu, Astrophys. J. **897**, 146 (2020), arXiv: 2004.10787.

140 L. Nicastro, C. Guidorzi, E. Palazzi, L. Zampieri, M. Turatto, and A. Gardini, Universe **7**, 76 (2021), arXiv: 2103.07786.

141 Anita Collaboration, P. W. Gorham, P. Allison, S. W. Barwick, J. J. Beatty, D. Z. Besson, W. R. Binns, C. Chen, P. Chen, J. M. Clem, et al., Astroparticle Physics **32**, 10 (2009), arXiv: 0812.1920.

142 G. Safronov, A. D. Avrorin, A. V. Avrorin, V. M. Aynutdinov, Z. Bardáčová, R. Bannasch, I. A. Belolaptikov, V. B. Brudanin, N. M. Budnev, G. V. Domogatsky, et al., in *40th International Conference on High Energy Physics*, 606 (2021), arXiv: 2012.03373.

143 F. Halzen, in *26th International Cosmic Ray Conference (ICRC26), Volume 2*, volume 2 of *International Cosmic Ray Conference*, 428 (1999).

144 IceCube Collaboration, Science **342**, 1242856 (2013), arXiv: 1311.5238.

145 A. Rau, S. R. Kulkarni, N. M. Law, J. S. Bloom, D. Ciardi, G. S. Djorgovski, D. B. Fox, A. Gal-Yam, C. C. Grillmair, M. M. Kasliwal, et al., Publ. Astron. Soc. Pac. **121**, 1334 (2009), arXiv: 0906.5355.

146 E. A. Magnier, E. Schlafly, D. Finkbeiner, M. Juric, J. L. Tonry, W. S. Burgett, K. C. Chambers, H. A. Flewelling, N. Kaiser, R. P. Kudritzki, et al., Astrophys. J. Suppl. Ser. **205**, 20 (2013), arXiv: 1303.3634.

147 IceCube Collaboration, M. G. Aartsen, M. Ackermann, J. Adams, J. A. Aguilar, M. Ahlers, M. Ahrens, I. A. Samarai, D. Altmann, K. Andeen, et al., Science **361**, 147 (2018), arXiv: 1807.08794.

148 A. Franckowiak, S. Garrappa, V. Paliya, B. Shappee, R. Stein, N. L. Strotjohann, M. Kowalski, S. Buson, S. Kiehlmann, W. Max-Moerbeck, et al., Astrophys. J. **893**, 162 (2020), arXiv: 2001.10232.

149 F. W. Stecker, C. Done, M. H. Salamon, and P. Sommers, Physical Review Letters **66**, 2697 (1991).

150 IceCube Collaboration, M. G. Aartsen, M. Ackermann, J. Adams, J. A. Aguilar, M. Ahlers, M. Ahrens, I. Al Samarai, D. Altmann, K. Andeen, et al., Science **361**, eaat1378 (2018), arXiv: 1807.08816.

151 E. O'Sullivan and C. Finley, in *36th International Cosmic Ray Conference (ICRC2019)*, volume 36 of *International Cosmic Ray Conference*, 973 (2019), arXiv: 1908.05526.

152 E. Waxman and J. Bahcall, Physical Review Letters **78**, 2292 (1997), arXiv: astro-ph/9701231.

153 D. Xiao and Z. G. Dai, Astrophys. J. **790**, 59 (2014), arXiv: 1406.2792.

154 H.-N. He, A. Kusenko, S. Nagataki, Y.-Z. Fan, and D.-M. Wei, Astrophys. J. **856**, 119 (2018), arXiv: 1803.07478.

155 M. G. Aartsen, K. Abraham, M. Ackermann, J. Adams, J. A. Aguilar, M. Ahlers, M. Ahrens, D. Altmann, T. Anderson, M. Archinger, et al., Astrophys. J. **811**, 52 (2015), arXiv: 1506.03115.

156 IceCube Collaboration, M. G. Aartsen, M. Ackermann, J. Adams, J. A. Aguilar, M. Ahlers, M. Ahrens, I. Al Samarai, D. Altmann, K. Andeen, et al., Astron. Astrophys. **607**, A115 (2017), arXiv: 1702.06131.

157 C. L. MacLeod, Ž. Ivezić, C. S. Kochanek, S. Kozłowski, B. Kelly, E. Bullock, A. Kimball, B. Sesar, D. Westman, K. Brooks, et al., Astrophys. J. **721**, 1014 (2010), arXiv: 1004.0276.

158 B. W. Lyke, A. N. Higley, J. N. McLane, D. P. Schurhammer, A. D. Myers, A. J. Ross, K. Dawson, S. Chabanier, P. Martini, N. G. Busca, et al., Astrophys. J. Suppl. Ser. **250**, 8 (2020), arXiv: 2007.09001.

159 F. J. Masci, R. R. Laher, B. Rusholme, D. L. Shupe, S. Groom, J. Surace, E. Jackson, S. Monkewitz, R. Beck, D. Flynn, et al., Publ. Astron. Soc. Pac. **131**, 018003 (2019), arXiv: 1902.01872.

160 K. C. Chambers, E. A. Magnier, N. Metcalfe, H. A. Flewelling, M. E. Huber, C. Z. Waters, L. Denneau, P. W. Draper, D. Farrow, D. P. Finkbeiner, et al., arXiv e-prints arXiv:1612.05560 (2016), arXiv: 1612.05560.

161 J. H. Krolik, K. Horne, T. R. Kallman, M. A. Malkan, R. A. Edelson, and G. A. Kriss, Astrophys. J. **371**, 541 (1991).

162 Z.-Y. Cai, J.-X. Wang, F.-F. Zhu, M.-Y. Sun, W.-M. Gu, X.-W. Cao, and F. Yuan, Astrophys. J. **855**, 117 (2018), arXiv: 1711.06266.

163 M. Sun, Y. Xue, H. Guo, J. Wang, W. N. Brandt, J. R. Trump, Z. He, T. Liu, J. Wu, and H. Li, Astrophys. J. **902**, 7 (2020), arXiv: 2008.09967.

164 M.-H. Ulrich, L. Maraschi, and C. M. Urry, Annu. Rev. Astron. Astrophys. **35**, 445 (1997).

165 B. C. Kelly, J. Bechtold, and A. Siemiginowska, Astrophys. J. **698**, 895 (2009), arXiv: 0903.5315.

166 Z. He, T. Wang, G. Liu, H. Wang, W. Bian, K. Tchernyshyov, G. Mou, Y. Xu, H. Zhou, R. Green, et al., Nature Astronomy **3**, 265 (2019),

arXiv: 1812.08982.
167 Z.-Y. Cai, J.-X. Wang, and M. Sun, Astrophys. J. **892**, 63 (2020), arXiv: 2002.11116.
168 H. Sou, J.-X. Wang, Z.-L. Xie, W.-Y. Kang, and Z.-Y. Cai, Mon. Not. R. Astron. Soc. **512**, 5511 (2022), arXiv: 2203.07119.
169 Z. Yu, P. Martini, T. M. Davis, R. A. Gruendl, J. K. Hoormann, C. S. Kochanek, C. Lidman, D. Mudd, B. M. Peterson, W. Wester, et al., Astrophys. J. Suppl. Ser. **246**, 16 (2020), arXiv: 1811.03638.
170 Y. Homayouni, J. R. Trump, C. J. Grier, Y. Shen, D. A. Starkey, W. N. Brandt, G. Fonseca Alvarez, P. B. Hall, K. Horne, K. Kinemuchi, et al., Astrophys. J. **880**, 126 (2019), arXiv: 1806.08360.
171 F.-F. Zhu, J.-X. Wang, Z.-Y. Cai, Y.-H. Sun, M.-Y. Sun, and J.-X. Zhang, Astrophys. J. **860**, 29 (2018), arXiv: 1711.00870.
172 Y.-H. Sun, J.-X. Wang, X.-Y. Chen, and Z.-Y. Zheng, Astrophys. J. **792**, 54 (2014), arXiv: 1407.4230.
173 N. Rumbaugh, Y. Shen, E. Morganson, X. Liu, M. Banerji, R. G. McMahon, F. B. Abdalla, A. Benoit-Lévy, E. Bertin, D. Brooks, et al., Astrophys. J. **854**, 160 (2018), arXiv: 1706.07875.
174 W. Ren, J. Wang, Z. Cai, and H. Guo, arXiv e-prints arXiv:2111.07057 (2021), arXiv: 2111.07057.
175 C. L. MacLeod, P. J. Green, S. F. Anderson, A. Bruce, M. Eracleous, M. Graham, D. Homan, A. Lawrence, A. LeBleu, N. P. Ross, et al., Astrophys. J. **874**, 8 (2019), arXiv: 1810.00087.
176 Z. Sheng, T. Wang, N. Jiang, C. Yang, L. Yan, L. Dou, and B. Peng, Astrophys. J. Lett. **846**, L7 (2017), arXiv: 1707.02686.
177 M. J. Graham, S. G. Djorgovski, A. J. Drake, D. Stern, A. A. Mahabal, E. Glikman, S. Larson, and E. Christensen, Mon. Not. R. Astron. Soc. **470**, 4112 (2017), arXiv: 1706.03079.
178 A. Lawrence, A. G. Bruce, C. MacLeod, S. Gezari, M. Elvis, M. Ward, S. J. Smartt, K. W. Smith, D. Wright, M. Fraser, et al., Mon. Not. R. Astron. Soc. **463**, 296 (2016), arXiv: 1605.07842.
179 M. J. Graham, S. G. Djorgovski, D. Stern, A. J. Drake, A. A. Mahabal, C. Donalek, E. Glikman, S. Larson, and E. Christensen, Mon. Not. R. Astron. Soc. **453**, 1562 (2015), arXiv: 1507.07603.
180 T. Liu, S. Gezari, M. Ayers, W. Burgett, K. Chambers, K. Hodapp, M. E. Huber, R. P. Kudritzki, N. Metcalfe, J. Tonry, et al., Astrophys. J. **884**, 36 (2019), arXiv: 1906.08315.
181 C. J. Burke, Y. Shen, O. Blaes, C. F. Gammie, K. Horne, Y.-F. Jiang, X. Liu, I. M. McHardy, C. W. Morgan, S. Scaringi, et al., Science **373**, 789 (2021), arXiv: 2108.05389.
182 M. C. Begelman, R. D. Blandford, and M. J. Rees, Nature **287**, 307 (1980).
183 F. Pretorius, Phys. Rev. Lett. **95**, 121101 (2005), arXiv: gr-qc/0507014.
184 A. E. Reines, J. J. Condon, J. Darling, and J. E. Greene, Astrophys. J. **888**, 36 (2020), arXiv: 1909.04670.
185 C. Ward, S. Gezari, S. Frederick, E. Hammerstein, P. Nugent, S. van Velzen, A. Drake, A. García-Pérez, I. Oyoo, E. C. Bellm, et al., Astrophys. J. **913**, 102 (2021), arXiv: 2011.11656.
186 D. C. Y. Chao, J. H. H. Chan, S. H. Suyu, N. Yasuda, T. Morokuma, A. T. Jaelani, T. Nagao, and C. E. Rusu, arXiv e-prints arXiv:2009.07854 (2020), arXiv: 2009.07854.
187 Y. Shu, V. Belokurov, and N. W. Evans, Mon. Not. R. Astron. Soc. **502**, 2912 (2021), arXiv: 2011.04667.
188 L. W. Alvarez, W. Alvarez, F. Asaro, and H. V. Michel, Science **208**, 1095 (1980).
189 L. Denneau, R. Jedicke, T. Grav, M. Granvik, J. Kubica, A. Milani, P. Vereš, R. Wainscoat, D. Chang, F. Pierfederici, et al., Publ. Astron. Soc. Pac. **125**, 357 (2013), arXiv: 1302.7281.
190 E. A. Magnier, K. C. Chambers, H. A. Flewelling, J. C. Hoblitt, M. E. Huber, P. A. Price, W. E. Sweeney, C. Z. Waters, L. Denneau, P. W. Draper, et al., Astrophys. J. Suppl. Ser. **251**, 3 (2020), arXiv: 1612.05240.
191 M. Granvik, A. Morbidelli, R. Jedicke, B. Bolin, W. F. Bottke, E. Beshore, D. Vokrouhlický, D. Nesvorný, and P. Michel, Icarus **312**, 181 (2018), arXiv: 1804.10265.
192 Q. Ye, F. J. Masci, W.-H. Ip, T. A. Prince, G. Helou, D. Farnocchia, E. C. Bellm, R. Dekany, M. J. Graham, S. R. Kulkarni, et al., Astron. J. **159**, 70 (2020), arXiv: 1912.06109.
193 P. Wiegert, K. Innanen, and S. Mikkola, Icarus **145**, 33 (2000), arXiv: astro-ph/9912254.
194 F. Patat, O. S. Ugolnikov, and O. V. Postylyakov, Astron. Astrophys. **455**, 385 (2006), arXiv: astro-ph/0604128.
195 P. Mróz, A. Otarola, T. A. Prince, R. Dekany, D. A. Duev, M. J. Graham, S. L. Groom, F. J. Masci, and M. S. Medford, Astrophys. J. Lett. **924**, L30 (2022), arXiv: 2201.05343.
196 H. H. Hsieh and D. Jewitt, Science **312**, 561 (2006).
197 A. Morbidelli, J. I. Lunine, D. P. O'Brien, S. N. Raymond, and K. J. Walsh, Annual Review of Earth and Planetary Sciences **40**, 251 (2012), arXiv: 1208.4694.
198 N. Haghighipour, T. I. Maindl, C. Schäfer, R. Speith, and R. Dvorak, Astrophys. J. **830**, 22 (2016), arXiv: 1606.06226.
199 H. H. Hsieh, C. O. Chandler, L. Denneau, A. Fitzsimmons, N. Erasmus, M. S. P. Kelley, M. M. Knight, T. A. Lister, J. Pittichová, S. S. Sheppard, et al., Astrophys. J. Lett. **922**, L9 (2021), arXiv: 2109.14822.
200 F. L. Whipple, Astrophys. J. **111**, 375 (1950).
201 J. X. Luu, Publ. Astron. Soc. Pac. **105**, 946 (1993).
202 A. Morbidelli and D. Nesvorný, in *The Trans-Neptunian Solar System*, (edited by D. Prialnik, M. A. Barucci, and L. Young), 25–59 (2020).
203 J. M. Petit, J. J. Kavelaars, B. J. Gladman, R. L. Jones, J. W. Parker, C. Van Laerhoven, P. Nicholson, G. Mars, P. Rousselot, O. Mousis, et al., Astron. J. **142**, 131 (2011), arXiv: 1108.4836.
204 D. Nesvorný, Annu. Rev. Astron. Astrophys. **56**, 137 (2018), arXiv: 1807.06647.
205 M. Marsset, W. C. Fraser, R. E. Pike, M. T. Bannister, M. E. Schwamb, K. Volk, J. J. Kavelaars, M. Alexandersen, Y.-T. Chen, B. J. Gladman, et al., Astron. J. **157**, 94 (2019), arXiv: 1812.02190.
206 D. Nesvorný, D. Vokrouhlický, W. F. Bottke, and H. F. Levison, Nature Astronomy **2**, 878 (2018), arXiv: 1809.04007.
207 K. Batygin and M. E. Brown, Astron. J. **151**, 22 (2016), arXiv: 1601.05438.
208 K. Batygin, F. C. Adams, M. E. Brown, and J. C. Becker, Phys. Rep. **805**, 1 (2019), arXiv: 1902.10103.
209 E. Gullbring, P. P. Petrov, I. Ilyin, I. Tuominen, G. F. Gahm, and K. Loden, Astron. Astrophys. **314**, 835 (1996).
210 J. Bouvier, K. N. Grankin, S. H. P. Alencar, C. Dougados, M. Fernández, G. Basri, C. Batalha, E. Guenther, M. A. Ibrahimov, T. Y. Magakian, et al., Astron. Astrophys. **409**, 169 (2003), arXiv: astro-ph/0306551.
211 L. I. Biddle, C. M. Johns-Krull, J. Llama, L. Prato, and B. A. Skiff, Astrophys. J. Lett. **853**, L34 (2018), arXiv: 1801.06234.
212 L. Hartmann, G. Herczeg, and N. Calvet, Annu. Rev. Astron. Astrophys. **54**, 135 (2016).
213 E. Gullbring, L. Hartmann, C. Briceño, and N. Calvet, Astrophys. J. **492**, 323 (1998).
214 J. M. Alcalá, A. Natta, C. F. Manara, L. Spezzi, B. Stelzer, A. Frasca, K. Biazzo, E. Covino, S. Randich, E. Rigliaco, et al., Astron. Astrophys. **561**, A2 (2014), arXiv: 1310.2069.
215 F. H. Shu, F. C. Adams, and S. Lizano, Annu. Rev. Astron. Astrophys. **25**, 23 (1987).
216 S. J. Kenyon, L. W. Hartmann, K. M. Strom, and S. E. Strom, Astron. J. **99**, 869 (1990).
217 S. J. Kenyon and L. Hartmann, Astrophys. J. Suppl. Ser. **101**, 117 (1995).
218 L. Hartmann and S. J. Kenyon, Annu. Rev. Astron. Astrophys. **34**, 207 (1996).
219 Z. Chen, W. Sun, R. Chini, M. Haas, Z. Jiang, and X. Chen, Astrophys. J. **922**, 90 (2021), arXiv: 2108.12554.

220 M. Audard, P. Ábrahám, M. M. Dunham, J. D. Green, N. Grosso, K. Hamaguchi, J. H. Kastner, Á. Kóspál, G. Lodato, M. M. Romanova, et al., in *Protostars and Planets VI*, (edited by H. Beuther, R. S. Klessen, C. P. Dullemond, and T. Henning), 387 (2014), arXiv: 1401.3368.

221 L. A. Hillenbrand and K. P. Findeisen, Astrophys. J. **808**, 68 (2015), arXiv: 1506.01126.

222 B. Q. Chen, Y. Huang, H. B. Yuan, C. Wang, D. W. Fan, M. S. Xiang, H. W. Zhang, Z. J. Tian, and X. W. Liu, Mon. Not. R. Astron. Soc. **483**, 4277 (2019), arXiv: 1807.02241.

223 G. M. Green, E. Schlafly, C. Zucker, J. S. Speagle, and D. Finkbeiner, Astrophys. J. **887**, 93 (2019), arXiv: 1905.02734.

224 T. Röhser, J. Kerp, D. Lenz, and B. Winkel, Astron. Astrophys. **596**, A94 (2016), arXiv: 1609.06540.

225 S. Ramírez Alegría, J. Borissova, A. N. Chené, C. Bonatto, R. Kurtev, P. Amigo, M. Kuhn, M. Gromadzki, and J. A. Carballo-Bello, Astron. Astrophys. **588**, A40 (2016), arXiv: 1602.04898.

226 G. A. Gontcharov, M. Y. Khovritchev, A. V. Mosenkov, V. B. Il'in, A. A. Marchuk, S. S. Savchenko, A. A. Smirnov, P. A. Usachev, and D. M. Poliakov, Mon. Not. R. Astron. Soc. **508**, 2688 (2021), arXiv: 2109.13115.

227 E. J. Lee, M.-A. Miville-Deschênes, and N. W. Murray, Astrophys. J. **833**, 229 (2016), arXiv: 1608.05415.

228 Y. Su, J. Yang, S. Zhang, Y. Gong, H. Wang, X. Zhou, M. Wang, Z. Chen, Y. Sun, X. Chen, et al., Astrophys. J. Suppl. Ser. **240**, 9 (2019), arXiv: 1901.00285.

229 T. Cantat-Gaudin, C. Jordi, A. Vallenari, A. Bragaglia, L. Balaguer-Núñez, C. Soubiran, D. Bossini, A. Moitinho, A. Castro-Ginard, A. Krone-Martins, et al., Astron. Astrophys. **618**, A93 (2018), arXiv: 1805.08726.

230 D. Bossini, A. Vallenari, A. Bragaglia, T. Cantat-Gaudin, R. Sordo, L. Balaguer-Núñez, C. Jordi, A. Moitinho, C. Soubiran, L. Casamiquela, et al., Astron. Astrophys. **623**, A108 (2019), arXiv: 1901.04733.

231 Ž. Ivezić, B. Sesar, M. Jurić, N. Bond, J. Dalcanton, C. M. Rockosi, B. Yanny, H. J. Newberg, T. C. Beers, C. Allende Prieto, et al., Astrophys. J. **684**, 287 (2008), arXiv: 0804.3850.

232 I. Baraffe, D. Homeier, F. Allard, and G. Chabrier, Astron. Astrophys. **577**, A42 (2015), arXiv: 1503.04107.

233 Y.-B. Li, A. L. Luo, Y.-J. Lu, X.-S. Zhang, J. Li, R. Wang, F. Zuo, M. Xiang, Y.-S. Ting, T. Marchetti, et al., Astrophys. J. Suppl. Ser. **252**, 3 (2021), arXiv: 2011.10206.

234 F. Giovannelli and L. Sabau-Graziati, Chinese Journal of Astronomy and Astrophysics **3**, 202 (2003).

235 C. Mateu, B. Holl, J. De Ridder, and L. Rimoldini, Mon. Not. R. Astron. Soc. **496**, 3291 (2020), arXiv: 2006.09416.

236 L. L. Watkins, R. P. van der Marel, S. T. Sohn, and N. W. Evans, Astrophys. J. **873**, 118 (2019), arXiv: 1804.11348.

237 C. Mateu and A. K. Vivas, Mon. Not. R. Astron. Soc. **479**, 211 (2018), arXiv: 1802.07798.

238 X. Chen, S. Wang, L. Deng, R. de Grijs, M. Yang, and H. Tian, Astrophys. J. Suppl. Ser. **249**, 18 (2020), arXiv: 2005.08662.

239 S.-B. Qian, L.-Y. Zhu, L. Liu, X.-D. Zhang, X.-D. Shi, J.-J. He, and J. Zhang, Research in Astronomy and Astrophysics **20**, 163 (2020).

240 O. J. Eggen, Memoirs of the Royal Astronomical Society **70**, 111 (1967).

241 S.-B. Qian, J.-J. He, J. Zhang, L.-Y. Zhu, X.-D. Shi, E.-G. Zhao, and X. Zhou, Research in Astronomy and Astrophysics **17**, 087 (2017), arXiv: 1705.03996.

242 W. H. G. Lewin and M. van der Klis, *Compact Stellar X-ray Sources*, volume 39 (2006).

243 Q. Z. Liu, J. van Paradijs, and E. P. J. van den Heuvel, Astron. Astrophys. **455**, 1165 (2006), arXiv: 0707.0549.

244 Q. Z. Liu, J. van Paradijs, and E. P. J. van den Heuvel, Astron. Astrophys. **469**, 807 (2007), arXiv: 0707.0544.

245 P. Reig, Astrophysics and Space Science **332**, 1 (2011).

246 J. Casares, I. Negueruela, M. Ribó, I. Ribas, J. M. Paredes, A. Herrero, and S. Simón-Díaz, Nature **505**, 378 (2014).

247 I. Negueruela, Arxiv preprint astro-ph/9807158 (1998).

248 J. Yan, H. Li, and Q. Liu, Astrophys. J. **744**, 37 (2012), arXiv: 1111.0715.

249 L. M. van Haaften, G. Nelemans, R. Voss, M. V. van der Sluys, and S. Toonen, Astron. Astrophys. **579**, A33 (2015), arXiv: 1505.03629.

250 D. R. Weisz, A. E. Dolphin, E. D. Skillman, J. Holtzman, K. M. Gilbert, J. J. Dalcanton, and B. F. Williams, Astrophys. J. **789**, 147 (2014), arXiv: 1404.7144.

251 M. Geha, T. M. Brown, J. Tumlinson, J. S. Kalirai, J. D. Simon, E. N. Kirby, D. A. VandenBerg, R. R. Muñoz, R. J. Avila, P. Guhathakurta, et al., Astrophys. J. **771**, 29 (2013), arXiv: 1304.7769.

252 J. S. Bullock and M. Boylan-Kolchin, Annu. Rev. Astron. Astrophys. **55**, 343 (2017), arXiv: 1707.04256.

253 K. Spekkens, B. S. Mason, J. E. Aguirre, and B. Nhan, Astrophys. J. **773**, 61 (2013), arXiv: 1301.5306.

254 S. Sharma, J. Bland-Hawthorn, K. V. Johnston, and J. Binney, Astrophys. J. **730**, 3 (2011), arXiv: 1101.3561.

255 P. Kroupa, Mon. Not. R. Astron. Soc. **322**, 231 (2001), arXiv: astro-ph/0009005.

256 S. Koposov, V. Belokurov, N. W. Evans, P. C. Hewett, M. J. Irwin, G. Gilmore, D. B. Zucker, H. W. Rix, M. Fellhauer, E. F. Bell, et al., Astrophys. J. **686**, 279 (2008), arXiv: 0706.2687.

257 X. Li, H. Miyatake, W. Luo, S. More, M. Oguri, T. Hamana, R. Mandelbaum, M. Shirasaki, M. Takada, R. Armstrong, et al., Publ. Astron. Soc. Jpn. **74**, 421 (2022), arXiv: 2107.00136.

258 W. Luo, X. Yang, J. Zhang, D. Tweed, L. Fu, H. J. Mo, F. C. van den Bosch, C. Shu, R. Li, N. Li, et al., Astrophys. J. **836**, 38 (2017), arXiv: 1607.05406.

259 W. Luo, X. Yang, T. Lu, F. Shi, J. Zhang, H. J. Mo, C. Shu, L. Fu, M. Radovich, J. Zhang, et al., ArXiv e-prints (2017), arXiv: 1712.09030.

260 Z. Zhang, H. Wang, W. Luo, H. J. Mo, Z. Liang, R. Li, X. Yang, T. Wang, H. Zhang, H. Hong, et al., Astron. Astrophys. **650**, A155 (2021), arXiv: 2012.10640.

261 Z. Zhang, H. Wang, W. Luo, J. Zhang, H. J. Mo, Y. Jing, X. Yang, and H. Li, Astron. Astrophys. **663**, A85 (2022), arXiv: 2112.04777.

262 H. Miyatake, S. More, M. Takada, D. N. Spergel, R. Mandelbaum, E. S. Rykoff, and E. Rozo, Phys. Rev. Lett. **116**, 041301 (2016), arXiv: 1506.06135.

263 Y. Zu, R. Mandelbaum, M. Simet, E. Rozo, and E. S. Rykoff, Mon. Not. R. Astron. Soc. **470**, 551 (2017), arXiv: 1611.00366.

264 H. Wang, H. J. Mo, X. Yang, Y. P. Jing, and W. P. Lin, Astrophys. J. **794**, 94 (2014), arXiv: 1407.3451.

265 Y.-T. Lin, R. Mandelbaum, Y.-H. Huang, H.-J. Huang, N. Dalal, B. Diemer, H.-Y. Jian, and A. Kravtsov, Astrophys. J. **819**, 119 (2016), arXiv: 1504.07632.

266 K. S. McCarthy, Z. Zheng, H. Guo, W. Luo, and Y.-T. Lin, Mon. Not. R. Astron. Soc. **509**, 380 (2022), arXiv: 2104.13379.

267 S. More, B. Diemer, and A. V. Kravtsov, Astrophys. J. **810**, 36 (2015), arXiv: 1504.05591.

268 X. Wang, H. Wang, and H. J. Mo, arXiv e-prints arXiv:2206.12163 (2022), arXiv: 2206.12163.

269 M. Giavalisco, Annu. Rev. Astron. Astrophys. **40**, 579 (2002).

270 M. Sawicki, S. Arnouts, J. Huang, J. Coupon, A. Golob, S. Gwyn, S. Foucaud, T. Moutard, I. Iwata, C. Liu, et al., Mon. Not. R. Astron. Soc. **489**, 5202 (2019), arXiv: 1909.05898.

271 T. Moutard, M. Sawicki, S. Arnouts, A. Golob, J. Coupon, O. Ilbert, X. Yang, and S. Gwyn, Mon. Not. R. Astron. Soc. **494**, 1894 (2020), arXiv: 2001.06904.

272 C. C. Steidel, M. Pettini, and D. Hamilton, Astron. J. **110**, 2519 (1995), arXiv: astro-ph/9509089.

273 N. A. Reddy and C. C. Steidel, Astrophys. J. **692**, 778 (2009), arXiv:

0810.2788.
274 Z.-Y. Cai, A. Lapi, A. Bressan, G. De Zotti, M. Negrello, and L. Danese, Astrophys. J. **785**, 65 (2014), arXiv: 1403.0055.
275 C. C. Steidel, K. L. Adelberger, M. Giavalisco, M. Dickinson, and M. Pettini, Astrophys. J. **519**, 1 (1999), arXiv: astro-ph/9811399.
276 S. Danieli, P. van Dokkum, and C. Conroy, Astrophys. J. **856**, 69 (2018), arXiv: 1711.00860.
277 X. Yang, H. Xu, M. He, Y. Gu, A. Katsianis, J. Meng, F. Shi, H. Zou, Y. Zhang, C. Liu, et al., Astrophys. J. **909**, 143 (2021), arXiv: 2012.14998.
278 X. Yang, H. J. Mo, F. C. van den Bosch, A. Pasquali, C. Li, and M. Barden, Astrophys. J. **671**, 153 (2007), arXiv: 0707.4640.
279 T. Sunayama, Y. Park, M. Takada, Y. Kobayashi, T. Nishimichi, T. Kurita, S. More, M. Oguri, and K. Osato, Mon. Not. R. Astron. Soc. **496**, 4468 (2020), arXiv: 2002.03867.
280 A. Leauthaud, S. Saito, S. Hilbert, A. Barreira, S. More, M. White, S. Alam, P. Behroozi, K. Bundy, J. Coupon, et al., Mon. Not. R. Astron. Soc. **467**, 3024 (2017), arXiv: 1611.08606.
281 F. Shi, X. Yang, H. Wang, Y. Zhang, H. J. Mo, F. C. van den Bosch, W. Luo, D. Tweed, S. Li, C. Liu, et al., Astrophys. J. **861**, 137 (2018), arXiv: 1712.04163.
282 E. Di Valentino, A. Melchiorri, and J. Silk, Phys. Rev. D **92**, 121302 (2015), arXiv: 1507.06646.
283 W. Luo, J. Zhang, V. Halenka, X. Yang, S. More, C. J. Miller, L. Liu, and F. Shi, Astrophys. J. **914**, 96 (2021), arXiv: 2003.09818.
284 J. Zhang, R. An, W. Luo, Z. Li, S. Liao, and B. Wang, Astrophys. J. Lett. **875**, L11 (2019), arXiv: 1807.05522.